

DIGITAL ACCESS TO SCHOLARSHIP AT HARVARD
DASH.HARVARD.EDU

HARVARD LIBRARY


Electroadhesion Design for Microrobotic Locomotion on Diverse Surfaces

Citation

Shum, Jennifer A.. 2025. Electroadhesion Design for Microrobotic Locomotion on Diverse Surfaces. Doctoral Dissertation, Harvard University Graduate School of Arts and Sciences.

Link

https://dash.harvard.edu/handle/1/42719612

Terms of use

This article was downloaded from Harvard University's DASH repository, and is made available under the terms and conditions applicable to Other Posted Material (LAA), as set forth at

https://harvardwiki.atlassian.net/wiki/external/NGY5NDE4ZjgzNTc5NDQzMGIzZWZhMGFlOWI2M2EwYTg

Accessibility

https://accessibility.huit.harvard.edu/digital-accessibility-policy

Share Your Story

The Harvard community has made this article openly available.
Please share how this access benefits you. Submit a story

HARVARD
Kenneth C. Griffin

GRADUATE SCHOOL
OF ARTS AND SCIENCES

DISSERTATION ACCEPTANCE CERTIFICATE

The undersigned, appointed by the

Harvard John A. Paulson School of Engineering and Applied Sciences
have examined a dissertation entitled:

"Electroadhesion Design for Microrobotic Locomotion on Diverse Surfaces"

presented by: Jennifer A. Shum

Signature _____
Typed name: Professor Robert Wood

Signature _____
Typed name: Professor Patrick Slade

Signature _____
Typed name: Professor Kaushik Jayaram

Date: October 28, 2024

Electroadhesion Design for Microrobotic Locomotion on Diverse Surfaces

A dissertation presented

by

Jennifer A. Shum

to

The John A. Paulson School of Engineering and Applied Sciences

in partial fulfillment of the requirements

for the degree of

Doctor of Philosophy

in the subject of

Engineering Sciences

Harvard University

Cambridge, Massachusetts

October 2024

©2024 Jennifer A. Shum

All rights reserved.

Dissertation Advisor:
Professor Robert J. Wood

Author:
Jennifer A. Shum

Electroadhesion Design for Microrobotic Locomotion on Diverse Surfaces

Abstract

Small bioinspired insect-scale microrobots have the potential to someday be useful for exploration or inspection tasks, with their small size allowing for access to confined spaces. However, real-world inspection tasks often involve surfaces of variable inclines and finishes, highlighting the need for small-scale robust climbing options that are adaptable to diverse terrains. In this work we examine development of the Harvard Ambulatory Microrobot (HAMR), a 4.5 cm, 1.5 g microrobot. Improvements to the fabrication process for more robust manufacturing are made, with demonstration of an even smaller scaled (22.5 mm, 320 mg) HAMR-JR robot.

Electroadhesion improvements and robot capabilities are further explored for the purposes of enhancing locomotion and payload capacity over a diversity of pristine, rough, and inclined terrains. On pristine, smooth, flat terrains, improvements using thinner dielectric layers enable fabrication of electroadhesive pads capable of 60 g of shear force (roughly 40 times the weight of a robot). On these smooth terrains, large simple circular foot pads exhibit the greatest shear forces. However, on rougher inclined surfaces, pads which adjusted the width, length, and number of spoke-like features provide greater compliance and achieve more consistent shear adhesion forces. The improved adhesion capabilities of a compliant spoked foot pad are demonstrated with enhanced robot locomotion over steeper 37° inclines on a rough (75 µm vertical and 1 mm horizontal spatial roughness) conductive surface. Further design explorations of various compliant kirigami geometries are conducted to consider spoke, serpentine, and fractal patterns, with a simple model developed for spoke design parameters. Serpentine designs are found to most enhance compliance and shear adhesion capability on rough surfaces (up to twice the adhesion force of circular designs). Several demonstrations of the robot using compliant electroadhesive pads illustrate the potential of the robot to be used in industrial environments, with simple manipulation and locomotion tasks over a variety of conductive rough, inclined, and curved terrains.

Contents

Title Page i
Copyright ii
Abstract iii
Table of Contents iv
Acknowledgments vii

1 Introduction **1**
1.1 Motivation 1
1.2 Outline 2
1.3 Prior Work 2
1.4 Published Manuscripts 3
1.5 Contributions 4
1.5.1 Main Contributions 4

2 Background - Microrobotic Platform and Adhesion **6**
2.1 Small-scale legged robots 6
2.2 Adhesion techniques for insect-scale robots 8
2.3 HAMR Platform 9
2.3.1 HAMR-EA Platform 10

3 HAMR Fabrication Improvements and Scaling (HAMR-JR) **11**
3.1 HAMR Fabrication Overview 11
3.2 HAMR Fabrication and Process Improvements 12
3.2.1 Mechanical Failures 12
3.2.2 Electrical Failures 14
3.2.3 Process Improvements 15
3.3 HAMR-JR: Scaling Down 22
3.3.1 HAMR-JR Fabrication 22
3.3.2 HAMR-JR Performance 28
3.3.3 Future scaling 31
3.4 HAMR Fabrication and HAMR-JR Summary 33

4 Electroadhesive Pad Improvements and Robot Characterization on Pristine Surfaces 35
4.1 Electroadhesion Characterization and Payload Motivations . . . 35
4.2 Electroadhesive Pad Fabrication and Design . . . 37
4.2.1 Standard Pad Design Considerations . . . 37
4.2.2 Dielectric Thickness and Fabrication Exploration . . . 39
4.2.3 Comparison of Electroadhesive Pad Design Performance . . . 43
4.3 Robot-level considerations of climbing payload . . . 46
4.3.1 Robot Pull-Up Tests . . . 46
4.3.2 Robot 'Toppling' Exploration . . . 49
4.4 Pristine Terrain Electroadhesion Summary . . . 52

5 Electroadhesion Pad Design for Rough Inclined Terrains 53
5.1 Rough Terrains & Motivation . . . 53
5.1.1 Overview . . . 57
5.2 Electroadhesive Pad Design for Compliance . . . 57
5.3 Methods . . . 60
5.3.1 Electroadhesive Pad Experimental Test Setup . . . 60
5.3.2 Surface Definition and Fabrication . . . 61
5.4 Experimental Results . . . 66
5.4.1 Data Processing . . . 66
5.4.2 Performance Metrics . . . 67
5.4.3 Electroadhesive Performance of Circular and 'Geometrical' Designs on Flat Terrain . . . 67
5.4.4 Electroadhesive Performance of Circular and 'Geometrical' Design on Rough Surfaces . . . 69
5.4.5 Robot Inclined Climbing Demonstration . . . 71
5.5 Discussion and Summary . . . 77

6 Extended Compliance: Designing Kirigami Patterns for Local Conformation on Rough Surfaces 79
6.1 Introduction . . . 79
6.2 Pad Design and Fabrication: . . . 81
6.2.1 Design Details . . . 81
6.2.1.1 Fixed parameters . . . 83
6.2.1.2 Design-specific parameters . . . 83
6.3 Fabrication . . . 87
6.4 Experimental Electroadhesive Evaluation: . . . 90
6.4.1 Methods: Surface Fabrication and Experimental Setup . . . 90
6.4.2 Parameter Study . . . 90
6.4.3 Spoke Geometry Analysis . . . 94
6.4.4 Serpentine Pad Analysis . . . 99
6.5 Conclusions . . . 99

7 "Real-World" Electroadhesion Demonstrations and Applications 101
7.1 Adhesion on Industrial Rough Surfaces 101
7.1.1 Robot with Spoked EA Pad Inclined Climbing on Aluminum Tooling Plate and Tools 101
7.1.2 Serpentine EA Pad Design Conforming to Large Curvatures on Automobile Transmission 103
7.1.3 Robot with Serpentine EA Pad Design Conforming to Rough Textured Curvatures on Automobile Break Caliper 103
7.2 Gripping and Object Manipulation 106
7.2.1 Prior Work: Piezoelectric Grippers 106
7.2.2 Future Potential Work: Electroadhesive Grippers for Micromanipulation 107
7.2.2.1 Electrostatic manipulation examples 108
7.2.2.2 Self-grounded serpentine pad gripper 109

8 Conclusions 111
8.1 Summary of Work 111
8.2 Future Work 111

Bibliography 115

Appendix A Robot Toppling Avoidance 125

Appendix B Compliant Kirigami Designs: Data Tables and ANOVA Tests 129
B.1 Design Parameters of Various Kirigami EA Pads Investigated 129
B.2 Test of Breakdown Voltage / Shorting of EA Pads 131
B.3 EA Pad Performance Data on Rough Surfaces 132

Acknowledgments

Thank you to everyone who has helped make this thesis possible. Capturing every person who has made a difference in the journey towards a dissertation is an impossible task - but whether listed here or not, thank you all the same.

First, I first want to express a sincere thank you to my committee. Thank you to Patrick, for being such a supportive and encouraging committee member. Thank you to Kaushik, for mentorship throughout grad school. Some of my first research experiences in grad school involved learning to make robots and write papers alongside you, and your insights always push me to consider the challenges and potential of research with greater scope and perspective.

An enormous thank you to Rob, for the many ways you have supported and propelled my journey. The opportunity to dig into rigorous research endeavors, while having the chance to make genuinely cool tiny insect robots in the process, has been an incredible experience. Throughout the process, I have learned that research is far more a winding path of questions and possibilities than a direct answer to be solved – and I have appreciated having a space to ask questions, learn, experiment, attempt things, to fail on occasion, and find the mentorship and guidance to get back on track. Your insights into corners to poke around, ideas on endeavors to try, and feedback on all of my works, drafts, and efforts has been invaluable throughout my journey as a researcher.

I also want to express my thanks to the numerous individuals who provided mentorship, insight, and support throughout my research. Thank you to Perrin, Alyssa, Michelle, and Farrell, as post docs (or now professors) who have gone above and beyond to support my growth as a researcher. Thank you to Rut, Mike, Shuguang, Rizvi, Tristan, Fabian, Pierre-Louis, Elio, Tony, and other thoughtful and collaborative researchers I have had the chance to learn from or work alongside on research. Thank you also to the several undergraduate students including Kahlil, Henry, and Arjun that I have had the opportunity to explore research questions and projects alongside. Thank you to Justin Werfel, for hosting weekly journal clubs that both sharpened my critical reading abilities, and introduced me to far far more interesting bioinspred robots and papers than I would have encountered otherwise. Thank you to cross-discipline researchers and lab equipment experts like James and Greg, whose few minutes of insight can open so many doors and power so much research progress.

Thank you to the members of the Harvard Microrobotics Lab for all of the support, encouragement, academic insight, contribution and suggestion throughout my time in grad

school; being apart of such a collaborative and supportive lab group has made such a huge difference. Thank you to the many grad students who came before me – including Clark, Siyi, Mortiz, Vanessa, Becky, Michael, Emma, Kait, and Ely who shared advice, meals, events, research statement examples, course suggestions, feedback, and countless other life and academic areas. Rm 404 was cozy, but it held some of the most brilliant researchers and scholars that I am lucky to have had the opportunity to learn from. Thank you to the many grad students in the following generations– Andy, Rachel, Christian, Mady, Colter, Lauryn, Neera, and Eva, whose excitement about research and warmth in community have made the SEC building feel like home.

Thank you also to various organizations, including Harvard University and the John A. Paulson School of Engineering and Applied Sciences for providing spaces and collaborators for research, as well as the Department of Defense (DoD) for their funding of work through the National Defense Science and Engineering Graduate (NDSEG) Fellowship.

Thank you to the many incredible communities I have had the opportunity to be apart of during my time as a PhD student – from late night SEAS-GC meetings, to GSAS Residence halls events, to Adams House Carpe's and teas, to HGCC fellowships and meals together, the many individuals and connections I have enjoyed have made the process itself as memorable as reaching any end.

Thank you to my parents, who have supported me on the journey with words of encouragement and advice, hand-me-down textbooks, as well as the occasional food deliveries. Thank you to my brother Andrew, who has always gone before me and paved the path to tackling the world of engineering with just a little more insight and forethought than I would have otherwise. From teaching me to how count numbers in the early days to countless other skills over the years, I cannot imagine where I'd be without all the support that has been shared with me along the way.

1

Introduction

1.1 Motivation

Small lightweight bioinspired insect-scale robots have the potential to someday assist with distributed and robust coverage in area exploration tasks such as search-and-rescue missions, reconnaissance, asset inspection, and monitoring applications. The small size profile of such insect-scale systems can enable these robots to fit into narrow regions or confined spaces which may otherwise be challenging to send a human or larger device. A variety of bioinspired [1, 2, 3, 4] and small gram-scale terrestrial robots [5, 6] have been developed in recent years leveraging novel fabrication techniques that could be used as platforms for such inspection and area coverage tasks.

However, real-world inspection tasks often involve surfaces of variable inclines and finishes, highlighting the need for robust climbing mechanisms that are adaptable to diverse terrains. For example, we could imagine distributed inspection of wear on jet engines, wind turbines, or aircraft where many components are complex and non-uniform, or where wear or debris has created a rough or contaminated surface. For such tasks, robots must have the locomotion capability to adapt to environmental challenges, even when facing potentially rough surfaces or inclined terrains. With the ultimate goal for such distributed inspection tasks being untethered autonomy, onboard control and battery payload requirements may further increase mechanical requirements for robot capabilities and adhesion strengths on inclined terrains. Thus environmental complexities and payload capacity goals motivate a desire to build more effective foot adhesion designs for stronger and more capable small scale robotic locomotion across terrains.

1.2 Outline

The work presented here is organized as follows:

- **Chapter 1** provides an overview and brief introduction to this work.
- **Chapter 2** introduces background information on legged robots, insect-scale ambulatory robots, robotic adhesion strategies, and the HAMR robotic platform.
- **Chapter 3** examines HAMR fabrication processes and implements improvements, with application to scaling down for fabrication of a smaller robot.
- **Chapter 4** explores both electroadhesive pad design improvements and robotic platform capabilities to support additional payloads during inclined locomotion on pristine smooth surfaces.
- **Chapter 5** considers the challenges of adhesion on rough terrains, with experimental testing procedures, surface fabrication techniques, and design explorations of compliant spoke geometries for improved inclined robot climbing on rough surfaces.
- **Chapter 6** extends compliance efforts to exploration of broader kirigami geometry designs as well as understanding of performance based upon the chosen design parameters.
- **Chapter 7** demonstrates electroadhsive pads with enhanced adhesion capabilities on a variety of diverse rough, inclined, and curved surfaces.
- **Chapter 8** concludes with a summary and discussion of potential future work.

1.3 Prior Work

This thesis work builds upon the small insect-scale Harvard Ambulatory Robot (HAMR) platform developed within the Harvard Microrobotics Lab. An extensive number of prior developments have made fabrication and use of these robots possible, including much original SCM, PC-MEMS, and popup techniques [1, 7, 8]. Early versions of HAMR were designed by Baisch et. al, ([9]), with further model and design improvements by Doshi et. al [10], Goldberg et. al. [11], and others. Initial bioinspired explorations of

inclined insect-scale climbing [12] have been followed by initial HAMR-E electroadhesive robot development by Rivaz et. al. [13].

1.4 Published Manuscripts

This work draws on a collection of work completed collaboratively with other contributors to the HAMR platform and robot studies, with contributions to the following publications. Copyright belongs to respective publications (IEEE [1], IOP Publishing) that have allowed reprinting with permission from papers referenced below:

- **J.Shum**, P. E. Schiebel, A. Hernandez, and R.J. Wood, (2024). "Electroadhesive Pad Design for Increased Adhesion Capability of Climbing Microrobots on Diverse Terrains" IEEE Robotics and Automation Letters, Vol. 9, No. 12, 11569 - 11576. ©2024 IEEE

- **J.Shum**, P. E. Schiebel, A. Hernandez, K. Jayaram, and R.J. Wood, "Compliance for Adhesion: Designing Kirigami Patterns for Local Conformation on Rough Surfaces" *[Under Review]*.

- A. Hernandez, P. E. Schiebel, **J.Shum**, and R.J. Wood, (2024). "Spines and Inclines: Bioinspired spines on an insect scale robot facilitate locomotion on rough and inclined terrain." Integrative and Comparative Biology. © 2024.

- P. E. Schiebel, **J.Shum**, H. Cerbone, and R.J. Wood, (2022). "An insect-scale robot reveals the effects of different body dynamics regimes during open-loop running in feature-laden terrain". Bioinspiration & Biomimetics, 17(2), 026006. © 2022 IOP Publishing

- P. L. Lechère, P. E. Schiebel, M. C. Yuen, **J. Shum**, and R. J. Wood, (2022). "Passive compliant foot design for improved micororobotic mobility on rough terrains," in

[1] In reference to IEEE copyrighted material which is used with permission in this thesis, the IEEE does not endorse any University products or services. Internal or personal use of this material is permitted. If interested in reprinting/republishing IEEE copyrighted material for advertising or promotional purposes or for creating new collective works for resale or redistribution, please go to *http : //www.ieee.org/publications*$_s$*tandards/publications/rights/rights*$_l$*ink.html* to learn how to obtain a License from RightsLink. If applicable, University Microfilms and/or ProQuest Library, or the Archives of Canada may supply single copies of the dissertation.

2022 IEEE/RSJ International Conference on Intelligent Robots and Systems (IROS), Kyoto, Japan. © 2022 IEEE

- T. Abondance, K. Jayaram, N. T. Jafferis, **J. Shum**, & R. J. Wood, (2020). "Piezoelectric grippers for mobile micromanipulation." IEEE Robotics and Automation Letters, 5(3), 4407-4414. © 2020 IEEE

- K. Jayaram, **J. Shum**, S. Castellanos, E. F. Helbling, & R. J. Wood, (2020, May). "Scaling down an insect-size microrobot, HAMR-VI into HAMR-Jr." In 2020 IEEE International Conference on Robotics and Automation (ICRA) (pp. 10305-10311). © 2020 IEEE

1.5 Contributions

This thesis examines the mechanical design and fabrication developments required to enhance locomotion capabilities of microrobots on diverse rough, inclined, and real world terrains. Specifically, I present the following contributions:

1.5.1 Main Contributions

- Improvement and streamlining of general HAMR manufacturing processes and best practices for more reliable fabrication. These methods are applied to enable the fabrication of a functional small-scale microrobot at 2 cm length-scale, one of the fastest and most highly dexterous robots at this size scale.

- Exploration of design parameters and improvement of fabrication procedures for circular unipolar electroadhesive pads, with characterization of design performance on pristine smooth conductive surfaces to identify a pad process and design that far exceeds pure adhesion requirements of gram-scale robots.

- Characterization of robot mechanical capabilities and strategies for locomotion with added payloads on inclined surfaces, with development of pull-up test characterizations and center of mass toppling explorations that can support future onboard developments.

- Fabrication methods and experimental test procedures for testing electroadhesive pads on rough (micron to millimeter feature variation) conductive terrains. Experimental

characterization identifies improved performance with compliant spoked foot pads, augmenting robot ability to achieve climbing locomotion on higher degree inclines of rough terrains.

- Design exploration of a range of compliant kirgami patterned geometry designs for integration with conductive electroadhesive foot pads, including development of a simple bending beam based model which considers fabrication and geometric design limits to understand general trends in behavior of design parameters. Longer serpentine design patterns are identified for higher compliance and performance on rough terrains.

- Demonstration of robot locomotion with enhanced electroadhesive pads over a variety of inclined, rough, and curved conductive substrates, illustrating the potential for such devices to be utilized on more challenging surfaces in potential inspection tasks in the future.

2

Background - Microrobotic Platform and Adhesion

2.1 Small-scale legged robots

A wide range of highly dexterous and capable robots exist for legged locomotion, many with potential capabilities to explore rough or rugged environments. A variety of research platforms such as the Cheetah robot (MIT) [14] or Stanford Doggo (Stanford) [15], and commercial and industry platforms such as Big Dog/Spot (Boston Dynamics) [16] and Vision (Ghost Robotics)[17] in development have already demonstrated impressive legged locomotion capabilities. While perhaps not quite as fast as the biological counterparts these robotic systems may be inspired by [18], such robots have thus far tackled challenging maneuvers, reached relatively high speeds of locomotion, and navigated a diversity of tasks and scenarios. However, many of these highly capable robots rely on multiple actuators, sensors, and mechanisms for their capabilities, which all must be added on to the payload of a robot.

Leveraging novel fabrication techniques, various small-scale microrobots have recently been developed with the intention of deploying them in diverse environments for cannonical uses including search and rescue, hazardous environment exploration, and environmental monitoring [11, 19, 20, 21, 22, 23, 24, 25]. Their small scale can make them particularly well suited to regions where access to confined or tight spaces is helpful [26, 27]. However, the trade-off of a smaller size constraint is that less complexity can generally be incorporated. Many of the smallest of ambulatory robots can have reduced degrees of freedom and dexterity compared to their larger robot counterparts, and also have much lower

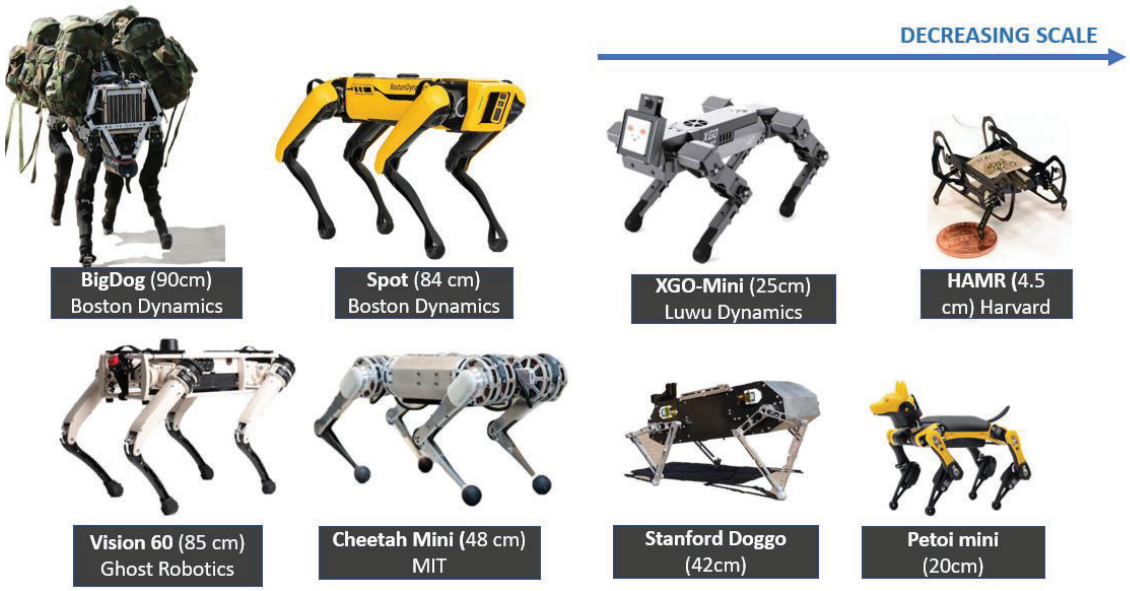


Figure 2.1: Legged Ambulatory Robots: a variety of legged robots exist, some (such as Big Dog) [16] with the capability to navigate rough terrains, albeit at a much larger scale than microrobotic devices.

payload capacities. Achieving particular locomotion strategies or hardware developments for the navigation of challenging environments with such small-scale robots may thus require particular consideration of processes, techniques and methods which can work best at different scales, as we consider with the case of adhesion for climbing locomotion.

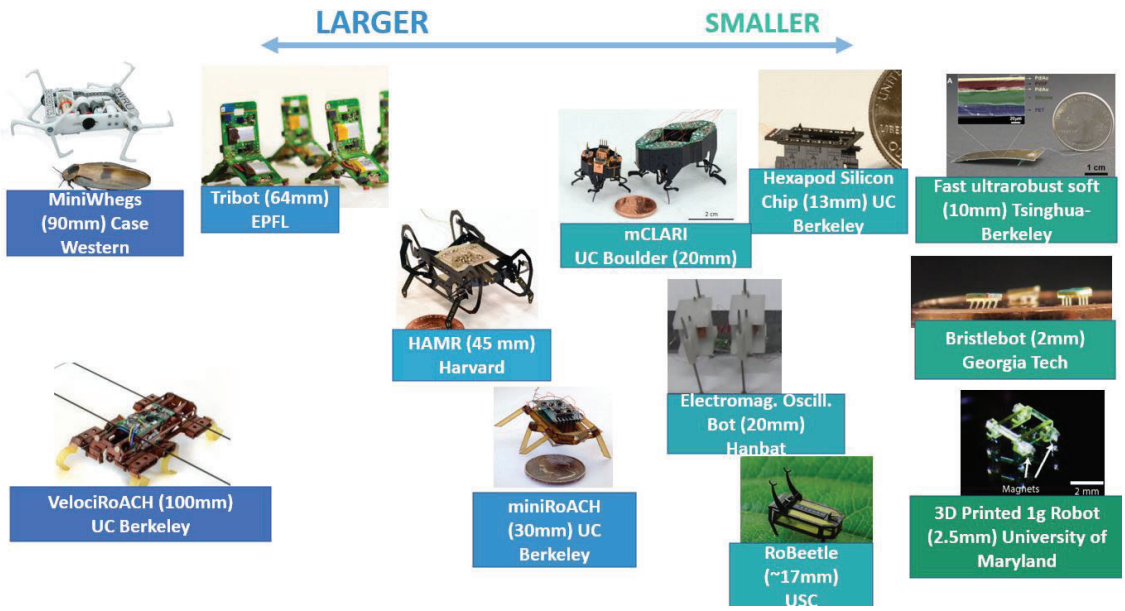


Figure 2.2: A wide range of small insect scale robots have been developed. Small robots often trade off locomotion dexterity and capabilities for size.

2.2 Adhesion techniques for insect-scale robots

While a variety of adhesion techniques have been used in robotic applications, such methods come with limitations on the environments and scales they can be used within. For example, suction and magnetic end-effectors may come with operating pressure requirements or surface constraints, with usage only possible on smooth, nonporous, or magnetic materials [28]. These methods also face the challenges of scaling both the adhesion technology and any required peripherals (e.g., pumps) to use at the scale of centimeter-size robots. Other bioinspired techniques include frictional contact appendages (claws, spikes, spines, etc.), chemical adhesives (glues), van der Waals force-based dry adhesion (gecko) fiber designs, and other such concepts seen in smaller organisms found in the natural world [29, 30, 31, 32, 33, 12]. Biological organisms often display diverse foot designs that can be attributed to a particular locomotive adaptation. While the pad geometry and surface morphology is diverse, the overall compliance of pads in climbing insects (e.g., grasshoppers, cockroaches) plays an important role in the ability to conform to rough surfaces. [34, 35]

However, such friction-based techniques may have limited incline capabilities, and fabrication of complex dry adhesion designs remains nontrivial. Capillary adhesion has been likewise explored previously on HAMR with several speed and reliability benefits, but with

the limitation of climbing up to at most 30 degree inclines [36].

To navigate challenging terrain in these scenarios, several example robots utilize electroadhesive pads for situations that require switchable adhesives, such as perching after flight [37] and climbing [13]. Electroadhesion [38, 28] presents the potential for achieving steeper climbing inclines than passive frictional approaches, on-off controllability using voltage signals alone, the capability to be used across a range of varying pressure or surface conditions, and can furthermore be fabricated with the simplicity and ease of using the same 2D layer fabrication techniques as the base robot. Thus for its ability to be used in a range of environmental conditions, electroadhesion is chosen here as a means of adhesion relevant for potential microrobotic inspection applications.

Amidst the larger diversity of electroadhesive robots that exist [39, 28, 38], the scalability of electroadhesion lends itself especially well to such microrobotic applications, where small (mm to cm) features can enable light (mg to g) microrobots to achieve strong adhesion forces. As robots scale down to smaller and smaller sizes, the volume and weight of such robots would decrease faster than their surface area. With electroadhesive techniques relying on surface area, this suggests that smaller microrobots could take advantage of such methods more effectively at small scales.

2.3 HAMR Platform

In this work, we utilize the Harvard Ambulatory Microrobot for our studies. HAMR utilizes a multi-layer laminate pop-up MEMS fabrication technique [40] and piezoelectric actuators, which results in a lightweight (1.5 g) and dexterous robot capable of multiple gaits and speeds [10, 41] at a small scale (4.5 cm) [42]. This platform has demonstrated the ability to achieve locomotion across varied environments, utilizing swimming [43] and electroadhesion for climbing [13], as well as untethered locomotion suited for use outside the lab [11]. HAMR has eight independently controlled degrees of freedom, including swing and lift for each leg. The small size paired with relative dexterity make the HAMR platform ideal for legged locomotion tasks at small scales, with the hope of being able to use the robot for someday accessing and inspecting confined spaces that may otherwise be inaccessible to humans.

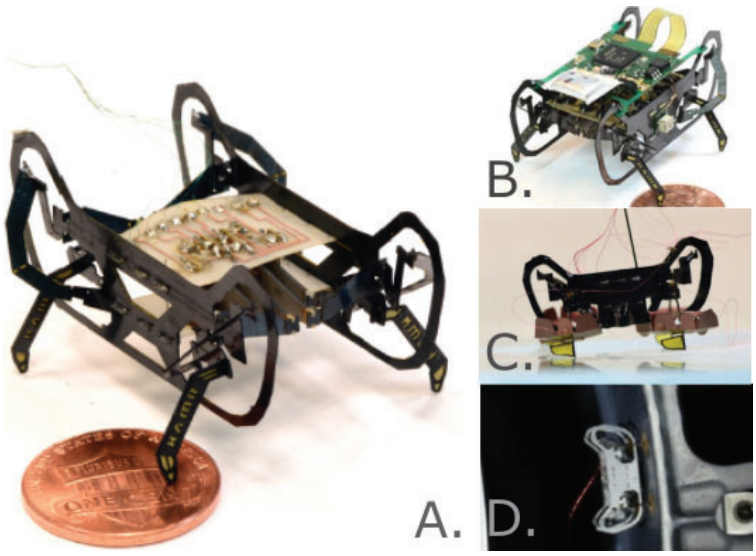


Figure 2.3: HAMR Robot: this 4 cm robot has been used for high speed locomotion, with versions made for (B) autonomy and control, (C) swimming in watery environments, and (D) electroadhesive inspection.

2.3.1 HAMR-EA Platform

HAMR-E has been previously developed by Rivaz et. al. for the purposes of electroadhesive locomotion [13]. This work established a foundation for exploring electroadhesive work within the HAMR platform, including an initial fabrication method for electroadhesive pads, a three-legged tripod gait for climbing locomotion, and compliant multi-DOF (roll, pitch, yaw) ankle joint legs for ankle-level compliance of a full flat pad.

However, previous electroadhesion work for HAMR has focused primarily on flat pristine terrains [13] with only brief variable terrain demos, leaving room to improve electroadhesion capabilities on non-uniform rough terrains. In particular, we consider that more rigorous approaches to characterization can help us to explore performance of pads on rough terrains, where adhesion is decreased in magnitude. We also note that the robot design used standard circular footpads, which do not necessarily adhere well to rough uneven surfaces, and presents the potential for improvement. Being able to improve the robot adhesion abilities could help unlock improved locomotion and climbing capabilities over rough and diverse terrains, ultimately enabling these robots to reach more spaces relevant for eventual exploration and investigating tasks.

3

HAMR Fabrication Improvements and Scaling (HAMR-JR)

3.1 HAMR Fabrication Overview

In order to achieve locomotion over diverse terrains with a robot, we must first build a base robotic platform to enable such locomotion. HAMR as a lightweight legged robotic platform is well-suited to climbing inclines, with legged robots having the dexterity capability to tackle potential environmental heterogenities with more specific situationally-tuned gaits than wheeled or tread robots. The dexterity of HAMR enables bioinspired pronk or trot gaits to be be used for flat ground running, with the ability to switch to tripod insect-inspired gaits, which move one leg at a time to be used for more stable adhesion-based climbing.

However, despite the benefits of their potential dexterity, such legged robots can also come with additional complexity in fabrication. Particularly when considering the small, lightweight, fast, and controllable piezoelectric actuators which enable precisely controlled swing and lift degrees of freedom for the robot, the fabrication process can be long and challenging.

In this section, we examine the following: (1) A brief introduction to the overall HAMR platform fabrication. We identify existing fabrication challenges and failure points of the process, and develop a list of potential solutions and improvements for streamlining, with particular focus on the piezoelectric actuators, and (2) application of this overall process towards development of a half-scaled HAMR-JR (2 cm) version of the robot, the smallest version of these highly dexterous HAMR robots fabricated to date.

3.2 HAMR Fabrication and Process Improvements

Many researchers have worked on the HAMR platform previously to construct a foundation for the design and fabrication of the system, from initial application of Smart Composite Microstructure (SCM) [7], pop-up [8] and Printed-Circuit MEMS (PC-MEMS) processes to create some of the earliest prototypes of HAMR legged robots (Baisch et. al.) [44, 20], as well as enable more recent work exploring power autonomy and control [11, 45, 41]. The generalized process consists of laser cutting individual material layers, curing a combined layup of these aligned materials, then release cutting out final parts to fold, attach, and assemble as needed. This general lamination process is used for both structural (chassis) and functional (actuator) components.

However, actually making these microrobots in practice consists of a variety of nuances and techniques across multiple areas of actuator fabrication and robot assembly. Here we focus on fabrication of one of the latest designs, HAMR-VI, from prior work by Doshi et. al [10], made with the pre-stacked ('PS') style actuators. This process includes an initial pre-stack of alumina and PZT materials aligned in a jig, such that they can be readily layered. Pre-stack layering is followed by a two-cure process: the first cure adheres two PZT prestack layers to each other for the bimorph design, with a central carbon fiber signal layer in the middle, and alumina structural components at the base and tip of the PZT. The second cure attaches copper for traces, alongside bridges which connect bias and ground to their respective PZT surfaces. Rastering steps isolate traces and provide a via hole channel to the central signal layer, while release cut steps isolate individual actuators from the aligned layup, followed by conductive epoxying of the signal via hole and trace. While this process produces lightweight ($\tilde{1}$00 mg each) and high performance (247 μm deflection, 270 mN force) actuators [10], making these in large quantities remains a challenge. In particular, we identify several potential practical process challenges with mechanical delamination, cracking, and electrical failure, as detailed in the following sections and visually summarized in Fig. 3.1.

3.2.1 Mechanical Failures

Several potential failures can occur mechanically when fabricating actuators: delamination between layers, uneven cutting or rastering of designs, misalignments of layers during layup, and cracking of materials. Delamination can occur between any of the inter-

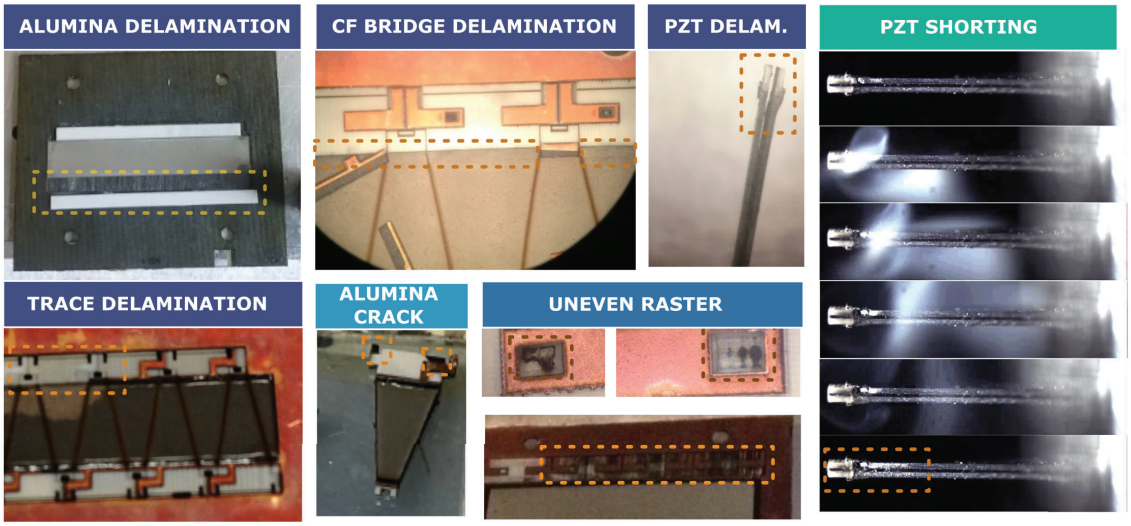


Figure 3.1: Actuator Challenges: Delamination of alumina, carbon fiber bridges, PZT, and copper traces can all occur as a result of poor connection and bonding between layers. Uneven rastering and alumina cracking can occur from laser setup and settings. PZT shorting can occur from a variety of sources - including design files, laser cut order and settings, cleanliness, and test procedure. Dotted lines outline the failure point within each respective photo.

faces and at multiple stages throughout the two-cure, raster, release and assembly process. Potential delaminations as shown on the left side of Fig 3.1 include: (1) initial alumina-central carbon fiber interface during first cure; (2) copper trace to alumina interface during second cure, or after raster when surrounding material is removed; (3) carbon fiber bridge to alumina interface after release when supporting structure is removed; and (4) PZT to PZT delamination (during first cure, or after final release). While occasionally some delaminations can be fixed throughout the process by adding CA or conductive epoxy as needed depending on whether it is a purely structural or electrical connection, the fastest method for the most robust and lightweight actuators would ideally avoid relying on individually fixing numerous connections after initial fabrication.

In addition to delamination challenges, there can also be mechanical difficulties with materials cracking or remaining where unwanted. Alumina base prongs and tips needed for robot assembly attachment can crack during final release, fixturing, and assembly into the robot. Rastering of the via holes (for electrical connection to the central carbon fiber signal layer) can be uneven, and easily cut all the way through the central carbon fiber

layer, or raster only portions of the hole away. As before there is the potential to 'fix' less than ideal structural components - either gluing alumina pieces back on, or using a sharp tool to scrape out the remainder of an uneven raster, though these still present less ideal solutions for structural and electrical robustness. Some challenges including delamination of the PZT itself, poor re-alignment leading to shifted cuts, and/or poor release such that the PZT cracks during cleaving steps, result in needing to remake the entire layup.

3.2.2 Electrical Failures

Beyond primarily structural challenges of fabrication that can at least be apparent throughout the fabrication process, electrical failures are often only evident after fabrication of a batch when completed actuators can be tested. When electrically testing actuators, each actuator is individually attached to ground (constant), bias (constant) and signal (sinusoidal) voltage signals which induce the piezoelectric material to bend upwards or downwards according to the signal input.

Weak deflection can occur as a result of a poor connection - due to aforementioned delamination which might prevent adequate conduction through the carbon fiber interfaces, or as a result of other poor contact. Conductive epoxy may not have made full contact within the signal via hole to secure a reliable connection to traces, or contact to the external voltage sources (either via test jig or soldered to the robot circuit board) may be spotty. Weak deflection could also potentially occur as a result of misaligned poles and biasing of the two PZT plates. Positive and negative sides of the PZT must be kept track of carefully such that the positive and negative sides alternate as anticipated in the two-layer PZT layup. While post-fabrication re-poling can align the charges as well, the performance may not be as strong as when kept consistent with the original polarization orientations.

Electrical shorting can also occur, with a number of potential causes. The most direct cause of shorting can be the result of overly high-powered laser cutting - this could damage the crystalline structure and cause shorting. Previous research has found dielectric strength to decrease with increased cutting power (approx $> 6.4\text{V}/\mu m$ cleaved, $3\text{V}/\ \mu m$ cut through at 0.4 W and $1\text{V}/\mu m$ cut through at 0.63 W), which may be a result of localized melting, causing chemistry composition to change around the cut area with PVD-like evaporation of certain constituent metals [46]. Shorting can also come from other laser-related causes beyond the intended directly designed PZT cuts - for example, when

cutting the alumina sections with the higher powered settings to cut through the strong structural material, cuts closely adjacent to and intersecting with the PZT can similarly cause shorting. Some laser systems may dwell longer in corners or turns, further adding to the potential for overpowered cutting on the sensitive PZT material.

Beyond laser damage to the material structure of the PZT itself, the potential for shorts as a result of unintended connection between the two sides of the bimorph actuator can also occur. Loose carbon fiber strands from the central signal layer (or other bits of debris, such as strands from cleaning cloths/microbrushes) could inadvertently cause one side of the actuator to short to the other side. When assembled into a robot, shorts can also potentially occur from one actuator to another actuator as a result of the conductive carbon fiber at the tips attaching to carbon fiber linkages.

Actual usage can cause electrical shorting to occur as well. When initially testing actuators, they must be carefully ramped up to the intended operating voltage (250 V) rather than used immediately at intended voltage. Overloading of actuators (via payload or obstacles) can further cause shorting, and overextension of a robot during use can cause cracking of the actuators. Since structurally the actuators have a carbon fiber layer for applied voltage signal in the center of two PZT layers, with separate ground and bias signals on the outer surfaces of the PZT bimorph, mechanical cracks and debris can increase the likelihood of conducting from a surface to the center and inducing electrical shorting.

All of these mechanical and electrical failure modes can make the practical fabrication of these piezoelectric actuators challenging (both in identifying the exact causes for failure and resolving the underlying problems), thus leading to our implementation of the following process improvements.

3.2.3 Process Improvements

In order to address the above challenges, we identify several practical yet important elements of fabrication that are important to pay attention to and consider in the fabrication of these small scale systems, as summarized in Fig 3.2. Some of these steps were added in the HAMR process with reference to and implementation of methods of Jafferis et. al. [46] while others were identified through repeated fabrication, observation and testing.

1. Material Supply Assessment: Assessing the state of materials to ensure they are used as intended is one important step to ensuring well-bonded laminate layups.

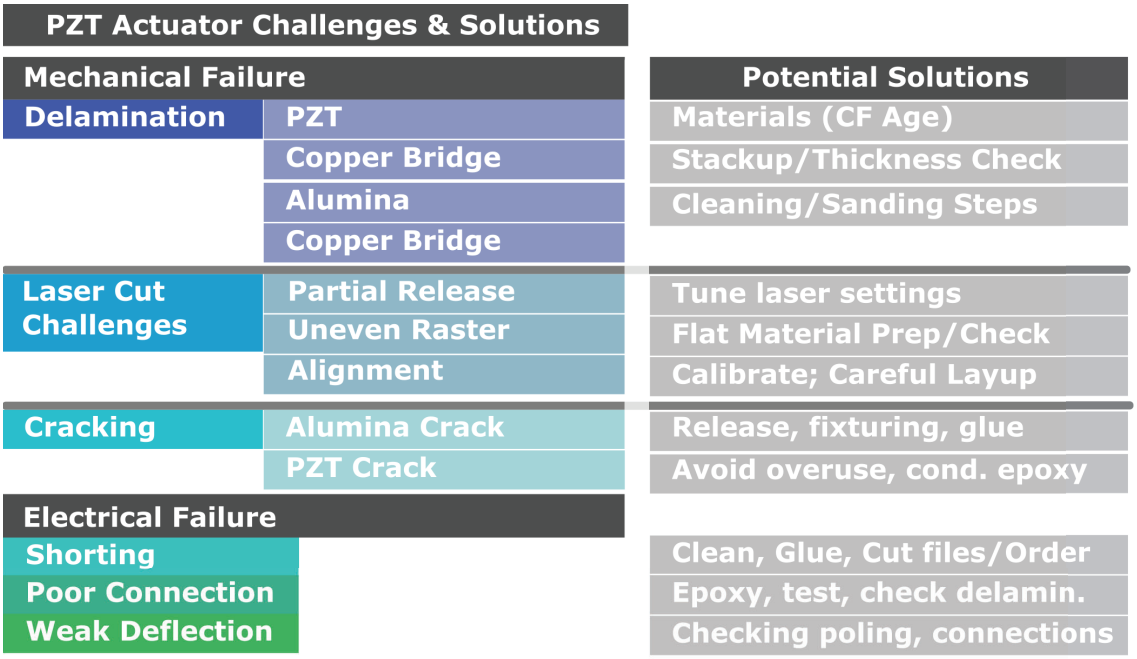


Figure 3.2: Summary of Prestack Actuator Fabrication Challenges and Potential Solutions: A variety of materials and layup checks, laser setting and design file tuning, cleaning steps, gluing, and checking steps can be used to streamline and improving existing challenges.

In particular, it is useful to ensure that uncured carbon fiber (used for structural rigidity and conductivity when cured, but also providing the resin used for bonding and adhesion of actuator layers while still uncured), is fresh and in functioning condition. Visual checks were conducted to ensure sections were selected with minimal striation/fiber gaps, and no 'wetness' was apparent. While desiccant packets were used within tightly sealed zip lock bags, some amount of moisture in the bag could lead to condensation upon removal from refrigeration, ultimately leading to a top piece of carbon fiber or sheet edges getting wet. A general tactile observation of 'tackiness' was also useful when removing cut layers of uncured carbon fiber from the backing. The overall age of carbon fiber could be considered as well, with particular attention given to check older supplies. As carbon fiber resin dries out over time and sheets potentially get wet from repeated defrosting and refrigerating, individually portioned sheets of carbon fiber may need replacing (from bulk roll supply kept in deep storage or original suppliers). One portion of carbon fiber within a particular batch might work well while another might not, so checking that the specific material used still has tacky resin can ensure that curing occurs as intended to bond all the layers together.

When working with the uncured carbon fiber, we further ensure that the press layers used for curing during the actuator process includes not just the standard elements (layers of Kapton polyimide film, silicone, steel shim, and pacopad (Pacothane Technologies) for heat and pressure distribution), but also additional layers of FEP (Dupont, fluorinated ethylene propylene), which help keep the pacopad from absorbing additional resin which may help bond the layers.

After curing a layup, we can also visually check the results of the 2-cure layup before continuing with the remainder of steps to see how much resin flow occurred. For example, in the Fig. 3.1 visualization of the trace delaminations, we can note the lighter (no-resin) element of the PZT directly below the failed traces, compared to the darker PZT elsewhere which did not experience immediate delamination. While not necessarily a direct correlation with how well adhered layers are or whether delamination will definitely occur, this can provide a useful early check of general carbon fiber quality. If for some reason a sufficient supply of quality carbon fiber can not be obtained, future efforts could explore relying upon additional glues and epoxies to supplement the carbon fiber resins in bonding adhesion.

Beyond carbon fiber materials, the thicknesses and tolerances of other materials are also critical for a pre-stacked jig process. An FR4 jig is used for alignment of the PZT and alumina, with alignment tabs and thinly cut 'springs' such that these materials can be pushed flush with each other within one in-plane pre-stack layer. This full layer layup can then be laid up twice, and sandwiched around both sides of a central carbon fiber layer to create the two-layered PZT actuator layup. This assumes that the FR4 jig is roughly equal to (or thinner than) the thickness of the other PZT and alumina materials being laid up for a level surface for carbon fiber adhesion. In practice, however, with the tolerance of the commercially-available FR4 thickness (0.005" or 0.127 mm), the resulting material could often be thicker (0.14 to 0.18 mm). This larger thickness could create a gap in the layup, wherein the carbon fiber did not adhere well to the PZT and alumina. To avoid delamination, thickness checks with a micrometer were conducted on every batch ordered, and only material sufficiently thin enough (0.14-0.15 mm) was used, thus ensuring adequately flat and uniform thickness pre-stack layers.

Ensuring that the materials are aligned properly within the entire layup is also important - when using jigs, all prongs and mating areas are checked carefully to ensure that no layers are overlapped with each other. Closely pressing FR4 jig spring parts are also

cut off and removed before actual layup, with pieces held in place by the gelpack. When using weight stacks, care is taken to ensure appropriate placement for centered loading for even curing across the entire area of the layup.

Thus, by checking both carbon fiber quality and material layup thicknesses when using a prestack process, many delamination challenges can be avoided.

2. Laser Cut Settings and Design File Adjustment: By adjusting and carefully tuning the laser cut settings and design files, challenges of shorting and/or potentially cracking actuator elements can be addressed. As mentioned, high power cutting can damage PZT materials, reducing their dielectric breakdown strength and causing shorting. To prevent this, it important that the cutting power is measured prior to use and kept low enough that it avoids this shorting, referencing actuator sources for previously determined appropriate power settings (for example, 0.23 W for the majority of PZT cuts and 0.63 W for minimal high-powered PZT edge treatments) [46].

Beyond the laser cut settings, it is also essential that any higher power cuts potentially intersecting with or very near the PZT material (such as those for alumina cuts) are conducted first. This step can then be followed by the appropriate PZT cut settings which can remove damaged PZT material from the area. Since the alignment of the laser system is never perfect (even when incorporating careful steps adjusting alignment cross fiducials for both translational and rotational re-alignment, as well as accounting for camera thermal drift, there may still be 10's of microns of error), being able to perform these cuts directly one after the other without shifting the piece in the middle ensures accurate cuts. We also adjust the design file to ensure that PZT cuts fully extend into the alumina cut regions, again to ensure that lower power cuts can cut away any potential PZT, even with the potential of slight misalignment. As can be seen from Fig. 3.1 we see that the shorting is initiated near the alumina tip-PZT interface in the shown example, likely caused by PZT material that was slightly cut with higher powered alumina settings. This shorting occurred throughout entire batches, but with revised design files (Fig. 3.3) and cut order procedures this challenge disappeared. Those laser systems which dwell in corners may further require tweaked settings or cut design files that loop around edges to avoid overpowered cutting on the sensitive PZT material.

Despite the importance of avoiding overly highly powered cuts, care must be taken to also ensure that enough power and passes are used, otherwise the opposite problem of undercut layups can occur. This can cause mechanical cracking and fracture during release

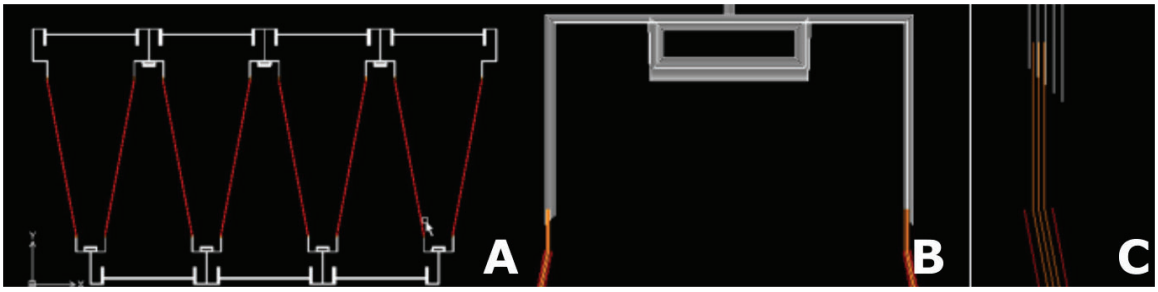


Figure 3.3: Actuator Design File Adjustments: A) Full view of actuator release cuts, including alumina (white), low power PZT (orange), and high power PZT edge-treatment (red) cuts. B) A closeup view of adjusted actuator tip design: a large number of cuts are added for the alumina (rougly 8-15 cuts spaced 5-10 μm apart. Multiple lines - both for PZT and alumina, help material to cut through all the way and avoid cleaving in the end (or potential fracture/cracking of features). C) An even closer view specifically of the PZT to alumina interface, where PZT low powered lines extend into the alumina cut region.

steps. By tuning not just power but also frequency, speed, number of passes, number of designed lines (with multiple closely spaced cut lines enabling easier releases), and z-focus height (for thick layups, focusing into the cut as it progresses can also improve release), laser recipes which can adequately and reliably cut through with lower power can be developed. While laser power can fluctuate and decrease over time, by adding additional passess and lines to cut recipes, batches can still be released reliably and avoid potential need for cleaving in the end, albeit a little slower and potentially at the cost of cutting through underlying Gelpak substrates. Trading off a little speed for additional reliability in fabrication makes for a more robust process overall, and enables batches to be completed more consistently.

With careful attention to the laser cut settings, the alignment and order of cuts, and the design around PZT, we can thus both avoid electrical shorting and ensure more reliable releases cuts of actuators.

3. Pre-cut layers and leveling: In addition to carefully tuning laser settings, pre-cutting layer features where possible can save on the need to precisely tune layer cuts during the more careful full layup cuts. For example, rastering steps can come out uneven both when removing copper from non-trace sections of the actuator, as well as when rastering the via hole channels which allow for a connection to the central signal carbon fiber, as shown in Fig. 3.1. These uneven raster cuts often occur as a result of slightly non-level surfaces when rastering. While in the first case, the alumina can simply be rastered down further until a clean raster is achieved, this is less than ideal —it not only takes more time

and more passess to do this more times, but also slightly decreases the thickness of the alumina in those areas, making it potentially more likely to crack or fracture if too thin. In the second case of via hole rastering, the central carbon fiber layer is very easily cut through (requiring much lower cut settings than the alumina being rastered on top of it) and may be removed entirely if over-rastered. Using thinner alumina layer for reduced alumina rastering is also not ideal, as having all the components of the actuator pre-stack approximately equal in thickness for a level layup is helpful to avoid uneven pressure. In the event that carbon fiber in the via hole is over-rastered, conductive epoxy may in theory still be applied as long as connections are made carefully to the edges of carbon fiber that still exist at the rastered hole edges for later signal conduction. However, ensuring a strong connection to these edge strands is harder than having an entire carbon fiber bottom surface of the hole to make a strong connection to for later electrical conduction.

One potential option to help both cases is to precisely level the layup before laser rastering. In general, layer flatness and leveling is important for accuracy of cuts, and great care is always taken to adhere materials to Gelpak mounted onto flat glass slides when preparing. Nevertheless, there can still be some very minor amount of unevenness from one side of the piece to the other (potentially due to laser fixturing, or perhaps the part itself if the taped down layup was just slightly uneven on one side/has bumps and features as it becomes more rastered and patterned itself, etc.). By visually checking with a camera in all directions prior to rastering, any slight out-of-focus areas can be identified and adjusted (using very thin kapton shim or otherwise on the order of microns to tens of microns) to ensure a fully level and in-focus image prior to laser rastering. This can work reasonably well for improving large-scale regions, such as those areas rastered away to create the copper traces, however very tiny via holes with less area (considering potential hole diameters on the order of hundreds on microns, and laser spot resolution on the order of tens of microns) may have decreased rastering area, such that the laser resolution limits become more noticeable. With the challenge of these small area regions being spaced with relatively large lateral mm distances between individual holes that may cause vertical focus discrepancies, features can raster unevenly.

Another option, particularly for these via holes, is to precut them into the alumina material itself as part of initial prestack stages. This removes the need to time the cut settings exactly, as the Gelpak beneath used just for single layer material fixturing can be overcut a little, unlike the very easily rastered carbon fiber of the full layup. While

it does require keeping close track of the orientation of pre-stack layers if designs are not symmetrical, this pre-cut hole creates much cleaner connection points for later conductive epoxy connections. Very light rastering can be done after the second cure step to remove any potential resin overflow that may cover the via hole, but requires much less power than trying to raster through alumina as in prior process steps. Future efforts could also consider pre-cutting the copper traces (and the carbon fiber beneath them) in the desired final trace shapes rather than performing a raster on the layup. By checking the leveling and pre-cutting the via hole designs, challenges of uneven rastering can be avoided.

4. Consistent Cleanliness: Ensuring clean surfaces should further improve both structural bonding and reduce risk of unintended shorting due to contaminants. In addition to nitrile glove PPE to reduce potential human contaminants of potential oils or debris when handling materials, all materials should be kept on clean surfaces. Structural materials (such as alumina or cured carbon fiber/FR4 in non-actuator processes) can be sanded and sonicated prior to a layup to further enhance ability to achieve surface adhesion. Cleaning with IPA and kimwipes, cotton swabs, or microbrushes should be completed after cutting materials or release layups, as laser cutting or rastering steps create a reasonable amount of material charring and debris. Additional care should be taken to regularly inspect parts under a microscope for debris (either from laser, from external sources, or from the cleaning brushes themselves- which can leave strands or fibers depending on their type). Careful cleaning of the edges of released actuators is also essential after release, as slightly undercut central carbon fiber layer strands can create 'fuzzy' edges that can bend between the two PZT plates. By consistently cleaning parts and keeping them clean at all stages of layup and final assembly, delamination and shorting due to external debris can be avoided.

5. Edge CA Glue: Addition of non-conductive cyanoacrylate glue to the edges of PZT actuators can improve their breakdown capabilities [46], and seals the edges from any stray debris that could short across the edge. CA glue is also added to the tips of the actuators to prevent inter-actuator shorting through chassis components. CA glue added lightly just to the edges of copper traces can also help to add structural bonding to the alumina in case of weak carbon fiber resin connections.

6. Documentation: Keeping careful notes and updating a 'HAMR handbook' of step-by-step changes can further be helpful for the fabrication of these systems. Often times the fabrication process has multiple steps to follow, conventions to keep track of (with both PZT orientation and via hole orientation, and setting/alignment details to keep in mind)

and reducing human sources of error via checklists and references can avoid errors which can require restarting of a batch.

Without any single one of these improvements, we note that it can still be possible to make actuators. A gap due to material thickness variation or slight debris due to cleanliness issues may matter less if the carbon fiber is exceptionally fresh and adheres well, or a somewhat close high powered alumina cut may miss hitting the PZT and causing a short given opportune alignment in that area. Nevertheless, by implementing all of the above fixes and considering them during the fabrication process, it improves the chances for success and reliability with actuators, as will be demonstrated by the actuator fabrication of the following HAMR-JR section.

3.3 HAMR-JR: Scaling Down

Work on HAMR-JR published in "Scaling down an insect-size microrobot, HAMR-VI into HAMR-Jr" [42] was done in collaboration with K. Jayaram et. al, who contributed the primary component of performance characterization and analysis of the new scaled-down system.

We implement the design of HAMR-VI with the fabrication process improvements described above and demonstrate the full fabrication of a half-sized version of the robot, "HAMR-JR". The robot was scaled allometrically —the designs are scaled down equally in length and width, while the thickness of the materials used was kept the same due to availability of material resources. Within the design files, this required scaling all designs down to 0.5 times the original size, then re-editing each flexure width to be larger such that the flexure gaps (which are adjusted to leave room for the material layer thickness) were the same as the original designs.

3.3.1 HAMR-JR Fabrication

An overview of the entire detailed fabrication process for this half-scaled version of the robot, largely derived from previous efforts for the HAMR platform, can be seen in Fig. 3.4. In summary, the procedure is as follows:

1. **Chassis**: The chassis components are made from an 11-layer laminate consisting of cured carbon fiber (strong and lightweight structural component), FR1500 Pyralux ad-



Figure 3.4: Fabrication of HAMR-JR: The process consists of: 1) Chassis fabrication, including both 11 layers of material cuts and layup as well as 2) cure, release, de-chipping and popup. 3) Actuators are made using a pre-stack process, with 4) a two-cure process, raster and release cuts, conductive epoxy application, and testing. 5) Circuit boards are made with laser rastering and etching processes, with hand-insertion and soldering of actuators. 6) Finally, full assembly of chassis, circuit board, and actuators is completed, with final popup assembly, tethering, and testing before legs are added.

hesive (bonding component), and Kapton polyimide film (flexure component). Parts are designed in 2D CAD software and cut using a precision laser (355nm UV laser, DPSS or Oxford system) with an approximately 10 μm beam width. Carbon fiber pieces are thoroughly cleaned with isopropyl alcohol and sonicated after laser cutting, and all layers are carefully 'de-chipped' under a microscope to ensure removal of all undesired material remnants that do not directly fall out from the cut. Carbon fiber and kapton parts can be plasma etched in O_2, which can help improve bonding. This is an optional step that can help ensure the best bonding and prevent delamination, although it is possible for standard HAMR robots to be made without this step).

An initial 'backtack' is performed with the central carbon fiber and adhesive layers, which lightly tacks adhesive islands from the paper backing onto the carbon fiber with a few minutes of high heat and pressure (an approximately 5 minute ramp from 25°C to 180°C with approx. 150lbs pressing the 22 cm^2 layup area), before peeling away the backing and laying up the full layup. This backtack allows for unattached independent islands of adhesive to be used in designs rather than requiring a full adhesive layer. A cutout view of the different layers can be seen on the right of Fig 3.4.1, where the order of alternating carbon fiber, kapton and adhesive layers (with back-tacked carbon fiber in the middle) can be seen. All layers of the design include pin holes which allow for alignment in precision fixturing, and alignment cross fiducial markers which allow for end release.

The full layer layup is then cured under heat and pressure for several hours (using layers of steel shim, silicone, and teflon/kapton to both distributed heat and pressure evenly as well as keep parts from sticking), after which it can be realigned on the laser system and release cut out with excess pieces removed. The swing and lift linkages must be popped up on both of the chassis pieces: requiring 90 degree positioning and CA gluing into place, aided by lightly evaporated accelerant held nearby to help speed the setting process. Each linkage has two folds - the first positioning the entire linkage perpendicular to the flat chassis plane, and the second fold again folding the outer distal part of the linkage down perpendicular to the rest of the linkage base. Care is taken to avoid getting glue into active flexure areas near the base of the linkage that are needed for functioning of the transmission. This two step pop-up process is repeated for all four swing and four lift transmissions needed for the quadrupedal

robot. A closeup of these popped up linkages can be seen in the closeup of Fig. 3.6.

2. **Actuators**: The actuators are made with a pre-stack alumina-based method, as described briefly earlier. All materials for a pre-stack (PZT, alumina, FR4 jigs, Gelpak) are cut out in large batches, then used to layup one side of a pre-stack with a flush alumina-PZT-alumina layer by using an FR4 jig on top of Gelpak for alignment and to keep everything in place, as shown in Fig 3.4.3. A central carbon fiber layer is cut for the center of the actuator layup, and layered between two of these PZT pre-stacks. Throughout this process it is important to keep the charge orientations in mind, with + and - sides of PZT layers stacking in alternating layers. The same alignment holes, layup materials, and fixturing are used as before (with additional pacopad and FEP), enabling a first cure of the carbon fiber and prestack layers. The second cure adds a layer of carbon fiber and copper to both sides, which can be rastered away for traces (and potentially via holes), before the actuators can be realigned, release cut, cleaned, glued, and tested. Actuators make use of the improvements outlined above for ease of fabrication.

3. **Circuit board**: The circuit board starts as a copper clad FR4 sheet which is covered in several layers of photoresist applied using a spin coater. The same high-precision laser is used to raster away and remove photoresist from all regions not desired as circuit traces. The piece can then be etched in ferric chloride to remove copper from all areas not covered in photoresist, yielding the desired trace pattern. The boards are cleaned off in acetone to remove the photoresist covering the traces, and tinned with solder to enhance soldering. Circuit boards can be glued into an initial FR4 jig to help with actuator assembly. Completed and fully tested actuators are individually inserted starting from the middle of the board and moving outwards (each actuator that is soldered increases the stiffness of the otherwise compliant circuit boards, thus it is easier to move outwards). Each actuator is soldered loosely just to one side to keep them in place, with slight copper scraping and flux application to each trace prior to soldering for better adhesion, as shown in Fig 3.4.5.

4. **Assembly, Tethering, Testing**: For final assembly the two chassis halves and assembled circuit board actuator core can be CA glued together, with the circuit board slotting into alignment holes in the chassis pieces. The actuators are fully soldered

in place, with very slight trimming and adjustments to their positioning to ensure they align well with the carbon fiber linkages that mate with the actuator tips. Each actuator is soldered to signal, bias, and ground signals. CA glue is used to connect actuators to their corresponding (swing or lift) linkage. The spherical five-bar transmission can be popped up as seen in Fig 3.4.6 with glue added to the two corners to keep it perpendicular.

A tether is made by unravelling just the two ends of AWG litz wire. This litz wire (10/48) is a woven bundle of individually insulated 48 AWG wires (.00124" or roughly 30 μm nominal copper diameter), which can be individually scraped at the end and soldered to pins on one side, and the circuit board at the other. After testing to ensure all electrical connections are working, legs can be added to the robot and full leg deflections can be observed to determine if any linkages may need tweaking for consistent performance, ultimately completing a full robot build.

The same general procedure can be used for both a 'standard' sized HAMR-VI (4cm) and a half sized HAMR-JR (2cm); we consider it a benefit of the technique that the same designs and base process can be applied to the creation of a scaled version of the robot. However, we also note that many of the steps can be just slightly more difficult processes with the smaller variant of the task. For example, de-chipping during layer cuts can require additional attention to ensure that every tiny piece is removed as desired, as smaller pieces are less likely to cleanly fall out on removal from Gelpak. Backtacking steps can require more careful and deliberate peeling to avoid losing precision features (with a smaller area for individual adhesive glue islands, additional pressure/heat may also help to ensure proper tacking). Alignment of layups is also important, with slightly misaligned adhesive potentially either missing pieces they need to attach, or blocking flexures leading to potential stiffness changes. Traces on the circuit board are thinner and thus more sensitive to potential over-etching, with additional or thicker layers of photoresist helping to ensure success. Thin traces are also more prone to breaking or cracking that requires soldering fixing or separate wire jumpers to reconnect. Assembly of linkages at exact 90 degree angles can also be more difficult to achieve manually with the smaller version - although because of the smaller feature sizes, they can somewhat reasonably be at least partially assembled directly on flat Gelpak for fixturing (with a tiny bit of material digging in to the Gelpak), rather than fixtured in the air with reverse action tweezers as required for large

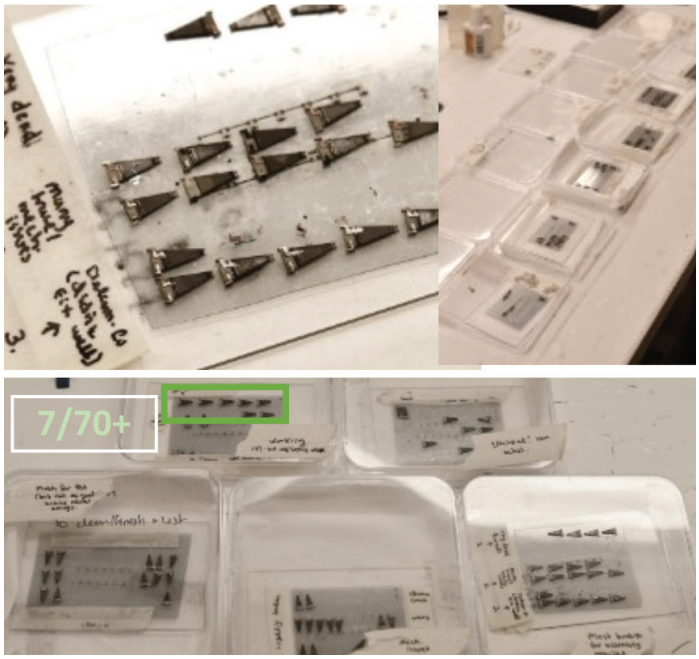


Figure 3.5: Yield of actuators for HAMR-JR. Initial attempts to make small actuators yielded few working actuators (yield $< 10\%$), but after implementation of improved processes outlined prior was able to be improved to yield full batches.

robots. Adequately gluing features in place while ensuring it avoids active flexure areas that need to remain flexible can be a challenge with tiny working spaces. Precision soldering is further required, with a steady hand, operator precision, and fine tip soldering irons for careful soldering of the signal, bias, and ground of every actuator.

Many of the actuator challenges outlined previously regarding delamination and shorting can be more prevalent given smaller areas for adhesion and closer design features for laser cuts that can cause problems to arise. In initial attempts to fabricate smaller batches of actuators prior to implementation of the improvements outlined in section 3.2.3, many of the actuators failed due to delamination and shorting challenges, as shown in Fig. 3.5, yielding roughly less than a 10% yield of actuators.

However, with the general process improvements outlined in section 3.2.3 which improve the overall methods used, we could achieve 90-100% yield of actuators (the potential for human error in breaking or inadequately gluing an actuator along the way remains, but entire batches could reasonably be completed and working at one time. Thus while using the same baseline procedures as used for larger versions of the HAMR, we are able to achieve fabrication at this scale by careful implementation of the improvements outlined above.

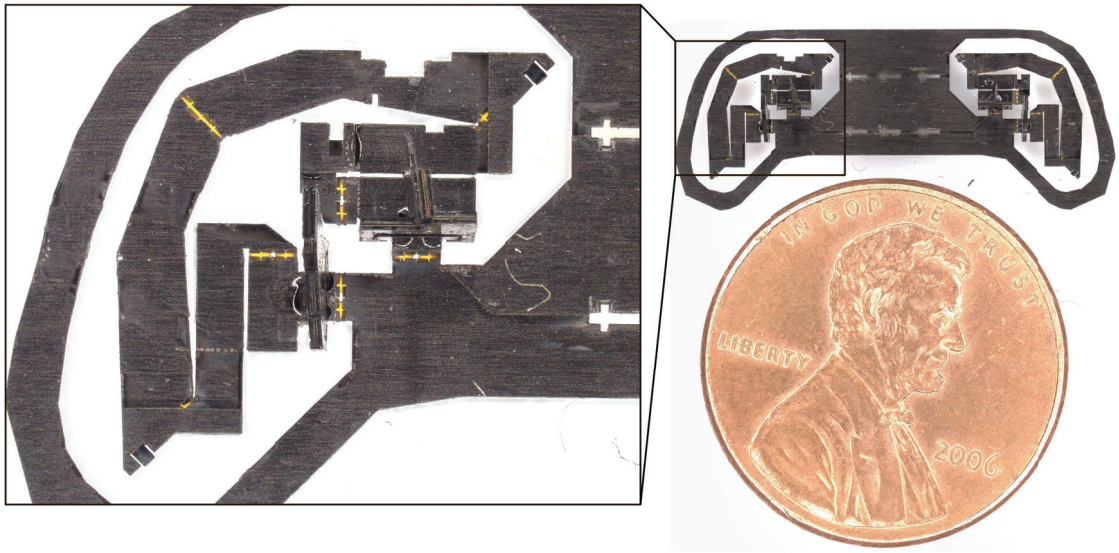


Figure 3.6: Hamr-JR Closeup View: As we can see from this high resolution image (Keyence VHX-7000 imaging system), the flexure and linkage features on the chassis (next to a penny, for scale) are very fine, and require a microscope for popup and assembly of linkages. The far left linkage (swing) and right linkage (lift) are the components sticking up perpendicular from the plane of the image; the lift linkage appears ever so slightly non-90 degrees in this photo, and may benefit from slight tweaking (by melting of the CA glue and repositioning of the linkage) for adequate mating to actuators and transmission of forces.

Such best practices can be applicable to both larger and smaller size robots to improve robot fabrication processes overall.

3.3.2 HAMR-JR Performance

After all of the fabrication steps outlined above, we examine the theoretical characteristics of the scaled robot as well as its performance. We can consider the geometric properties of the robot, where the length (l) and width (w) are reduced by half:

$$\begin{aligned} l_{jr} &= \frac{l_{vi}}{2} \\ w_{jr} &= \frac{w_{vi}}{2} \\ BL \propto l \implies BL_{jr} &= \frac{BL_{vi}}{2} \\ m \propto lw \implies m_{jr} &= \frac{m_{vi}}{4}, \end{aligned} \tag{3.1}$$

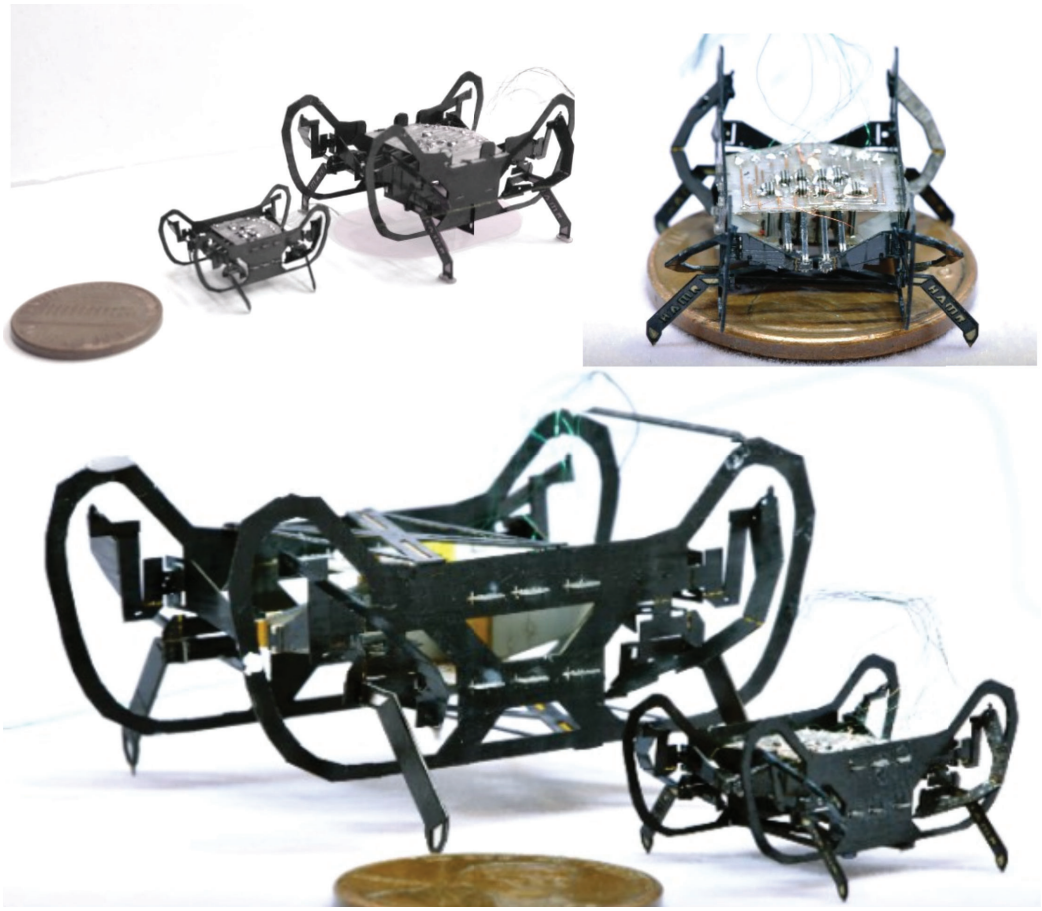


Figure 3.7: HAMR-Jr, a 22.5 mm, 320 mg robot, is fabricated using our described laminate techniques, with U.S. penny and original (45 mm) HAMR-VI for scale comparison.

where BL is the body length of the robot, m is the body mass, and subscripts jr and vi indicate the scaled (HAMR-Jr) and original-sized (HAMR-VI 45.1 mm, 1.41 g) robot prototypes, respectively. With the half-sized allometric scaling completed, we thus expect a robot with half the body length and a quarter of the mass of the original HAMR-VI robot. Indeed we find that the new HAMR-JR robot comes in at 22.5 mm (0.5 times the original BL) and 0.32 g (0.23 times the original mass).

Similarly, from prior work [47], we expect actuator mechanical characteristics:

$$\begin{aligned} d \propto l_{act}^2 &\implies d_{jr} = \frac{d_{vi}}{4} \\ F \propto \frac{w_{act}}{l_{act}} &\implies F_{jr} = F_{vi} \\ k^{act} \propto \frac{w}{l^3} &\implies k_{jr}^{act} = 4k_{vi}^{act} \end{aligned} \tag{3.2}$$

where d is the actuator tip deflection, F is the blocked force, and k is the actuator stiffness. Further detailed analysis on flexure stiffness k_{flex}, resonance frequency (ω), stride length (equal to actuator tip deflection, given the same transmission ratios in both original and scaled versions of the robot), and mean running speed ($v \propto d\omega$) can be found in [42]. This analysis anticipated roughly similar absolute velocity (in mm/s).

We demonstrate running speeds of 313 mm/s, which, when adjusted to bodylength was 13.9 BL/s, the fastest normalized speed recorded for the HAMR family of designs. It is also generally fast considering robots at comparable scales, as shown when compared against other robots. A brief recap of the new HAMR-JR compared to similarly sized insect-scale robots in terms of body length, stride frequency, speed, and cost of transport [1] can be found in Table 3.1. A version of the robot fabricated with a flexure layer twice as thick as the current version (50 μm kapton) is able to demonstrate the capability to carry a 3.5 g payload, over 10 times the weight of the robot.

Table 3.1: Locomotion performance of HAMR-Jr against other insect-scale robots [48].

Robot	**Body length** (mm)	**Stride frequency** (Hz)	**Speed** (BLs^{-1})	**Cost of Transport**[1]
Wu (2019) [21]	10	850	20	14
St. Pierre (2018) [49]	2.5	150	14.9	33.1
HAMR-Jr	22.5	200	13.9	33.8
HAMR-VI [10]	45.1	65	10.6	7.4
Shin (2012) [50]	20	55-75	2.4	743
Kim (2019) [6]	2	63000	4	-
Contreras (2018) [51]	13	100	0.07	39.8
Tribot (2019) [52]	58	-	-	4.4

[1]Note - we consider the Cost of Transport [53] to be a dimensionless quantity, defined by $CoT = \frac{P}{mgv}$ [11] where P is electrical power input, m is mass, g is gravity, and v is velocity.

3.3.3 Future scaling

Future efforts into further scaling the robot to even smaller size scales (e.g., to 1 cm scale or lower) will need to consider the challenges of assembly precision in such fine detail systems. While previous work has been done to scale actuators down to roughly 2 mm [47], the assembly and construction of the overall robot would remain non-trivial. A brief consideration of potential robot changes can be seen in Fig. 3.8, wherein alternative options of assembly design (reducing the number of actuators by pairing some leg swings, modifying the thickness of actuators, changing the assembly interfaces, and improving the assembly methods) could make such tiny robots easier to assemble. Options which allow for actuators to be dropped in all at once rather than soldered in one by one (either through circuit board interfacing or via exploration of multilayer actuator blocks) could be useful for ease of assembly. Future work could also consider implementation of alternative actuator designs using only carbon fiber for structural components [54] as an option for non-alumina based actuators which could be made thinner or with reduced potential for breaking during insertion. In addition, monolithic or popup designs adaptations [40, 20] could be incorporated for easier assembly which avoids many of the careful hand assembly pop-up tasks (albeit with potentially more upfront work for changes and edits to design). We also consider that hard equipment limitations come into play at these even smaller scales, for example with laser resolutions limits for both features and re-alignment that may need to be considered at smaller scales.

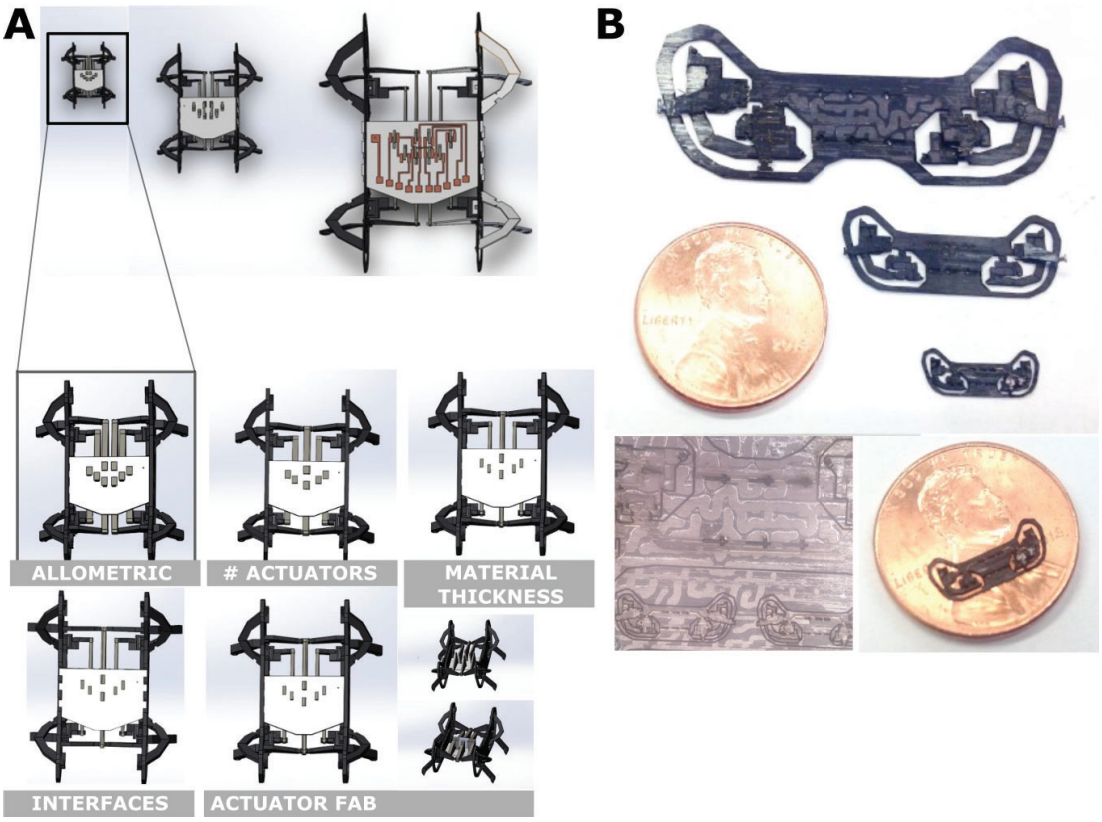


Figure 3.8: Potential considerations for future scaling. Left: By considering alternatives to a direct allometric scaling of the same design, including fewer actuators, thinner materials, circuit board revised interfaces, and actuator core fabrication methods, we envision easier assembly can be possible for small scales. Right: a brief proof-of-concept of a further scaled 1 mm chassis vesion of the robot, albeit with challenging popup of linkages and cut alignment.

3.4 HAMR Fabrication and HAMR-JR Summary

In this chapter we outline the basic HAMR fabrication procedure, with careful attention to the practical nuances and intricacies of actuator fabrication. We note some of the common failure points and challenges in the fabrication of these devices, as well as outline some of the solutions implemented (or suggested for future consideration) that can improve ease of fabrication. With these troubleshooting efforts and overall improvements to the fabrication process, we are able to (1) make these tiny microrobots more reliably and efficiently, as well as (2) demonstrate scaling these fabrication processes to a smaller size scale, with development of a 2 cm HAMR JR, one of the smallest and fastest normalized running speed versions of the robot.

These improvements to the robot are useful in several ways. Firstly, these overall process improvements can make creating these robots easier. While many of these changes may individually be incremental and small, a single failure can ruin a full set of actuators, ultimately causing a researcher to restart from wherever they are in the multi-day process. By streamlining these processes and striving to update documentation and communication, we can achieve several benefits: increased speed of training for other researchers, faster production of robots within the lab (for many of the leg appendage-based experiments which require base robots to explore questions), and construction of the scaled-down robot as shown here.

The additional speed of completion can be compounded with both actuator and general fabrication improvements in tandem with a scaled robot design: a 'regular' HAMR-VI would require fabricating two separate batches of seven actuators to complete a full robot, potentially taking twice as long. This is in part due to the limitations of the laser field of view and room for actuator layout preventing a full set of eight from being made at one time. However, it is also in part due to overall yield, which while never previously formally quantified, did not necessarily anticipate a full yield. With process improvements as described plus the scaling of HAMR-JR actuators, we can fabricate 13 actuators in one batch (plenty for a single robot, with room for extras in case of performance variation), and can reasonably anticipate being able to have a full batch of functioning actuators at the end. While exact actuator performance may still vary slightly among a batch, having extras can allow for pairing or matching of actuators if needed, and yield enough to choose the best actuators for a robot.

Given the additional assembly challenges for a small scaled robot (and smaller features in general), it is not necessarily faster to make the half-scaled version of the robot despite actuator batch size increases, thus we elect to still use the 4 cm size robot platform for experimental studies and tests. We can take advantage of the streamlined processes to still achieve actuator consistency and reliable batch fabrication and yield at slightly larger scales, with the option always existing to scale down smaller for application use cases after studying appendages, leg attachments, and phenomena at larger scales.

Improving these processes overall can also serve as a useful step towards eventual commercialization or industry usage of these currently research-based systems. In collaboration with collaborators at Draper Labs, the fabrication process was able to be communicated and moved from the lab environment to successful fabrication in an industry research setting [1], paving the way for such development efforts to extend beyond the limits of academia. As a small aside, we note that this platform also lends itself well to potential STEM and outreach activities, and can further be found published for younger audiences [2].

As mesoscale robots seek to continue scaling both up in quantity or down in size, further efforts will need to continue to examine both the process techniques and limitations of existing methods for complex small designs. However, for now this process enables us to build these robotic systems more reliably and we next turn our attention to tackling questions of foot adhesion and locomotion using this base robotic platform.

[1] https://www.draper.com/media-center/news-releases/detail/23416/tiny-self-guided-robots-to-the-rescue-in-high-risk-environments

[2] Feature article of the Oct 2023 issue of *Highlights Magazine* for children.

4

Electroadhesive Pad Improvements and Robot Characterization on Pristine Surfaces

4.1 Electroadhesion Characterization and Payload Motivations

With a robotic platform that can be used for microrobotic locomotion, we next consider potential improvements to the adhesive mechanisms themselves required towards the goal of locomotion on inclined surfaces. As these robots seek to someday be used in inspection tasks in the real world, not all surfaces are expected to be flat, so the ability to achieve locomotion on inclined surfaces will be required. The work done by Rivaz et. al. [13] demonstrated the potential for using electroadhesion for climbing inclined surfaces and inspires the baseline approach to this work, but HAMR-E (1.48 g, 4.5 cm) is still not yet a fully functioning system that can work in real world situations. Particularly as we consider the potential for microrobots to eventually be used in groups for inspection or in-the-field exploration tasks, we note the importance of eventually being able to autonomously power and control such systems, not just run them as tethered versions. Work has also separately been done previously on an autonomous version of the robot, HAMR-F (2.79 g, 4.5 cm) by Goldberg et. al. [11] as shown in Fig. 4.1.

However, having onboard power and control electronics requires additional robot payload (in the case above, the robot has around 1.3 g added mass, even with dedicated design of lightweight electronics), almost doubling the total microrobot weight. While the

autonomous HAMR-E was able to run on flat surfaces, being able to someday incorporate such electronics onto systems which can tackle inclines and non-flat surfaces will be important. For climbing robots, added weight can be a challenge, with increased potential for a robot to fall or otherwise struggle to pull itself forward on an incline.

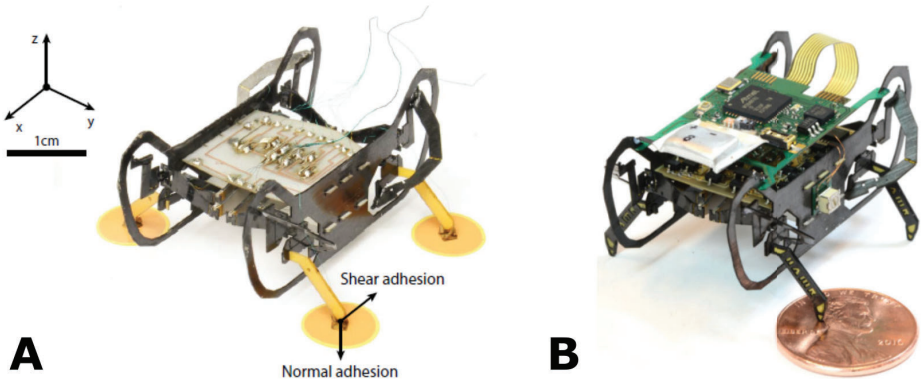


Figure 4.1: Two prior HAMR versions: A) HAMR-E [13] is capable of inclined and inverted locomotion through the use of its electroadhesive feet. However, it has not yet been implemented with considerations of payload. B) HAMR-F [11] is capable of autonomous power and control, yet weighs approximately 1.3 g more than the standard version.

Thus here we primarily explore the question: Can we fabricate and understand the performance of a robot with the mechanical and adhesive capabilities to reliably hold an additional payload during climbing? To do this, we tackle a few sub-questions:

1. How can we improve the design and fabrication of electroadhesive pads to account for potential added payload while still retaining a high factor of safety on adhesion capabilities?

2. How can we test the robot capabilities to climb with added payload, as well as consider the tradeoff of different payload massess on performance? What strategies could be employed to improve the capability of the robot to climb inclines by adjustment of payload location?

We explore these questions of electroadhesive improvement, characterization, and robot capabilities in the following sections.

4.2 Electroadhesive Pad Fabrication and Design

This work was done in partial collaboration with Rut Pena, with contributions to electroadhesive pad fabrication explorations.

4.2.1 Standard Pad Design Considerations

The design of the electroadhesive (EA) foot pads inspired by prior work [13] is based upon a parallel plate capacitor model, where the top of the foot pad receiving a commanded voltage is one side of a capacitor, the bottom pad layers (kapton), in addition to any additional air gap between surfaces, act as a dielectric in the middle, while the top of the grounded conductive terrain surface beneath the pad forms the other side, as shown in Fig 5.5A. Thus approximating the behavior of a pad in close contact with flat conductive surfaces as similar to that of a standard parallel plate capacitor (for which the area is much larger than the distance between them), the adhesion force can be approximated using the following equation [13]:

$$F_{adh} = A\epsilon_0\epsilon_d\frac{V^2}{2d^2} \tag{4.1}$$

where V is the voltage, A is the conductive area of the pad, ϵ_0 is permittivity of vacuum, ϵ_d is the relative permittivity of kapton (3.4-3.6), and d is the dielectric material thickness.

We note that this unipolar parallel plate capacitor model was explored due to its suitability for an industrial inspection setting, where a conductive or semiconductive surface can be readily grounded for robotic inspection or maintenance tasks. Such a unipolar design involves simpler fabrication and reduced risk of dielectric breakdown than the more complex bipolar interdigitated designs required for electroadhesion on non-conductive surfaces [38], but such alternative electroadhesion methods could be explored in future applications.

In theory, based upon these equations the adhesion of such pads can be increased in one of several ways: increased area, increased voltage, or decreased dielectric thickness. Each of these avenues has their own trade-offs:

- **Area** increases should scale linearly with F_{adh}, which is one of the simplest options to employ to increase adhesion. However, this method has limitations. Because these adhesion pads are used as feet, there are space constraints given the bounds of the microrobot (given a roughly 4 cm long microrobot and 1 cm size pads), as adhesive robot

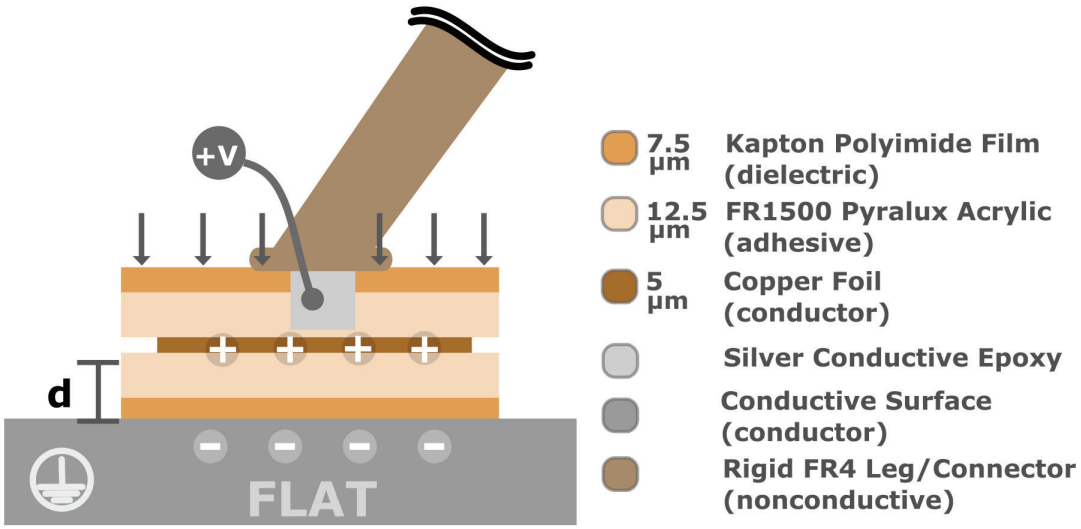


Figure 4.2: Diagram example of physical electroadhesive pad layup with parallel plate capacitor elements labelled. Voltage (V) is applied to the central copper layer via conductive epoxied connection to a thin electroadhesion tether wire, and flat surface is grounded, thus forming the two plates. The distance between of dielectric gap (d) is also shown.

feet should not step onto or intersect with each other during locomotion. Especially as these systems seek to scale further in the future (towards 2 cm total robot length or smaller, potentially carrying payloads beyond just the mass of the robot itself), we could envision that payloads (of sensors, cameras, communication and power boards, or other such useful electronics with their own scaling limits) might increase relative to the robot mass. Thus with smaller footpad working area given gait constraints, and potentially increased relative payloads to carry, purely area-based adhesion improvement strategies that don't seek to use space efficiently for adhesion density may not be sufficient. We further might anticipate that increasing the overall footpad area may increase the odds of running into surface constraints, such as surface cracks, edges, or other structural heterogeneities that change across larger scales over the surface environment.

- **Voltage** increases should scale quadratically with F_{adh}, which could in theory lead to even better performance than larger area alone. However, supplying a higher voltage may require more complex electronics and amplifiers to deliver. Particularly when thinking about eventually placing such power elements onboard a robot itself, being mindful of the tradeoff with potentially added weight is important. Moreover,

even with high voltage amplifiers, the structures themselves and materials can face dielectric breakdown at high voltages (25 μm Dupont Kapton has dielectric strength of approximately 300 kV/mm), thus this method is also limited.

- **Dielectric thickness** decreases should scale quadratically, with $F_{adh} \propto 1/d^2$ The main drawback to this method is fabrication complexity - being able to obtain and layer increasingly thinner dielectric layers can be a complex task, and off the shelf options for thinner material supplies reach a limit (off-the-shelf options of DuPont Kapton polyimide thin films reach only 5 μm, 7.5 μm and 12.5 μm). Practically speaking, this means that we are limited to only certain limited quantized layer choices. However, with efforts to explore such thinner materials selection at least within the options available, this method could still be used to help further performance beyond what the other two options of area and voltage could achieve alone. The potential of exploring how to deposit even thinner films (perhaps via sputter coating or spin coating of polyimide) instead of using existing layers also exists, but would require more dedicated fabrication exploration in the future to explore those processes. We can also consider that additional layers sandwiched within the structure of pad (such as the adhesive or copper layers) may increase the effective overall thickness and thus thinner layer options for these material layers could similarly be investigated - albeit with their own quantized layer options as well.

4.2.2 Dielectric Thickness and Fabrication Exploration

We thus begin by examining the potential to increase the performance of electroadhesive pads through a decrease of the dielectric thickness - as scaling up area (within realistic robot and surface constraints) later is relatively easy from a fabrication standpoint, as is later testing such pads with different operating voltages. We attempt to decrease the dielectric thickness in two ways: (1) use of thinner off-the-shelf dielectric materials in a laminate structure method, and (2) use of alternative fabrication techniques, such as copper sputter coating, to obtain thinner layers than copper layer laminate layups. The four different permutations of method and thicknesses fabricated and tested in our exploration can be seen in Fig 4.3, with details to follow.

The multi-layer technique for fabrication uses a similar procedure to those methods used for general robot construction described in the prior chapter, wherein layers of different

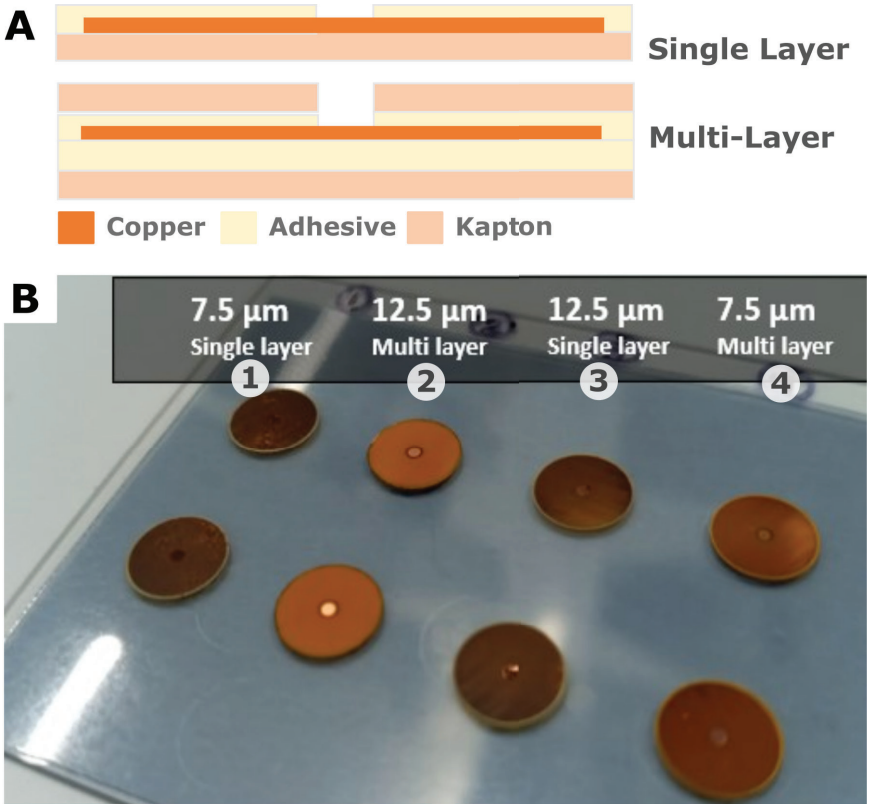


Figure 4.3: Elecetroadhesive pad types: single-layer pads were made with a sputter coating technique, while multi-layer pads were made with a layup and cure technique. Both fabrication methods explored the difference of a similarly decreased dielectric layer thickness ($12.5\mu m$ and $7.5\mu m$)

individual materials are laser cut, stacked, cured, released, and folded into the final shape. We use a similar approach to methods implemented in prior work [13], with a full view of the material layup in Fig. 4.4 and a full outline of the procedure in Fig. 4.5.

In summary, the fabrication process was as follows: layer-by-layer CAD design. Dxf files (Fig. 4.4, Right) were used to generate laser cut files. These design files include both the material layers themselves, room for release cuts around the layers, and alignment marks (four alignment pins, and three alignment cross fiducial marks along the centerline for later rotational alignment). The copper layer was carefully removed from its carrier backing and placed on a Gelpak 0 (light adhesion Gelpak) substrate, which was itself mounted onto a second layer of Gelpak 0 adhered to the top of a flat glass slide. The Gelpak on the slide helped keep materials in place without sliding during laser cuts. Both the copper and first Gelpak layers were cut with appropriately tuned settings on a DPSS (355 nm UV

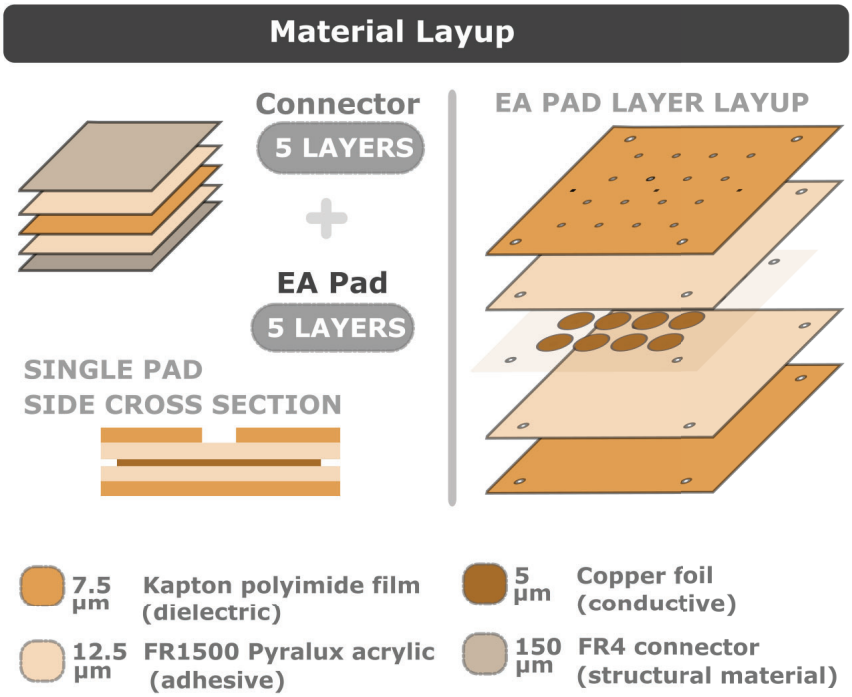


Figure 4.4: EA pad fabrication. Left: the material layup for the electroadhesive pad itself, as well as the material layers used to make a simple ring connector for attachment to the top (if desired, for fixturing) are shown. Right: Each layer is laser cut with the relevant designs prior to full lamination, enabling features (like holes for conductive epoxy or insulating borders of kapton) to be made in the layup.

wavelength high precision) laser. By using two layers of Gelpak, the top layer of Gelpak could be easily cut to size including alignment jig features and removed for use as a layer in the layup itself. This was helpful for backtacking steps, to keep all the individual islands of copper precisely in place.

Excess copper foil was removed using a pair of tweezers by pulling away unneeded copper. An alignment jig with pins in the corners was used to align the Gelpak layer with copper pad islands onto the jig. Layers of 12.5 µm FR1500 pyralux adhesive and 7.5 µm (or 12.5 µm) kapton were similarly cut on the DPSS using the same Gelpak 0, then added on top of the alignment jig layup such that a single layup of layers (Gelpak 0, copper, adhesive, and kapton) was aligned. This layup was placed under a weight stack (85-100lbs) which applied heat and pressure for 5-10 minutes - just enough to lightly tack all the elements in place but not fully cure the adhesive. The result of this initial 'backtack' partial cure is a layer with just the aligned copper pad traces attached to the adhesive and kapton.

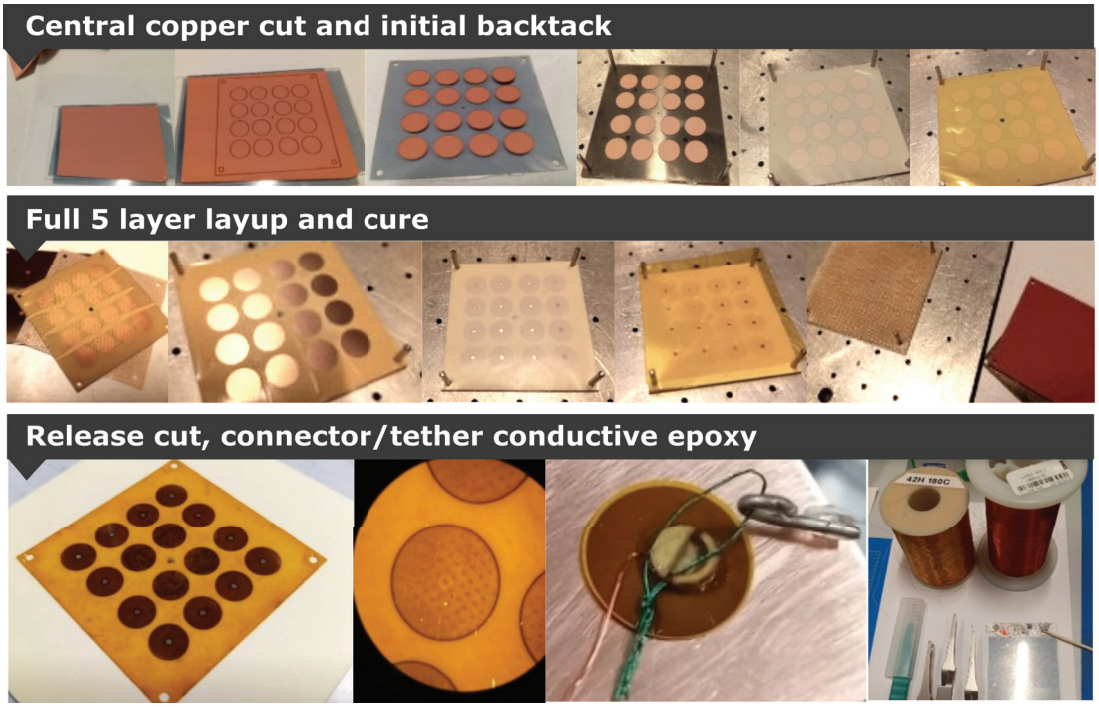


Figure 4.5: EA pad fabrication full process: This figure demonstrates the full process of making multi-layer electroadhesive pads using a laminate approach. Following initial material cuts, layers can be aligned in one layup and cured with heat and pressure into a single laminate, which is then cut and released into the final individual pads. A connector of FR4 can be made to add to the pads themselves using a similar process.

The remaining two layers of kapton and adhesive were then cut on the laser and laid up alongside the initial backtacked layers on the alignment jig. The full layup was then cured for several hours under pressure and heat according to adhesive requirements, and removed when completed. This step could also be done using the same weight stacks for multiple sets of layer layups at one time - provided that the pressure and heat be evenly distributed for each layer.

The final layup was then remounted onto a Gelpak 0 on a glass slide and aligned to account for rotational offset using the alignment crosses. Thermal drift between the laser system and camera was also accounted for using a calibration test cross. Release cuts were performed to release the final part. The final released individual pad designs were all then individually conductive epoxied (EG8050 silver-filled two component epoxy, cured for at least 12 hrs in an oven at 65°C) using a thin 38 awg wire attached to breakout pin for easy testing, with an FR4 connector hook added on top of the conductive epoxy and taped

down with high temperature resistant masking tape. This connector piece helped provide a uniform flat way of attaching the positive voltage wire without worry of it coming out or causing the pad to curl during epoxy curing. The connector itself allows for either in-plane shear loading, or folding up 90 degrees for vertical normal loading. A small compliant insulated piece of tether wire string was looped and tied through the connector piece, and used for adding weights or attaching to more dedicated loading systems. A final completed pad is shown.

Slightly thinner 7.5 µm kapton is shown to scale in Fig 4.4, which should in theory provide slightly stronger adhesion than the 12.5 µm option used in prior work [13] due to the thinner layer. In using thinner materials, wrinkling and static of the material did make fabricating slightly more challenging. Additional attention was given to removing air bubbles and wrinkles from between the Gelpak and material (using careful placement laying the material down on Gelpak, with rollers and glass slides to squeeze out any remaining air) in order to ensure the most accurate laser cuts, but the process was otherwise similar.

In comparison to the above methods, the single-layer technique for fabrication used a sputter coating method for achieving layered layup of the copper design rather than a layer-based lamination approach, and can be seen in Fig. 4.6. In this process, a Gelpak mask with holes for the copper circles is made to cover a kapton base layer. The kapton and Gelpak is placed in a sputter coated and covered in a thin copper layer (roughly 0.2 μm). The mask can then be removed and an adhesive layer added to the top for insulation before the entire layup is release cut into individual footpads and wired together simiarly to the prior method. This process was also tested with the same two different thicknesses of kapton.

4.2.3 Comparison of Electroadhesive Pad Design Performance

A comparison of the shear adhesion performance of four different types of electroadhesive pads tested can be found in Fig. 4.7A. The results of the single process and multi-layer process can also be seen separated out in Fig. 4.7B, for easier viewing. Each pad was attached to a small lightweight paper loading boat (roughly 100 mg) similar to the one shown in Fig 4.7C, adhered to a surface in the vertical shear direction, and manually loaded carefully and gently with small uniform light (roughly 100 mg) weights until it slipped. The shear direction of loading was chosen for testing, as this was anticipated to be the

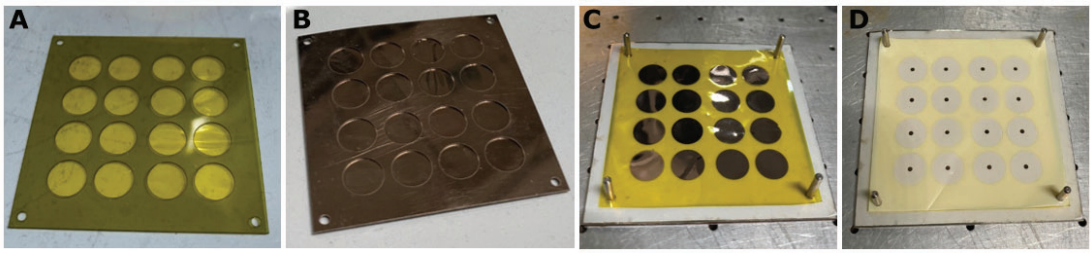


Figure 4.6: EA pad fabrication single-layer sputter method: A) The base kapton with a mask of gelpack on top with holes. B) The entire surface is sputter coated with a thin layer of copper. C) The Gelpak mask is removed, leaving only thin copper in its place. D) An adhesive mask is added on top, and the entire laminate is cured with heat and pressure prior to release cuts for individual pads.

most relevant direction of testing for a robot climbing potentially steep inclines. This also avoided the difficulty of having to avoid peeling effects that may occur with normal force measurements. A range of voltages were tested, 300V, 500V, and 700V, to also examine the impact of voltage. Each pad and voltage point included at least five trials. All tests were conducted on a flat copper substrate sanded with P2500 grit sandpaper for a flat, smooth, pristine clean mirror-like surface.

From these tests, it appeared that despite the thinner and more compliant design of the single-layer pads, the multi-layer pads generally displayed better performance. This is somewhat counter to prior hypotheses, which would generally anticipate that decreasing the dielectric thickness and increasing the potential compliance of the pad overall would result in better performance. Several factors could potentially have contributed to this result. These very thin pads could be prone to curl slightly prior to engagement, as a result of even very gentle handling, lifting from the Gelpak, and final assembly steps. Since adequate contact is important to adhesion performance, having pads as flat as possible when adhering against a flat substrate would make a difference for performance. It is also possible that the very thin layer sputtering methods resulted in a less than ideal conductive layer compared to the solid copper sheet used in the laminate layered process. Future work could explore this method of in depth tuning the sputtering processes. Nevertheless, the results seem to indicate that for a multi-layer laminate structure where things are kept flat, a thinner dielectric does indeed result in better performance, as would be anticipated.

Thus it appears that pad type 4 (a 7.5 μm dielectric thickness, multi-layer method fabricated electroadhesion pad) appears to perform the best, with 60 $\pm$25 g when run at

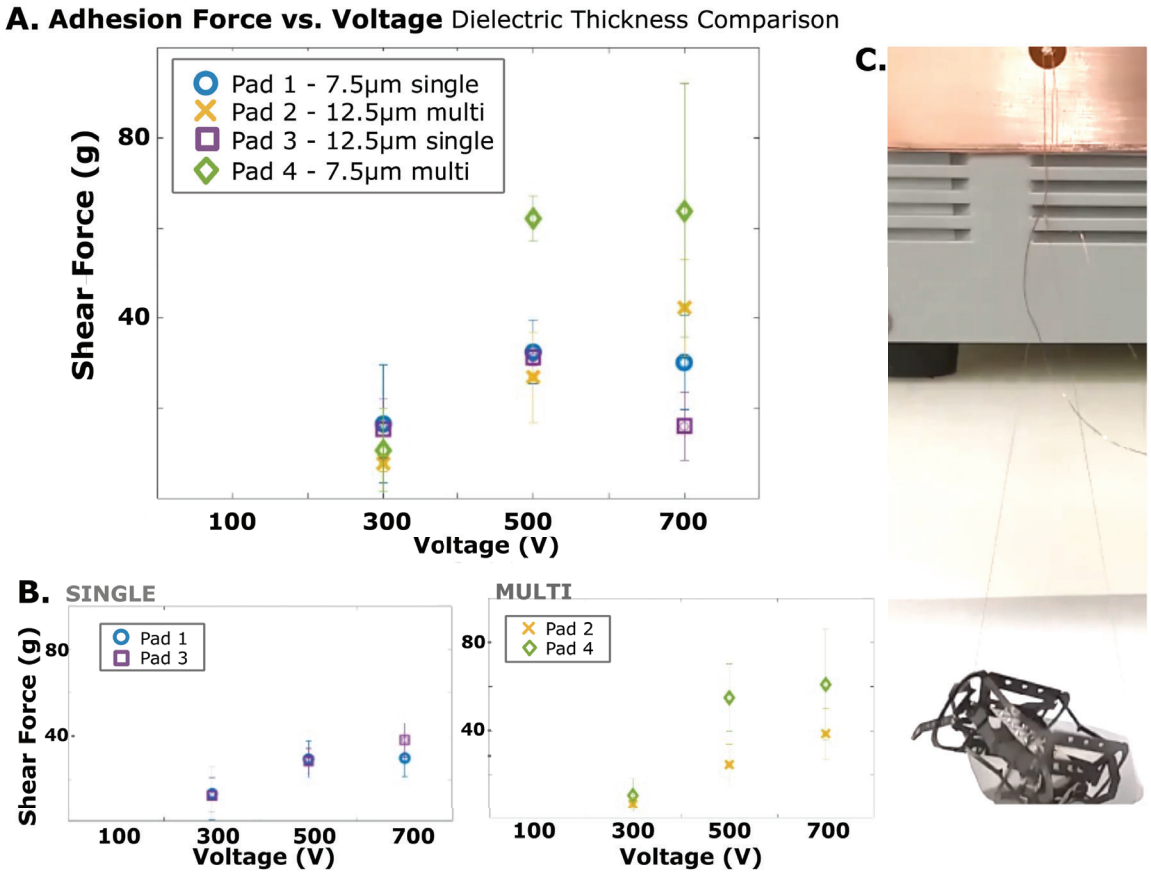


Figure 4.7: EA pad performance comparison. A) Adhesion shear force (in grams) vs. voltage (300 V, 500 V, 700 V) for the four types of pads fabricated. B) The same data as (A) sorted into results of the single and multi-layer fabrication methods. While pads do not reach the theoretical adhesion forces of Eq. 4.1 (anticipated given imperfections of real world fabrication and environmental interactions), this experimental comparison provides a reasonable comparison between different pad types to indicate which ones comparatively perform better. Pad performance is relatively similar at lower voltages (300 V) but pad 4 (thinner kapton dielectric layer and multi-layered fabrication) appears to perform better both compared to single-layered fabrication and thicker kapton options. C) A demonstration of pad 4, with a small paper boat filled with weights (including a full HAMR robot).

700 V (11 ± 8 g at 300V, and 55 ± 15 g at 500V). This provides a rough theoretical factor of safety of approximately 65× at 700V or 12× at 300V given the average performance. This is calculated considering a climbing robot to keep three feet on the ground at any given point during a tripod climbing gait for a 2.8g robot, thus 0.93 g required per footpad. There was a fairly large amount of deviation in the measurements; even when considering the lower end of the standard deviation however, with 700V we could still anticipate roughly a 38× factor of safety. We demonstrate the capabilities of a pad 4 by loading a small boat with individual weights, before additionally adding an entire HAMR robot on top, all supported by just the single pad as shown in Fig 4.7C.

These results seem promising and lead us to believe that for such pristine flat terrains, the design and fabrication of pad 4 is more than sufficient for adequate adhesion even with large payloads added to the robot. While we focus on the adhesion capabilities themselves in this study and do not implement a fully onboard power robot system in this work, these results could also be used in future efforts to help guide design considerations surrounding the tradeoffs of voltage capabilities and adhesion. For example, if electronics that can support a higher (700 V) voltages are developed but come with additional payload costs, these results could be used for reference to determine whether implementation may make sense, considering potential other loads (batteries, sensors, etc.) that may also be added.

With a broad understanding of adhesion performance for these flat surfaces, the capabilities of the robot itself in adapting to payloads can next be investigated.

4.3 Robot-level considerations of climbing payload

4.3.1 Robot Pull-Up Tests

Beyond adhesion, understanding and testing the ability for a full robot to pull itself forward during a step is also a required component to climbing ability. A simple 'pull-up' test procedure was implemented to determine an approximate understanding for whether a robot with a given set of actuators and transmission design could achieve reasonable forward movement within a single step when on an incline. For this test, an robot is initially turned on with no commanded motions (allowing actuators and legs to reach their initial resting configuration) and adhered to a surface. The four swing actuators are then commanded

with a simple "pull-up" gait (0.2hz, 200V in phase swing sine wave) to test how far the robot moves itself in one cycle, as shown in Fig 4.8A. The forward distance moved from this resting starting point, as well as backwards distance (and resulting calculated total distance) is tracked with ImageJ analysis of video capture. The robot was tested at angles ranging from a span from horizontal to nearly vertical (0, 10, 30, 45, 60, 80 degrees), as shown in Fig. 4.8B. Additionally, 3D printed proxy payloads were printed (Fig. 4.8D), which allowed for mock massess of 1 g and 2 g to be added to the robot for comparison testing.

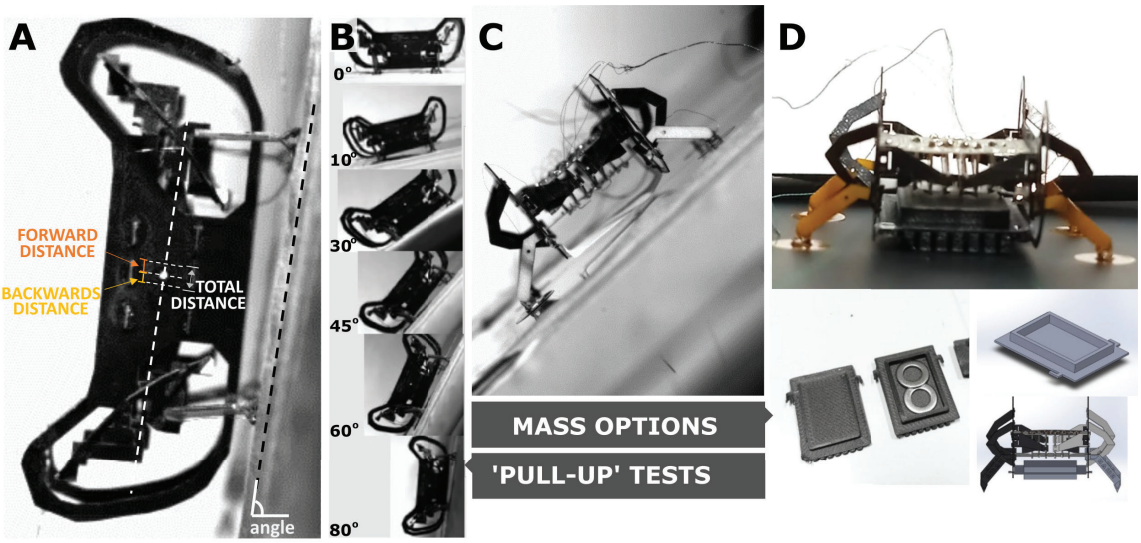


Figure 4.8: Robot Pull-Up tests were conducted to assess actuator pulling capabilities. A) Test setup and distances measured. B) Angles of incline tested. C) Front view of robot and a simple lightweight test payload. D) Robot with 3D printed payload mounted beneath the robot chassis and actuators.

In this test, only the robot design itself is tested with adhesion assumed constant - to simplify control, the robot is stuck to a sheet of Gelpak which holds the robot in place at different inclines. This simplification was made for purposes of independently assessing only the robot actuation components, and further pursued in light of the strong performance of pad designs in the prior section.

While the results of this test could be compared against pure actuator blocked force and deflection capabilities that have been explored in the past (for example, suggesting that for a HAMR-VI robot, each swing transmission should be able to yield approximately maximum one-way deflection of 2.5 ± 0.3 mm and force 13 ± 1.6 mN [10], or 1.3 g),

this method provides a characterization and understanding of how a full robot (with any additional robot level twisting or inefficiencies) may behave, along with an approximate understanding for how distances may change with varying payloads.

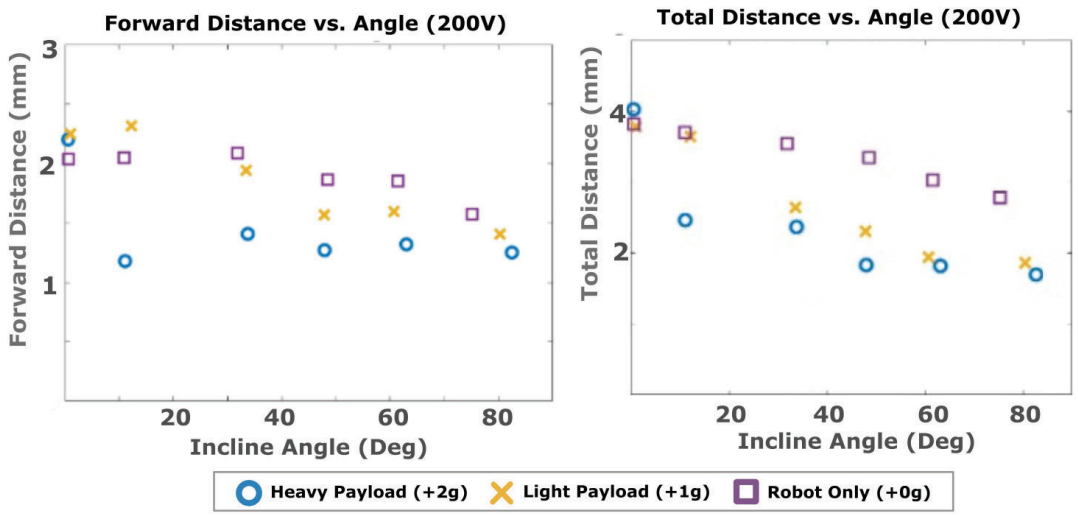


Figure 4.9: Pull-up test results: Left) The forward distance vs. inclined angle for the robot with 3 payloads added to a base 1.5g robot. Right) The total distance (forward and backwards distance) aross the same angles and payloads. Incline angles were manually adjusted, with exact incline angles measured during analysis of data, hence some slight variation). One trial per data point.

The results of this pull-up testing can be seen in Fig. 4.9. As generally anticipated, the distance a robot can move generally decreases both with increasing angle of incline and increasing payload. At low 0 to 10 degree inclines, it appears that a payload added to the robot can increase the distance the robot is able to move in a single pull-up cycle, perhaps due to momentum. All four legs were used in this experiment as a measure of total robot capability, but only three legs are used in tripod gaits (from prior works [13]). Brief experiments with variants of this trial were also conducted to gain an understanding of potential anticipated variability, for example with a robot using only three legs to swing forward, as seen in Fig. 4.10B. If all four swings were in fact needed, alternative variants of gait which pull collectively and then step could be explored. As shown also in Fig 4.10A. the results for a single robot with this pull-up test were relatively consistent, with slightly more variability with heavier payloads. However, from robot to robot there was more variation – this could be due to manufacturing differences, as well in part due to age/usage, since flexures may lose stiffness with repeated use.

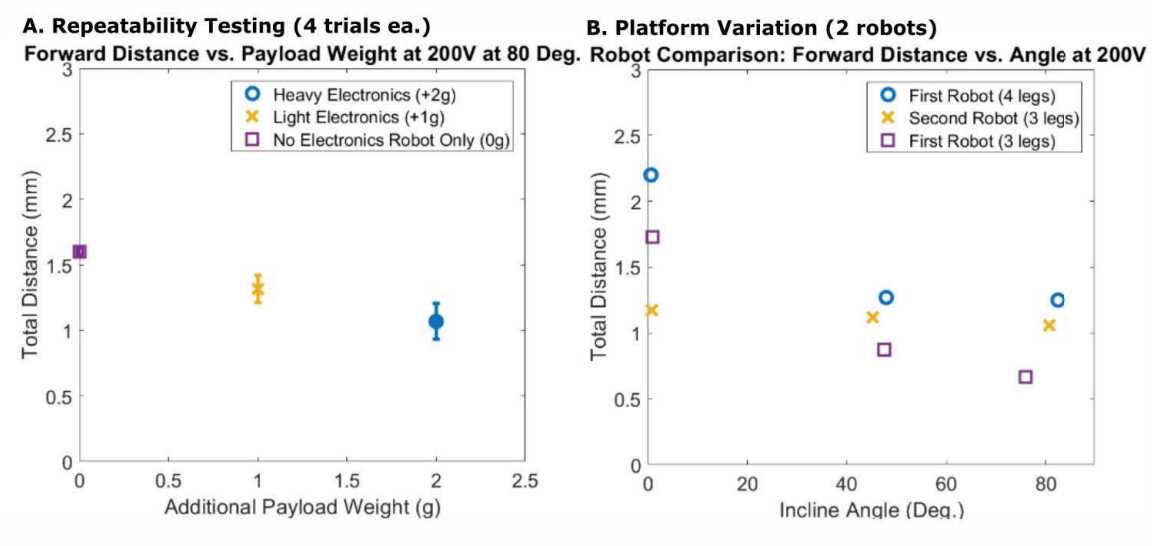


Figure 4.10: Pull-up test variation: A) Pull-up Tests at 80 degrees repeated with four trials per data point for understanding of variability. B) Pull-up tests with different robots and different number of legs used. One trial per data point. While data variability appears relatively low within a given payload/angle/robot configuration, changing the robot and number of legs used makes a greater difference.

From these results, we can see that for the payloads tested, the robot should be able to make some amount of forward motion in all cases of payload and incline angle, with (for example) robot 1 at 80 degree inclines resulting in single pull-up rep distances of around 1.6 mm (only 1.5g robot), 1.3 mm (with +1 g payload), 1.1 mm (+2 g payload).

Thus we find that the robot should reasonably have the capability to pull itself forward during climbing for the ranges of angles (0-80 degree) and added payloads (1-2 g) explored here. Actual robot locomotion capabilities which may need to consider not just whether the robot itself can inch forward slightly or adhere alone, but how well individual legs reach forward for the next step, successfully adhere, and disengage at the beginning of the next step, which may be more challenging than single pull-up testing.

4.3.2 Robot 'Toppling' Exploration

This exploration was completed in collaboration with Arjun Batra, who contributed to model analysis of angle and adhesion forces.

We also briefly consider a biologically-inspired approach to center of mass distribution that may enable us to design a better robot for use with climbing payloads. Climbing

on inclined surfaces is an essential capability for insects to traverse and explore varied locations and lends insight for small bio-inspired robotic devices looking to reach similarly diverse sets of environments. Such locomotion presents a few challenges: how does an insect avoid tipping over when climbing? And if a robot attempting similar locomotion patterns requires additional payload (due to power and controls electronics, sensors, or other loads) where could it be optimally placed to avoid compounding the toppling challenge? With these considerations in mind, exploration was conducted on how the center of mass distribution of a climbing robot influences the tipping angle limits of a purely geometric balance, and what adhesion forces may be required to achieve climbing at higher angles.

We draw inspiration from work done by Whorl et. al.[55] on the use of two kinds of ants: Formica ants, which use adhesion-based strategies, and Cataglyphis ants which use geometric properties, both to avoid toppling. We consider a simplified approach to understanding the anticipated angle of tip θ given a particular center of mass geometry. From a consideration of geometry and the torques resulting from gravity, we find $tan(\theta) \leq \frac{w}{h}$, where w is the width from the center of mass to the leg and h is the height from the ground to the center of mass. We can also calculate an anticipated theoretical force of adhesion needed to balance torques for a more active approach (see Appendix A for calculations). We attempt a very brief proof-of-concept experiment to illustrate the effects of the geometric approach (an altered center of mass), as shown in Fig. 4.11.

We simplify with a basic scenario in which we consider a HAMR robot has adequate adhesion on the two back legs, but does not have any adhesion on the front legs. This scenario can be reasonably expected over the course of electroadhesion-based climbing - perhaps the robot did not make close adhesion contact on its most recent step with one front leg, and has just disengaged its other front leg to take a next step forward. For simplicity of testing and to isolate the center of mass variable of interest, rather than use electroadhesion we assume a strong sufficient adhesion force can be represented through use of a sticky Gelpak as in our prior robot pull-up tests.

Simply by changing the location of an additional 2 g payload from the top of the robot to the bottom, we improve the static tipping angle from 25 to 45 degrees. Thus we see evidence that geometric considerations can improve the angles at which a robot can climb with enhanced reliability from the purely geometric center of mass approach, and the potential to rely on adhesion to reach higher inclines.

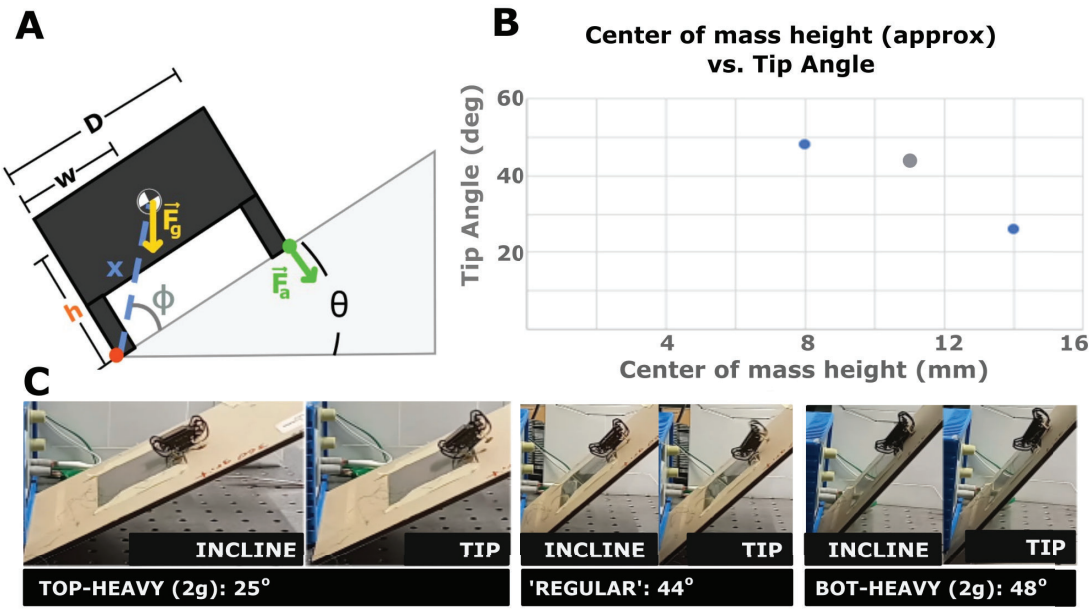


Figure 4.11: Toppling experiments given geometric center of mass position: A) Shows a brief model of the robot, where the red dot denotes tipping axis (at robot hind legs). The center of mass height (h) from ground and width (w) from the leg, surface incline (θ), distance from tipping point to center of mass (x), and forces of gravity (F_g) and adhesion (F_a) are shown. B) Shows a brief experimental test where the approximated center of mass of a standard robot (1.5 g) is shifted up 3 mm with the addition of a 2 g payload to the top of the robot or down 3 mm with the addition of a 2 g payload to the bottom of the robot. C) Several frames from testing, where the moment of robot tipping is shown.

4.4 Pristine Terrain Electroadhesion Summary

In this section, we explored electroadhesive design and fabrication considerations in tandem with testing robotic platform capabilities relevant to achieving locomotion with added payloads on inclined pristine smooth terrains. By investigating variations of the fabrication process, we solidify a manufacturing process with decreased dielectric thickness to improve adhesion. There was a relatively large amount of variability in the results - electroadhesive experimentation can be challenging because of many factors (electroadhesive static charge buildup, environmental factors, as well as the weighted boat resolution and loading technique), and we strive to improve these methods in following chapters. Nevertheless, we demonstrate increased adhesion performance of electroadhesive pads made with this process operated at 700V. Even with some variation, with an approximately 60 g shear adhesion strength, these pads can exceed the adhesion requirements for even larger payloads.

We also consider the HAMR robotic platform capabilities to climb with both its own weight and additional payload. From development of a pull-up testing procedure, we find that the robot is able to carry payloads up to 2 g with around 1 mm forward motion within each pull stride cycle, albeit with potential variation from robot to robot. Future efforts could consider changes to actuator and transmission designs to adjust anticipated force and deflection capabilities, but the 2 g payload test results suggest that the capabilities of the existing design appears to be sufficient. We further consider the impact of payload mounting location to shift the center of mass of the robot. We find that simply by shifting a 2 g payload to the bottom of the robot to lower the center of mass, we can improve static toppling angle from 25 to 45 degrees, which could be helpful for enhanced climbing reliability and less dependence purely upon electroadhesion at such angles. While we consider toppling here briefly as something to be avoided, it could be interesting to explore similar kinds of 'toppling' by shifting around of payloads as a strategy for angling and positioning the robot for potential future surface transitions. With both electroadhesion improved and robot capabilities tested, we lay the foundations for payload-capable inclined locomotion in the future, and turn next to other considerations for real-world usage: rough surfaces.

5

Electroadhesion Pad Design for Rough Inclined Terrains

5.1 Rough Terrains & Motivation

Thus far we have focused the discussion on improvement of the electroadhesive robot in relatively pristine working conditions; in addition to being grounded, the surfaces are well sanded to a smooth flat mirror-like finish with P2500 (8.4 μm) sandpaper. This pristine flat surface is important to electroadhesion, as being able to make close contact directly impacts the ability for the robot to stick well to the surfaces during locomotion. However, envisioning these robots to eventually be useful for real world inspection or search applications will most likely require the capability to navigate all types of surfaces, including terrain with potentially rough or uneven features.

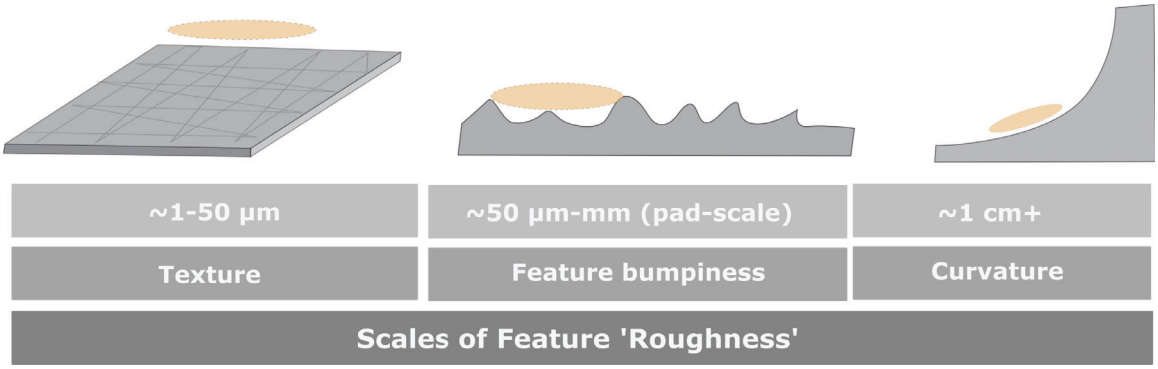


Figure 5.1: Rough surface scales that could be potentially encountered by a robot. Here, we primarily focus on the middle scale, relatively on the same order of scale as the pad.

Regarding rough surfaces, we could consider several potential categories of obsta-

cles a robot may encounter: (1) roughness smaller in scale than the robot (i.e., texture), (2) roughness much larger in scale than the robot (i.e., curvature), and (3) roughness variation on the order of the robot, as shown in Fig. 5.1.

While we briefly consider the two extremes of small scale textures and larger scale curvatures (Fig. 5.2), we consider the middle regime of rough features roughly on the order of pads to be most interesting for exploration and characterization. Previous characterization exists for exploring electroadhesion performance on surface textures of varying R_a average roughness [56] as well as with varying uni-directional, bi-directional, and multi-directional sanding patterns with varying sandpaper grits at different angles [57]. These studies showed increasing adhesion performance with decreasing Sq (root mean square height) roughness, and we observe approximately similar trends in the pads we fabricated (Fig. 5.2C).

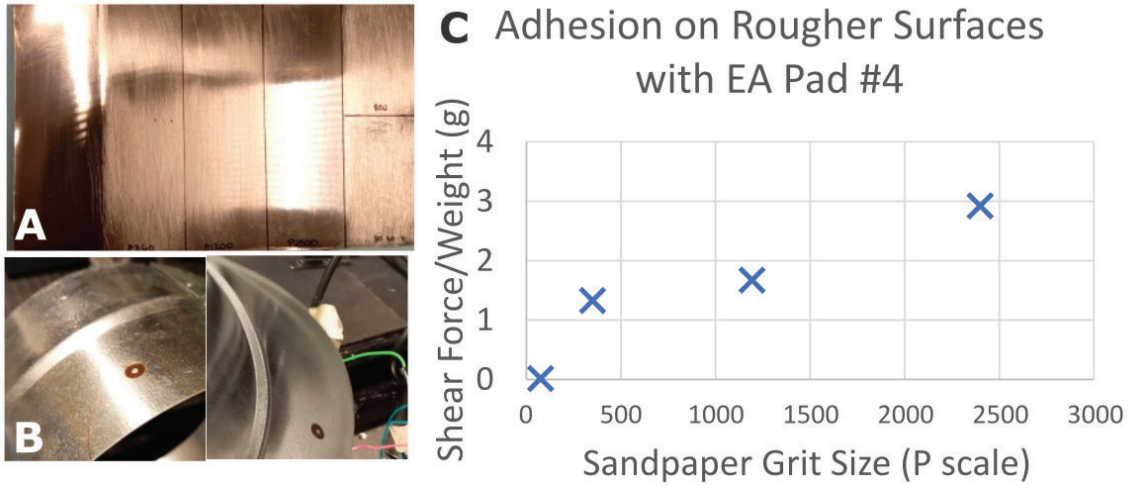


Figure 5.2: Brief considerations of A) smaller scale textures and B) larger scale curvatures. C) Adhesion pressure vs. sandpaper grit size experiments with standard pad 4 from previous section fabrication efforts. Texture tests completed with copper surface bi-directionally sanded with varying sandpaper grit (one trial per point), roughly showing a trend of increasing adhesion pressure with smoother sanded surfaces.

However, the regime of small (hundreds of microns to mm) sized feature terrain bumpiness is a less studied but similar challenging scenario which could be encountered by robots navigating environments. We previously explored performance of a standard (non-electroadhesive) HAMR-VI robot on rough "pocked" (foot scale feature size) and "jagged" (increasingly larger feature size) 3D printed heterogeneous terrains generated using

fractional Brownian motion in work by Schiebel et. al. [58], originally inspired by work from [59]. From studies of various open-loop gait strategies, this study found that on

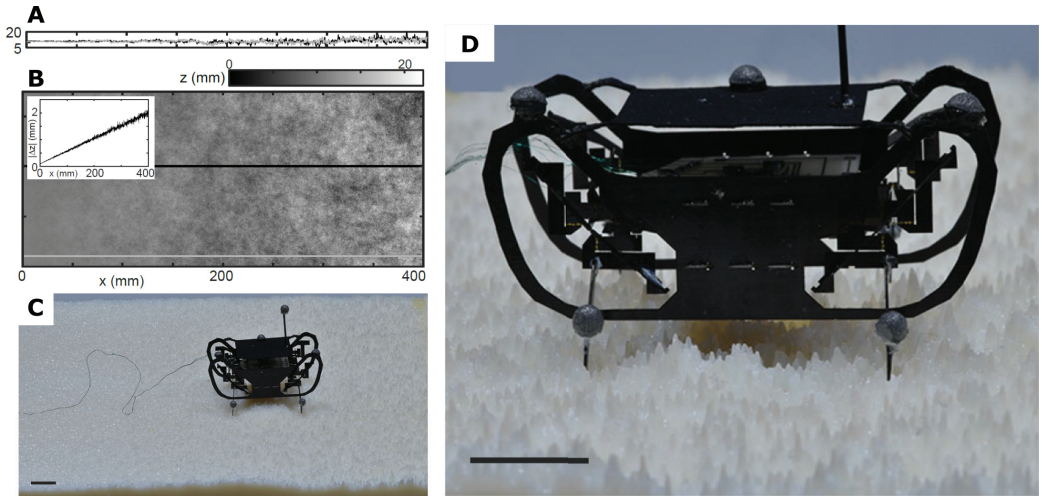


Figure 5.3: Rough Terrain Locomotion Studies from [58]. A) Sideview and B) 2D top view of terrain height variation (encoded as color shade), for a surface made using terrain definitions. C) Sideview and D) closeup view of the physical printed terrain next to a robot for comparison. 1 mm scale bar.

flat featureless or smaller "pocked" feature terrains, both trot and pronk gaits performed similarly, with optimal performance in kinematic running regimes (30-40 hz). Meanwhile on rougher "jagged" terrains, pronk gaits with lower body dynamics frequencies could enable the robot to traverse further into terrain with taller features heights [58]. This work thus outlined the role different open loop gait strategies can play in locomotion capability across terrain with varying feature roughness given a HAMR robot with basic pointed foot design. Extensions of this work have further led to explorations of compliant foot design [60] and leg spine design [61] using similar rough terrains, which show that careful design of leg and foot appendages can improve both level ground and inclined terrain locomotion performance.

We can further adapt the same surface definition methods to our electroadhesive studies as a method of exploring EA pad adaptability to rough surfaces here.

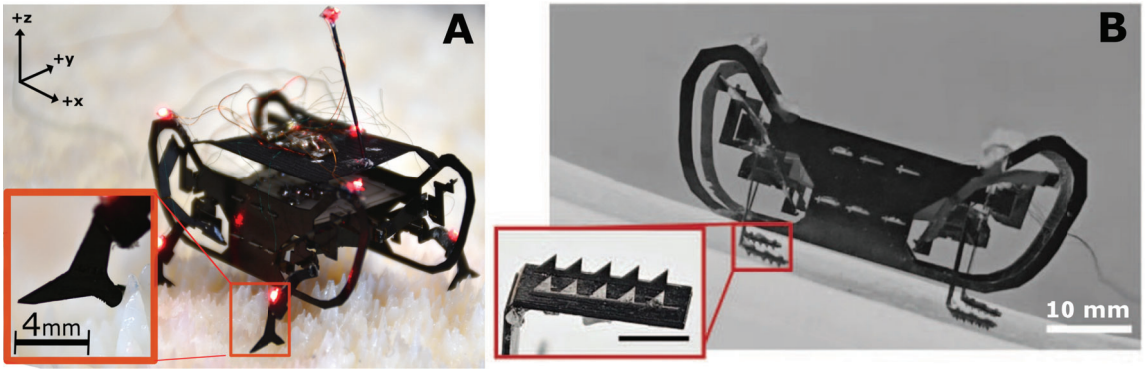


Figure 5.4: Rough terrain locomotion with HAMR - A) Passive foot compliance inspired by insect tarsi enables travel further into a jagged terrain of increasing feature height compared with simple pointed foot design in work by Lechere et. al. [60]. B) Beetle tarsi–inspired robot leg spines aid a robot when climbing low angle inclines with enhanced friction (0-20°) in work from Hernandez et. al. [61].

5.1.1 Overview

This work can be found in "Design for Increased Adhesion Capability of Climbing Microrobots on Diverse Terrains". P. Schiebel contributed to the surface definitions and fabrication and A. Hernandez contributed to statistical analysis.

In this chapter we seek to explore the adaptability of electroadhesion for climbing inclined rough terrains. We hypothesize that by introducing compliance to the pad geometry through incorporation of cantilever beam "spoke" feature designs, we can enhance the ability for a pad to locally conform around terrain heterogeneities and achieve better contact, thus improving the adhesion capabilities.

In the following sections we explore the following: (1) design, fabrication, and characterization of shear adhesion performance for a variety of electroadhesive pad geometry designs which could improve adhesion through increased compliance; (2) definition of a set of stochastic conductive rough terrain samples as representative of challenging climbing surfaces, adapting the rough surface definition methods of prior works [58]; (3) comparison of performance with electroadhesive pad designs on such flat and rough terrain surfaces to understand whether different designs may better suit different surface types, and (4) test of robot locomotion capabilities, with inclines up to 45 degrees using the various types of electroadhesive pads to adhere on rough terrains.

5.2 Electroadhesive Pad Design for Compliance

According to our unipolar electroadhesion model introduced earlier in Eq. 4.1, a larger contact area, increased voltage, and decreased dielectric thickness results in increased adhesion strength, and can be used to tune an electroadhesive pad to better stick to flat surfaces. However, especially when considering materials with local roughness and curvature, the ability for the pad to actually make close contact with the intended surface for actual effective contact area is essential to adhesion performance. A small air gap from the pad not making close contact with the surface decreases the capacitance, both decreasing the relative permittivity ($\epsilon_{d-air} = 1$) and increasing the dielectric thickness (d) gap. We hypothesized that by making the pad more compliant through the introduction of 'spoke' features that allow a pad to locally conform to surface heterogeneity, we could improve the performance of pads on less pristine rough surfaces or terrains, as shown in Fig. 5.5(B-C).

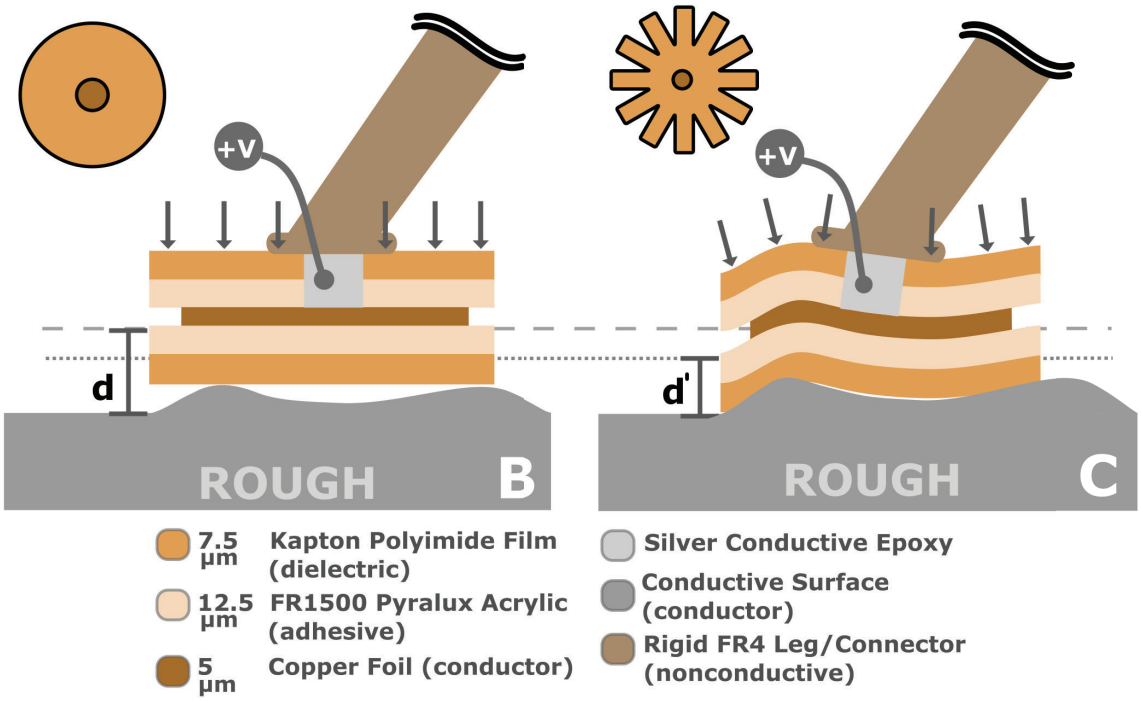


Figure 5.5: Diagram of electroadhesive pads on flat and rough terrains (not to scale). (A) All pads lay relatively flush to the surface on flat terrain. (B) Noncompliant pads may have air gaps which increases d and reduces electroadhesion. (C) Spoked designs may be able to bend and conform to surfaces better, thereby reducing d and increasing the adhesion force.

We can approximate spoke compliance roughly as similar to cantilever beam bending, where the center point is fixed and the distal end is free to bend and deform. Based on this assumption of beam bending, we anticipate increasing the length will enable greater spoke deflection, and thus a smaller air gap. Accordingly, with a smaller gap the dielectric thickness should decrease, with its inverse square relationship to the adhesion force resulting in higher adhesion capabilities. Increasing the perimeter to area ratio of the design by introducing spoke features has the potential to introduce fringing edge effect considerations. However, given the scale at which we have designed features (high spoke width to effective gap distance ratio) we consider fringing effects negligible [62]. We selected a range of designs with varying spoke length, width, and spoke angle to explore the effect upon adhesion. Selected designs are shown in Fig 5.6.

The electroadhesive pads were manufactured using the thin kapton film (d = 7.5 μm) multi-layer laminate fabrication approach introduced earlier and outlined in Fig. 5.7.

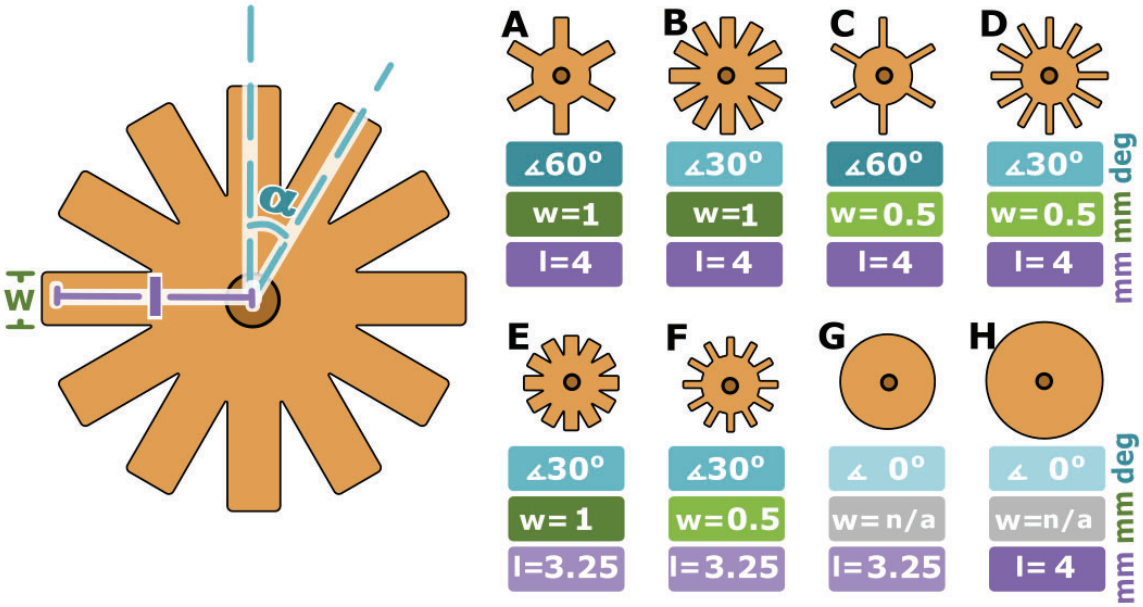


Figure 5.6: Design of electroadhesive pads with compliant spoke features: α the angle between spokes, l length, and w width of spokes are examined with varying parameters across the set of A-H pad geometries tested.

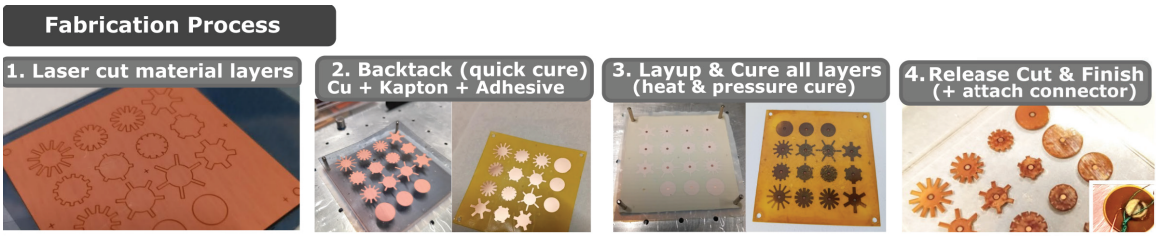


Figure 5.7: Left: Material layup of the electroadhesive pads, with five layer laminate of kapton, adhesive, and copper foil. Right: Fabrication process used to create batches of pads with pin-aligned lamination.

5.3 Methods

5.3.1 Electroadhesive Pad Experimental Test Setup

In order to assess the performance of each electroadhesive design, shear force tests were conducted to determine the maximum shear adhesion of a single pad. Shear forces (dependent upon the coefficient of friction (μ) according to $F_{shear} = \mu F_{normal}$) were used as a measure of adhesion capability since this is most relevant for a robot climbing against gravity on a vertical plane.

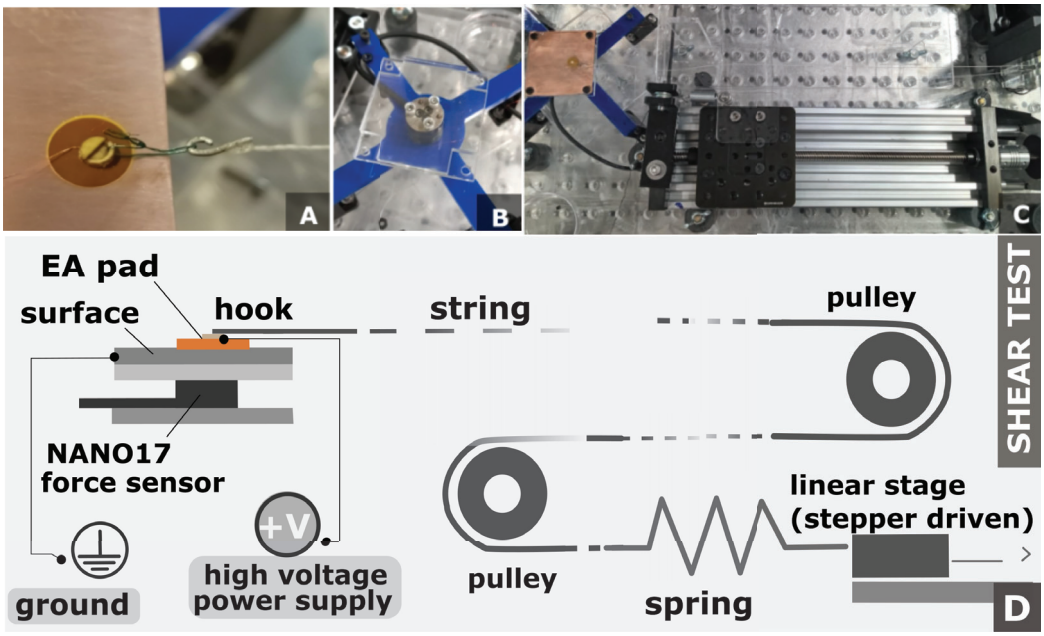


Figure 5.8: Experimental setup for electroadhesive pad designs. Top: Top view of the hook attachment mechanism used to attach and pull pads in shear. Bottom: Side view diagram of all components, including the Nano-17 used to measure forces, and the linear stage and motor used to exert increasing force via a string and spring pulley system. *We thank Fabian Landers for assistance with initial design of this system.*

A linear stage (OpenBuilds C-beam) and stepper motor (NEMA23) test fixture was used to test the maximum shear adhesion of a surface-engaged electroadhesion pad. By pulling the pad through a low-friction pulley system (Fig. 5.9) with a string-spring attachment to the stepper motor, a steadily increasing force was applied until pad slippage occurred. To ensure uniform pad loading in the shear direction, a rigid FR4 connector ring with compliant loop on the pad could slide to align with the direction of pulling force exerted by a hook attachment. A high resolution force/torque sensor (Nano-17) was mounted

beneath the electrically grounded surface terrain sample, while a high voltage amplifier (Trek 2200 series) supplied voltage to the electroadhesive pad. While this setup could deliver up to 2000V to the pad, preliminary tests of pad limits found dielectric breakdown and shorting beyond 1200 V. Thus 750 V was selected as a relatively high operation voltage for stronger overall adhesion and performance while avoiding shorts during trials. The linear stage motor driver, sensor readings, and electroadhesion voltage were controlled using a DAQ card (USB-6001, National Instruments) all controlled by a LABVIEW script.

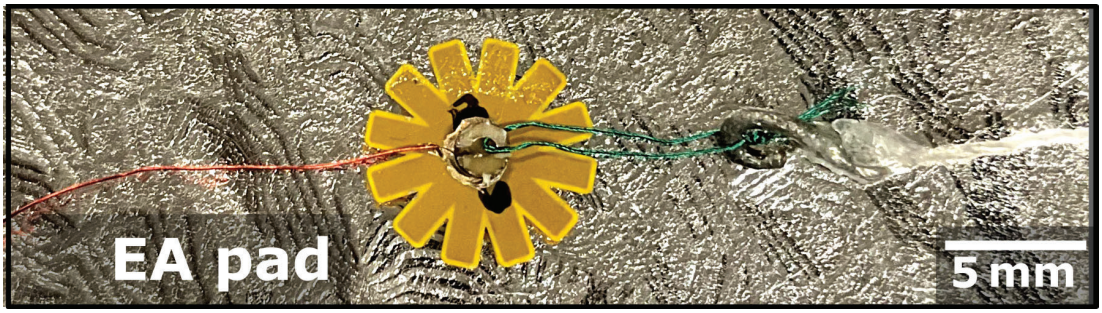


Figure 5.9: A close up view of a spoked pad on a silver-coated 3D printed test surface, attached to hook for pulling.

During each run, the electroadhesion pad was loosely attached to the shear loading system and placed on a random section of the terrain sample with an initial 1.5 g nonconductive weight on top to keep it in place. A typical test proceeded as follows: the high voltage source was turned on (750 V) to initiate electroadhesion engagement. Following engagement, the initial weight was removed, the force sensor data collection began (1000hz sampling), and the motorized stage began to pull the string until engaged, loading the pad in the shear direction. Data collection and loading continued until the pad noticeably slipped or fell off, at which point motors, voltage, and sensing were turned off and reset. Each pad design had at least three copies, with each copy being removed for at least thirty minutes between trials and grounded to ensure full static discharge before retesting.

5.3.2 Surface Definition and Fabrication

Our aim in this work was to determine whether increasing pad compliance would improve electroadhesion force on nonuniform surfaces. Thus, it was necessary to design a test surface which had well-defined yet random heterogeneities at the scales of interest. We used fractional Brownian motion (fBm) to generate random yet parameterized terrain heights (for details, see [59, 58, 61]). The character of these terrains is determined by the

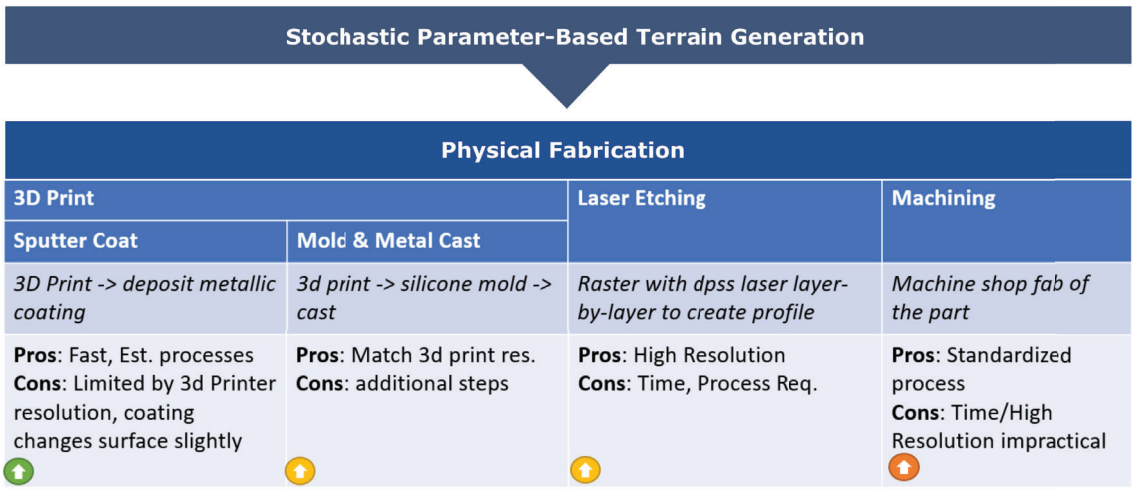


Figure 5.10: Potential fabrication methods considered for physical fabrication of the parameter defined surface using fractal Brownian motion techniques. While a few different processes were considered, 3D printing and sputter coating was selected as the fastest method for rapid iteration over different conductive rough surfaces.

Hurst parameter, $0 < H < 1$, which is related to the correlation between adjacent features. In this work, we used $H = 1$ resulting in localized terrain features and terrain which qualitatively appears "pitted" or "pebbled".

The spatial scale of the features was defined by the distance between adjacent features in the horizontal plane, and by the average distance between adjacent heights in the vertical direction (see Fig. 5.12(iv) for coordinate system). We used a MATLAB script to generate the feature heights using fBm, scale them to the desired spatial dimensions, then exported the resulting surface to a file for a 3D CAD program or 3D printer. While a few different processes were considered (Fig. 5.10), 3D printing was one of the fastest options, albeit with limited 3D printer resolution.

Terrains were fabricated using a 3D printer (Stratasys Objet30 Polyjet Printer, 30 μm resolution, VeroWhite). Surfaces were sputter coated with a thin silver layer (Denton Vacuum Desktop Pro, Ag, 4 min, 300 mA, approximately 0.2-0.3 μm thick) to make them electrically conductive. The physical resolution limitations of fabrication (i.e., resolution of printing and sputter coating) likely add some small degree of spatial low pass filtering over the originally mathematically-prescribed script-generated terrain geometries. While high spatial frequency features may be attenuated (due to the finite resolution of our surface fabrication method), this same process was applied equally to all samples for consistency

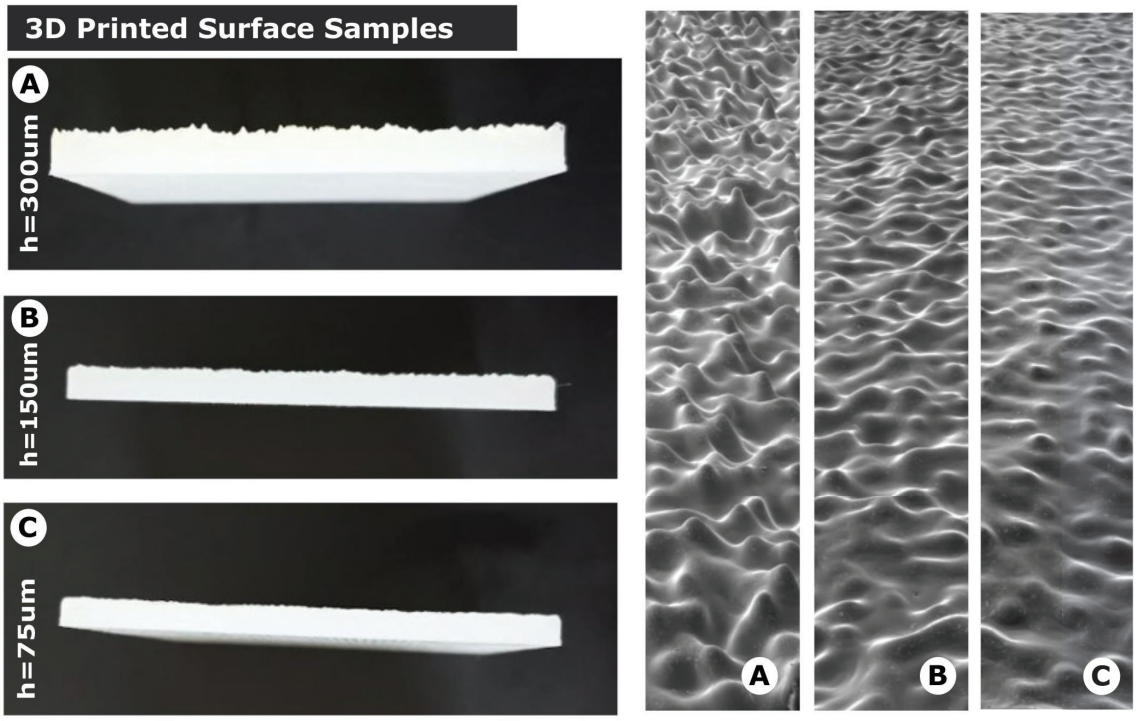


Figure 5.11: Images of 3D printed and sputtered terrains. Left: Sideview photograph of surfaces (each terrain is 5 cm in length).h denotes the z-axis height of the terrain. Right: Iso view of the same surfaces (corresponding to same letter labels) after sputter coating, when imaged with scanning electron microscopy (SEM). The width of each image section is 0.25 cm across (in the front of the image), with each surface tilted at 65°. *All SEM images taken by James Weaver, who provided much invaluable imaging and analysis suggestion and experimentation.*

across performance comparisons. A closeup of a few types of surface terrains generated with this 3D printing method, including both macro sideview and closeup SEM imaging, can be seen in Fig. 5.11.

Examples of terrains with the same $H = 0.1$ and different spatial scales are shown in Fig. 5.12(ii). In preliminary tests over a range of potential surface options (A-D), we generally found that the more closely packed, higher feature height terrains were more challenging for elecroadhesive pads to achieve measurable adhesion forces on. Such terrains could lead to forces so small that pads failed to even make initial electroadhesion attachment to the surface, making reliable shear adhesion force measurements over all pad varieties difficult. Thus, for the electroadhesive pad performance assessment in this study we

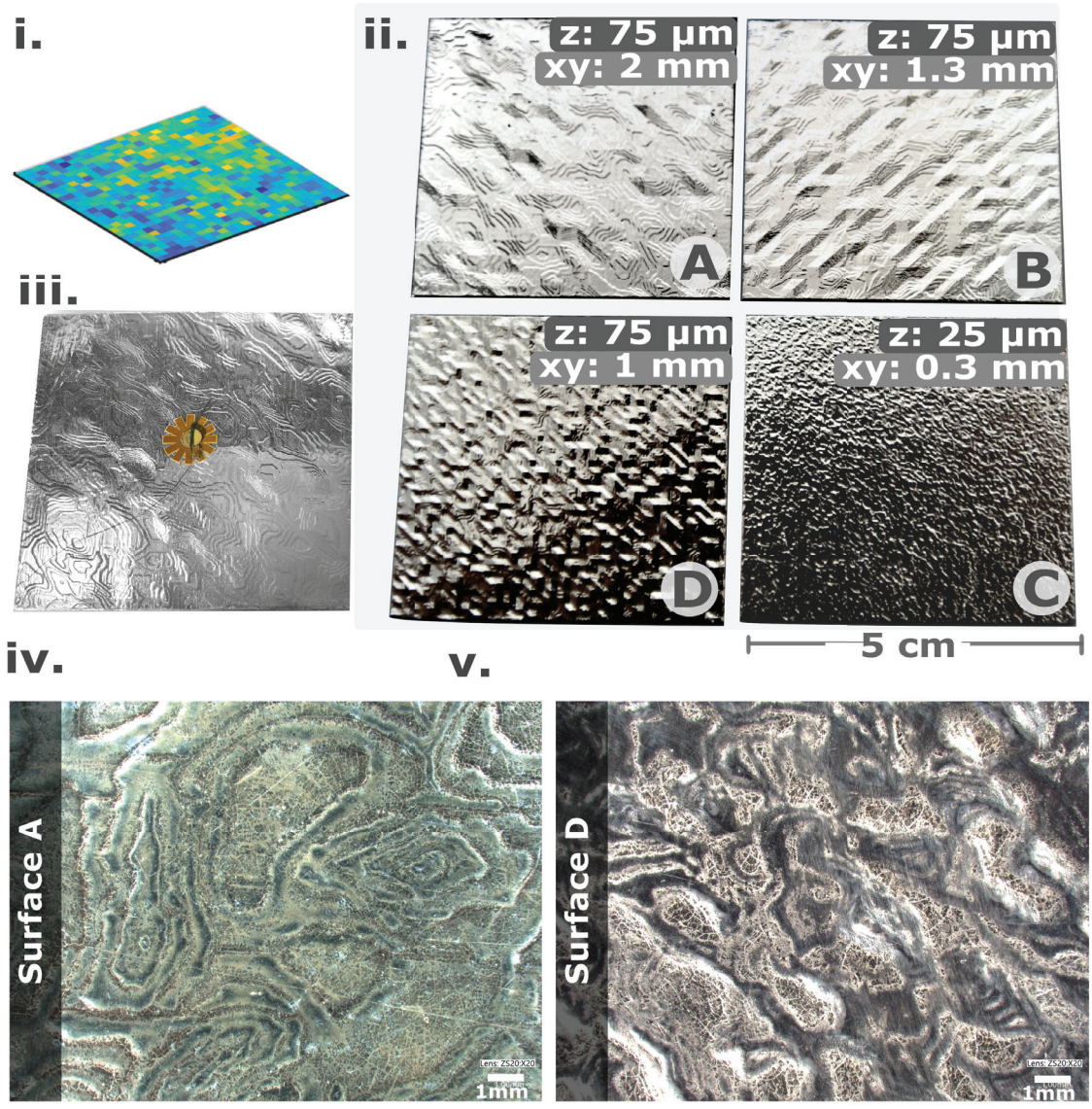


Figure 5.12: (i). A method was developed to fabricate varying roughness terrains from computer generated models. (ii). Terrains were 3D printed and sputter coated with a conductive metal (silver). Approximations of the coefficients of static friction between kapton-Ag surfaces were measured from inclined plane experiments (five trials per surface) and reveal $\mu = 0.24 \pm 0.03$ for our flat surface and $\mu = 0.27 \pm 0.04$ for surface A. Surface A was selected for pad experiments, while surface D was used in later robot incline climbing comparisons. (iii). Photograph for relative size scale of pad and terrain (iv) and (v). Surface photographs were taken with a Keyence VHX-7000 microscope.

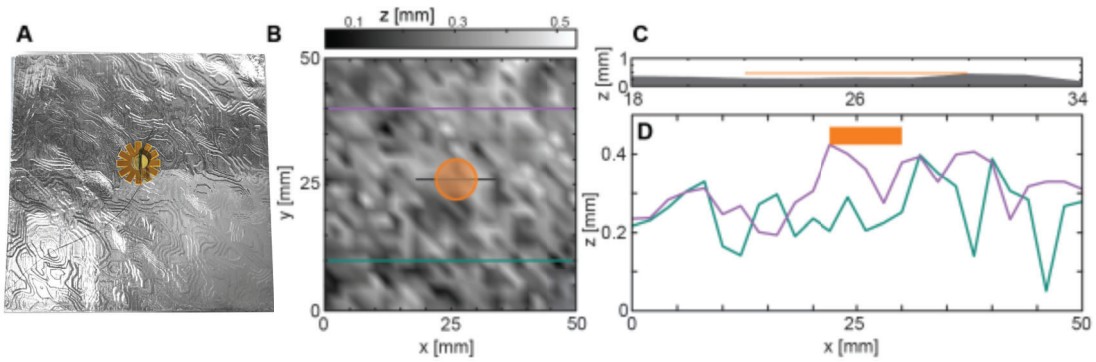


Figure 5.13: A) Photograph of 5 cm rough conductive terrain. B) Heatmap of the computer-generated surface heights used to print the terrain in A. z (color shade intensity) denotes average feature height of a terrain, while xy denotes the horizontal feature scale. Orange circle shows the size of the 8 mm diameter pad. C. Example side-views of the computer-generated heights. The thin orange rectangle shows the relative pad dimensions (thickness and diameter) to scale compared with vertical feature height and lateral terrain distance scales, with zoomed in version in D.

elected to focus on surface A, a terrain with average feature heights of 75 µm and horizontal feature scale 2 mm. Fig. 5.12(iii), shows a representative surface A selection where the pad scale relative to terrain features can be observed. Fig. 5.13 shows both the photograph of physical surface (A), as well as the generated terrain definitions (B), including sideview of height profiles (C and D).

Following initial pad testing we also performed later robot-level testing using the better performing pads. Because in robot-level testing multiple electroadhesion pads attach to the surface (with the gait used, at least three pads remained adhered at any given time), the overall robot adhered better than a single pad. We found that several of the pad types all climbed on our maximum 45° test incline reasonably well, making comparison less pronounced. We therefore selected a more challenging representative terrain surface D (75 µm feature height, 1 mm horizontal feature scaling) with closer asperity spacing for later robot tests to balance adhesion capability against greater climbing challenge and to more clearly demonstrate the climbing capability differences between different pad types. While these two terrain samples were selected for comparison across pad and robot performance in these trials, this general method of mathematically defining, 3D printing, and sputter coating terrains for testing could be extended to a wider variety of feature heights, feature spacing, and H-parameters beyond the specific terrains focused on here.

5.4 Experimental Results

5.4.1 Data Processing

For each trial, the force data was analyzed to identify the maximum peak shear force the pad could sustain before slipping, as shown in Fig. 5.14. Enough data was taken such that at least three data points were collected for each pad type to get a representative sampling of relative performance, however exact trial counts varied from pad to pad due to fabrication limitations (some yield loss during batch fabrication and/or loss of pads during testing itself) that led to fewer tests for some categories. The total number of tests per pad type can be found in Fig. 5.15. Because the stepper motor introduced vibrations to the system while pulling, noise in the data was filtered out using a non-causal filter (Butterworth 6th-order low pass, 1.5 Hz cutoff frequency).

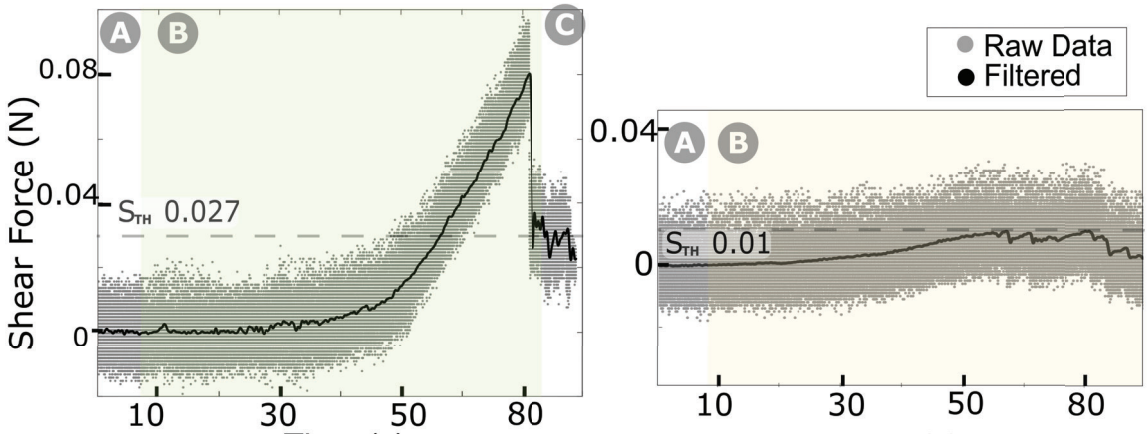


Figure 5.14: Representative plots of force vs time for a full pad pull trial, demonstrated using two pads on surface A. The force sensor data is shown raw (grey) and after filtering (black). Section (A) represents the initial seven seconds of data taken with the motor on but no force applied. This data was used to zero the force data for each trial (minor sensor drift could occur over time). Section (B) is the main portion of the data collection. After the motor is run for some time, the shortening string- spring tether eventually engages to pull the pad, resulting in an approximately linear ramping increase of shear force. In (C) the pad has slipped, surpassing the maximum shear load the pad is able to withstand in this trial. Note the slight jumps at the end indicating stick-slip behavior. The stick threshold (S_{TH}) for the pad given the adhesion criteria is marked with a dotted line. Left demonstrates an example of a successful trial using pad H (ramp-peak behavior that exceeds the criteria), while the right trial using pad C demonstrates a run that did not meet the minimum criteria.

In addition to data filtering, we also specified a threshold to both examine the effect

of adhesion consistency and ensure that only trials with an appreciable amount of adhesion were counted in our adhesion strength measurement. For this threshold, an adhesion criteria of 540 Pa (the adhesion pressure required to ensure the smallest pad could withstand at least 1g of shear loading) was selected. Different threshold options (such as a fixed force, or based on the standard deviation of the noise) were also considered, but this option allowed for pressure comparisons across the sample set.

5.4.2 Performance Metrics

Following the testing and data processing of electroadhesive pads on flat and rough terrains, several metrics were used to analyze the relative performance of the pads:

- **Percent Stick (%)**: Percentage of all trials that met the adhesion criteria ($>$ 540 Pa).
- **Shear Adhesion Pressure (Pa)**: The shear adhesion pressure of the pad ($\frac{\text{force}}{\text{pad area}}$) for only those trials which met the adhesion criteria ($>$ 540 Pa).

5.4.3 Electroadhesive Performance of Circular and 'Geometrical' Designs on Flat Terrain

From initial testing on flat surfaces, a baseline understanding of performance was determined. We observed that all pad types were capable of meeting the adhesion criteria, with 80-90% of the geometrical pattern trials and over 50% of circular pattern trials passing the selected threshold (see Fig. 5.15). The larger area pads appear to have slightly better performance than the smaller ones, with a higher stick rate and median, though no statistical significance was determined. A simple parallel plate capacitor model of the pads would suggest equivalent pressure performance across pads. However, we hypothesize that larger pads in practice may do slightly better since given their larger size they are more compliant, allowing one well-adhered spot to pull the rest of the pad closer to the surface for better engagement.

We note there is variation in our data for even this baseline flat testing. Electroadhesion testing can have high variability, with elements sensitive to various environmental factors such as humidity, pressure, or temperature, as well as potential for stray residual charges that may linger within the dielectric materials even after thorough electroadhesive pad and surface grounding. There may also be some slight fabrication variations (a result

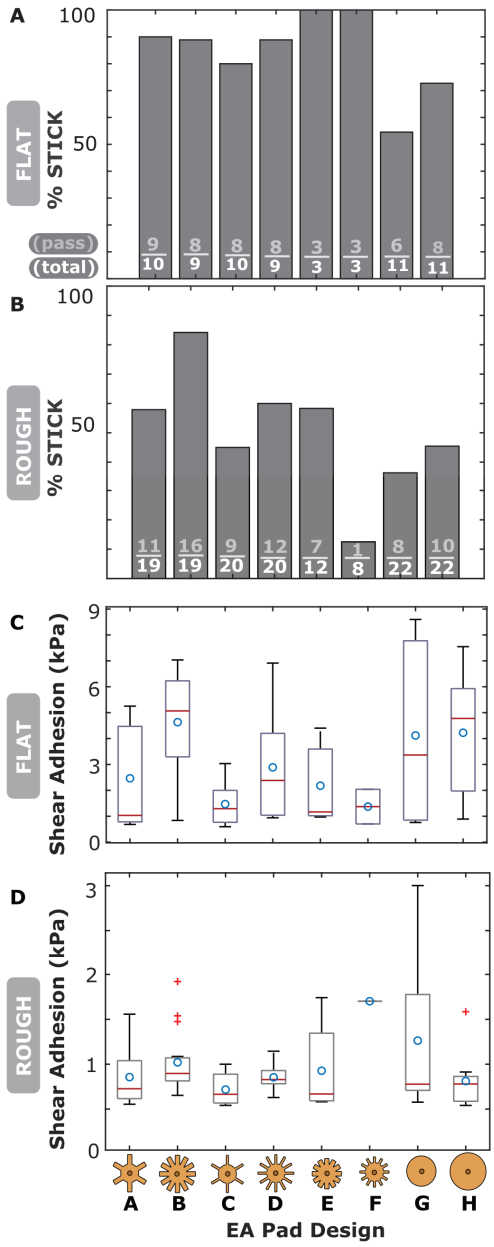


Figure 5.15: Flat and rough surface performance characterization of different EA pad geometries, as indicated by illustrations below the horizontal axis. In (A) and (B), the percentage of pads that met the adhesion criteria is shown for flat and rough surfaces, respectively. The total number of tests (in denominator) and number of tests which pass the selected "stick" threshold criteria (in numerator) are marked for each pad type. In (C) and (D), the shear adhesion pressures are reported for the subset of trials which met the adhesion thresholds. Means are indicated by blue circles, medians denoted by red bars, grey boxes indicate the interquartile range and black whiskers indicate minima and maxima. Data points >1.5 times the interquartile range from the median are red stars.

of hand-assembly manufacturing imperfections) in addition to plastic deformations in the pads from operation and handling which can further contribute to some of the variability seen within the data set.

5.4.4 Electroadhesive Performance of Circular and 'Geometrical' Design on Rough Surfaces

On our rough selected terrain (surface A), the ability for pads to meet the adhesion criteria varies more noticeably. In particular, one of the more compliant designs (e.g., pad design B) maintained roughly 84% stick rates, while circular pad designs achieved only 36% - 45% stick rates.

Relative performance of specific pad design variables such as spoke angle or length were also explored. We find that generally the longer spokes and smaller spoke angle (thus greater number of overall spokes), led to pads with more reliable adhesion stick percentages. For example, we see that pads B and D ($l = 4\ mm$, angle: 30°) stick more reliably (84% and 60%) compared to pads E and F with shorter length (58% and 13%, respectively). B and D similarly perform better than ($l = 3.25\ mm$) pads A and C (58% and 45%) with greater angle (angle: 60°). We note that the shear adhesion strength of such pads may be similarly higher for these longer and lower spoke angle features, though no statistically significant distinctions could be drawn from the data given the stick thresholding filter adhesion criteria. Changing the thresholding filter criteria could result in different comparisons (Fig. 5.16), but we stick with pressures for comparison.

As a baseline comparison, we also tested pads G and H (small and large circular pads). While the smaller circle appeared to have a higher mean shear pressure, it had a wider variability and much lower stick rate (36%), meaning the majority of trials yielded poor performance below the minimum adhesion thresholds and were filtered out of the aggregated pressure results. While adhesion pressures are helpful for comparison, we consider meeting minimum adhesion requirements to reliably step forward to be most relevant for improving the success of a climbing robot, thus we particularly focus on this stick rate for determining performance. On the basis of its more reliable (84% stick rate) performance on rough terrains, pad type B performed the best of the compliant geometries, and was selected for robot-level inclined climbing tests.

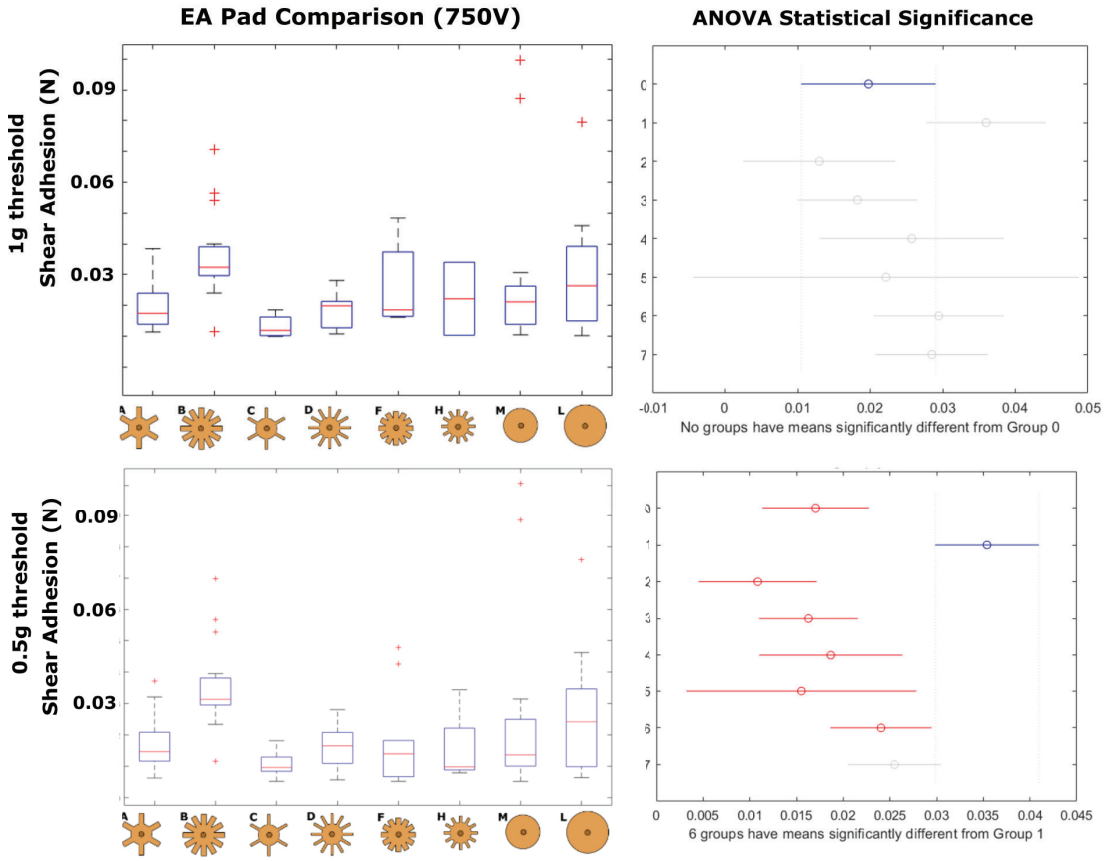


Figure 5.16: Alternative thresholding options for data analysis. The choice of criteria for determining an engaged 'stick' could make a difference in analysis of results. For example, choosing a small force-based metric of comparison (0.5 g, roughly the amount of weight we envision each leg needing to hold during a tripod gait), we can see the significance of different pad options change, with B more clearly being highlighted.

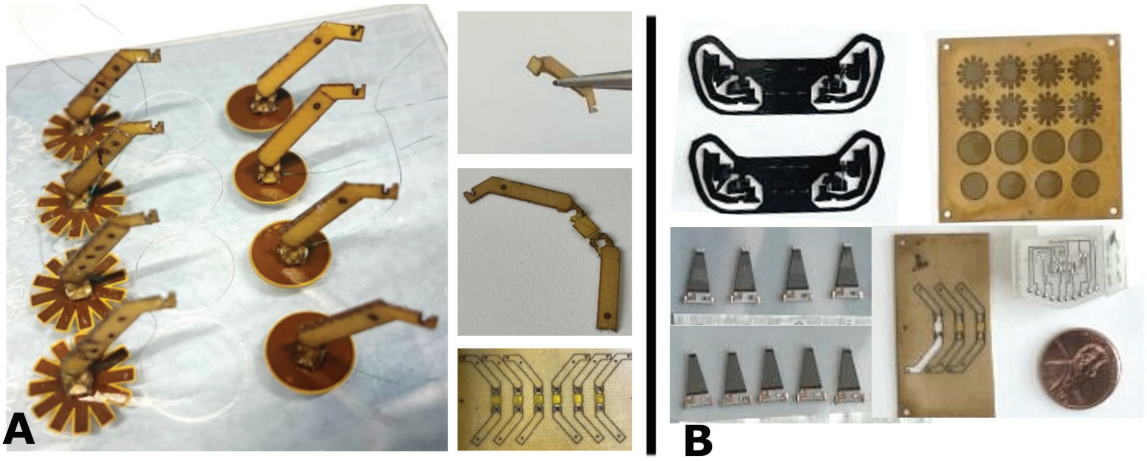


Figure 5.17: Fabrication of the HAMR-E robot foriInclined testing. A) Closeup of electroadhesive pads and legs. B) All components, including chassis, actuators, circuit board are shown with a penny for scale comparison.

5.4.5 Robot Inclined Climbing Demonstration

Using the electroadhesive pads designed and characterized in the previous section, a robot comparison demo was conducted to explore inclined climbing performance. A HAMR-E robot was constructed using the fabrication processes similar to prior work [13] (Fig. 5.17), with general robot manufacturing method improvements described in earlier chapters. We also use the same six degree of freedom ankle joint used in [13] to connect the pads to the legs. These joints provide ankle-level compliance, enabling the pads to stick and remain adhered to the surface regardless of precise leg angles, which change over the course of the gait cycle. The completed robot with newly designed pads can be seen in Fig. 5.18. The robot was run with a tripod gait described by [13] using a single set of gait parameters across all trials (actuator voltage: 175 V, frequency: 0.2 Hz, duty cycle: 4%, ground offset: -25%, lift compensation: 0, lift offset: 90%, swing amplitude: 100%). Slight phase offsets aligned swing and lift gaits, and individual leg offsets were tuned to account for leg imperfections.

A set of spoked pads (pad B), small circles (pad G), and large circles (pad H) were selected for comparison testing and were fixed to ankles and legs to facilitate changes between tests. The surface area of the compliant pad selected (B, 37 mm^2) falls between the areas of the two circular options (G, 33 mm^2, H, 50 mm^2). These pad sets were tested on three different surfaces types: a flat surface, a slightly rough surface (surface A), and

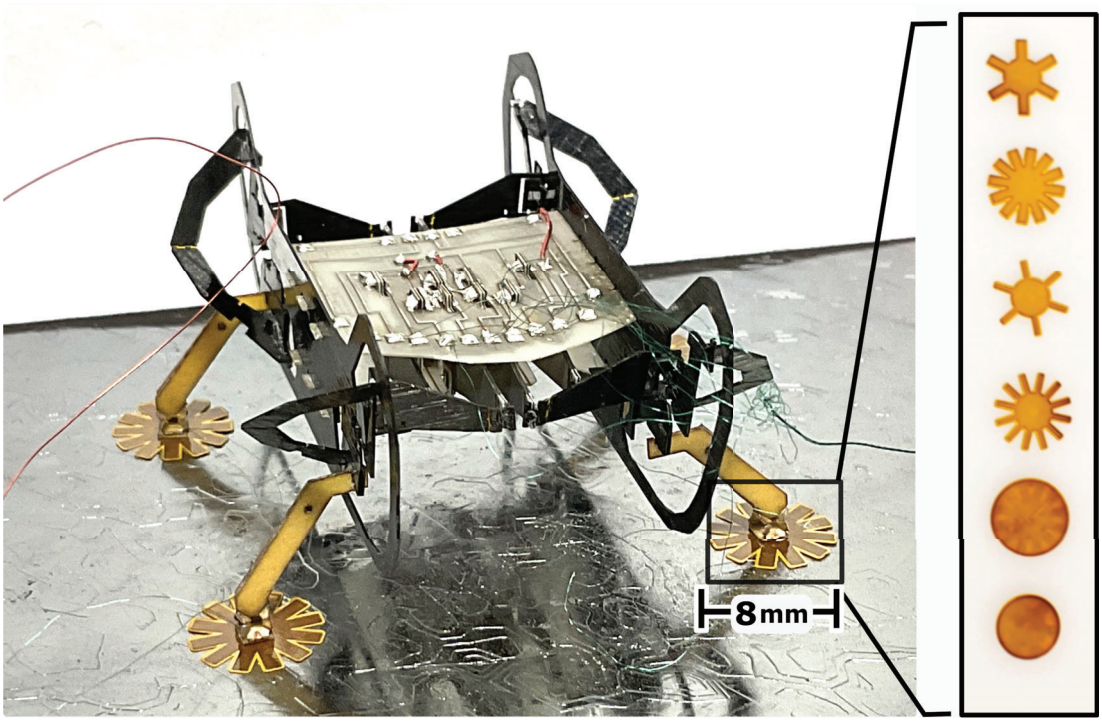


Figure 5.18: HAMR-E+ (1.45 g, 4.5 cm microrobot) with compliant electroadhesive pads for traversal of rough, non-uniform conductive terrains, such as this 3D printed and silver-coated terrain. Examples of 2D electroadhesive pad geometries manufactured and tested in standalone pad tests (right inset).

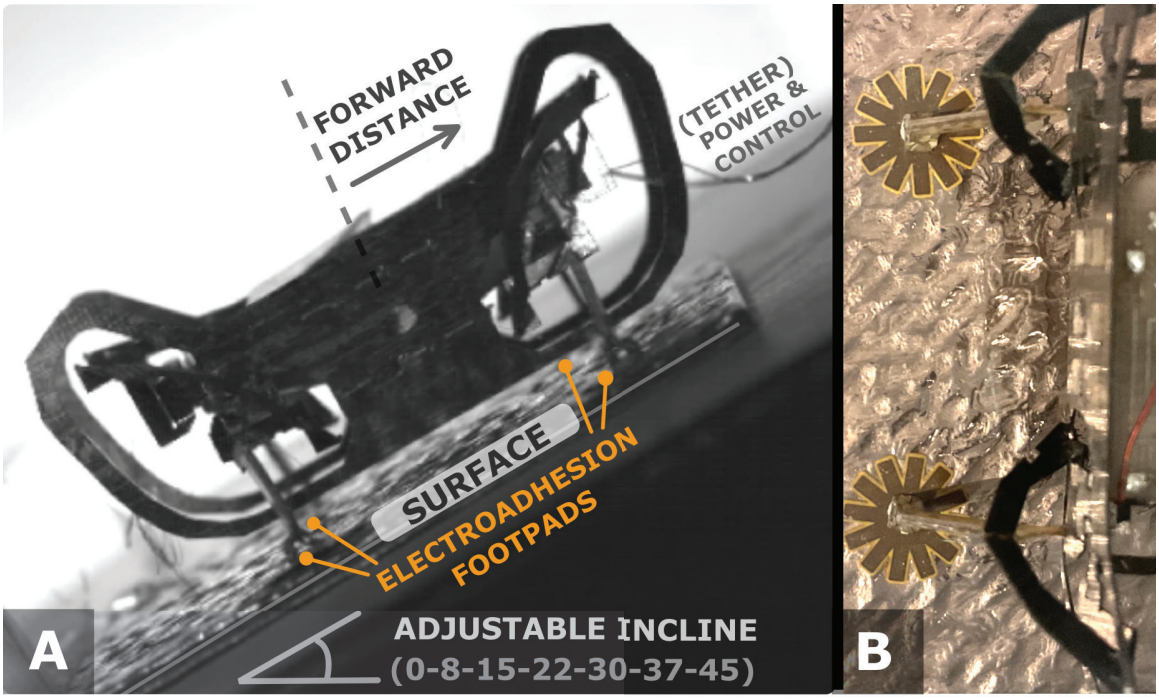


Figure 5.19: A) Robot performance was tested using an adjustable incline (0-45 degrees) and three interchangeable surface roughness terrain samples. Video capture of climbing was used for frame analysis in ImageJ to determine overall center of mass climbing speed. B) Closeup top-down view of the robot on the rougher surface D used for robot inclined climbing tests.

rougher surface (surface D), with electroadhesion voltages of 200V, 400V, and 500V. At higher voltages the robot would stick to the surface and struggle to detach itself, with this effect especially pronounced on the flat terrain. These voltages were selected as values which allowed a large circular pad to both stick and disengage well on each surface at an angle of 15 degrees, then used throughout all pad trials of the same surface type. Each surface was tested at a range of inclines of 0° to 45°, with testing angles as shown in Fig. 5.19 and examples of forward distances travelled in Fig. 5.20.

The results of these tests can be seen in Fig. 5.21. We observe that, as anticipated, climbing speed (as measured in % bodylength per step cycle) generally decreases as surface incline increases. Eventually, at higher inclines, climbing speeds reach a point where, depending upon the pad and surface combination, the robot can no longer make forward progress. While speed may be less critical if tasks have no time constraints, ultimately a robot's ability to achieve locomotion within a reasonable time frame (and eventually, operate on limited battery and power resources) remains important. Somewhat counter-

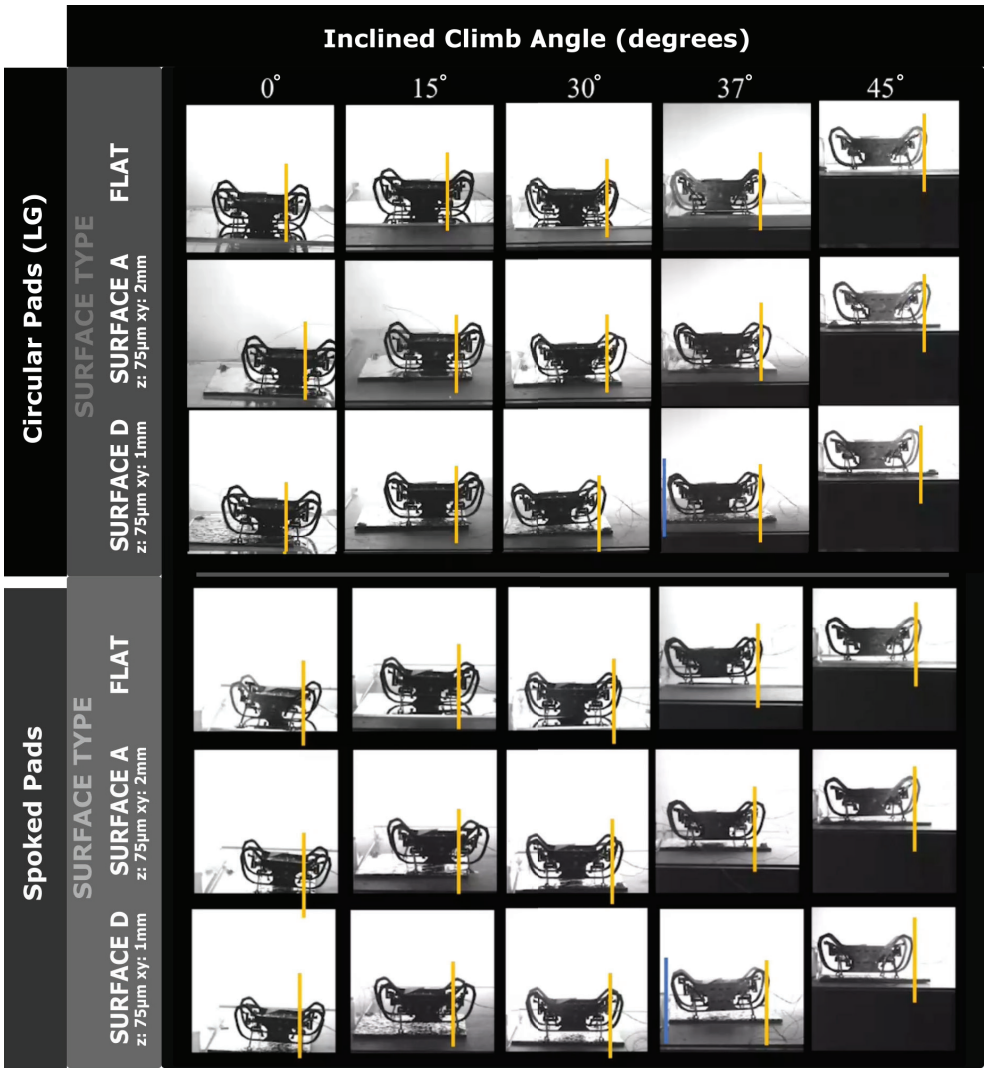


Figure 5.20: Inclined climbing tests. The columns show the angle of incline (0 to 45 degrees), while two different pads (circular and spoked) and surface types (A, D, and flat) are shown in individual rows. The camera angle is adjusted with angle so all video capture has the same alignment for forward distance measurement. The yellow bar shows where the front edge of the robot chassis begins in the first frame, with current snapshot above showing the distance the robot has gone in approximately 45 seconds (15 step cycles at 0.2Hz frequency). Trials were repeated three times.

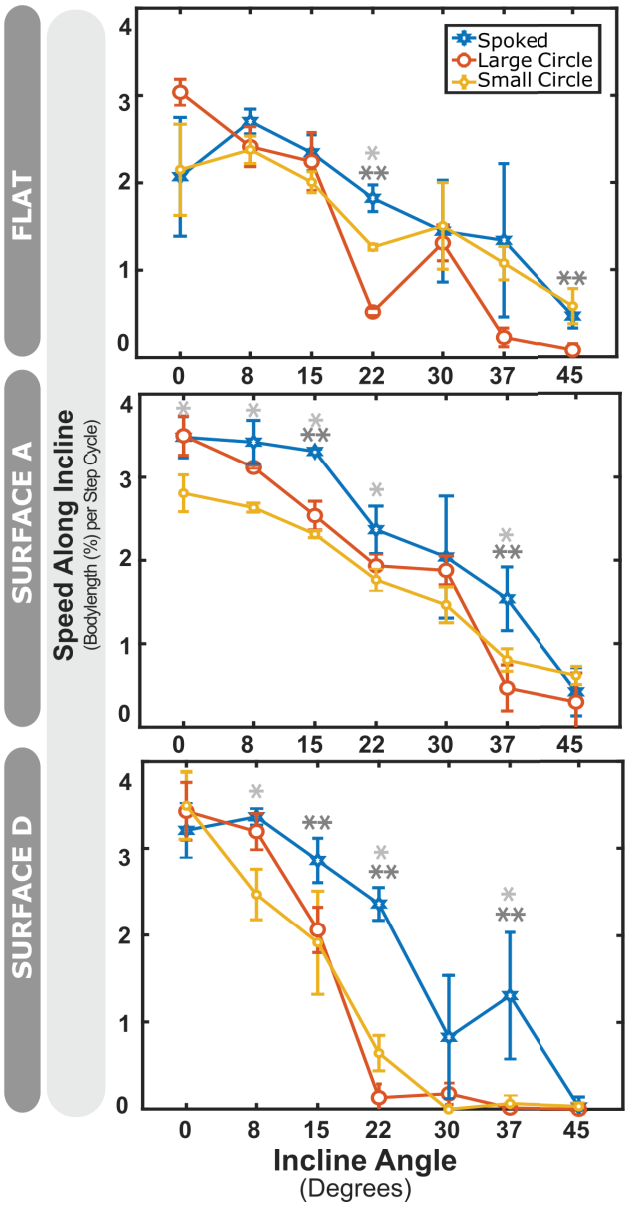


Figure 5.21: Inclined climbing performance of the robot with three representative pads from Fig. 5.6: spoked (pad B), large circle (pad H), and small circle (pad G) run over three different terrain types (flat, surface A, surface D). Each climbing trial condition was tested with three data points. Statistically significant differences (as determined by $p < 0.05$ when performing a one-way anova analysis for the pad types at given surface and incline angle) between the spoked and small pad are denoted with $*$ while differences between the spoked and large pad performance are denoted with $**$. Inclined tests at 0, 15, 30, 37, and 45 degrees were first completed in randomized order with trials at 8 and 22 degree angles added in subsequent trials.

intuitively we find that the robot had slightly slower speeds on the completely flat surface (for the large pad robot, an average of 39 % slower across all angles compared to surface D) – we speculate that excessive adhesion due to residual charges on the flat surface may have resisted forward motion, while slightly rougher surfaces enabled pads to more easily lift and move forward.

We observe that on surface A (Fig. 5.21B), all trials using the different pad types are able to make some degree of forward progress even up to inclined angles of 45 degrees. The robot with spoked pads generally has a slightly greater climbing speed, with an average 48% speed increase across all angles when compared to the robot with large pads. We find that on the more densely feature packed surface D (Fig. 5.21C), the circular pads could only achieve noticeable (speed greater than 0.5% BL/stepcycle) climbing on inclines up to 22 degrees, while the spoked pads are able to climb until 37 degrees (a 15 degree increase), demonstrating the capability of the spoked design to improve climbing capabilities (Fig. 5.22).

We can summarize our robot-level climbing findings: a) on flat surfaces there is minimal statistical difference between the top performing circular and spoked pad designs (as expected); (b) on surface A, where the majority of designs were able to achieve some measurable climbing performance for inclines 0-45 degrees, we see an average increase in climbing speed of 48% between the top spoked and circular designs; and (c) for a more aggressively rough surface (surface D) we see inclines where circular pads do not adhere but the spoked pads can still maintain adhesion and climbing capability. There was a minor decrease in climbing speeds for circular pads at 22 degrees, possibly the result of later added trials as noted in Fig 5.21. We speculate there may be wear of the pads during usage; a characterization of wear and degradation across pad designs could be explored in the future.

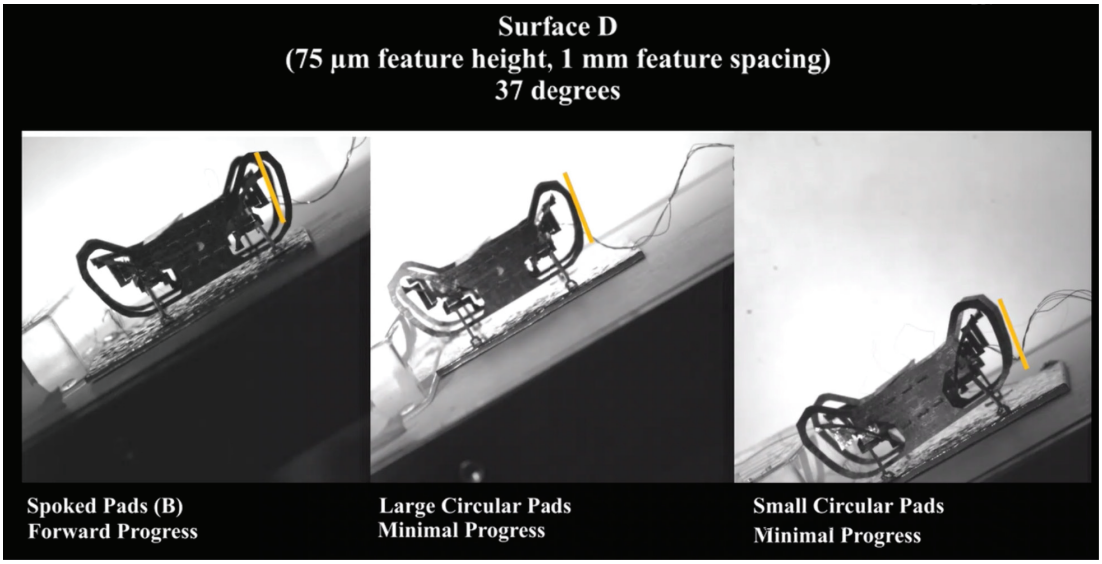


Figure 5.22: A comparison of climbing performance on a 37 degree incline: The spoked pads are able to make forward progress up the incline on surface D, while large and small circular pads do not.

5.5 Discussion and Summary

In this work we demonstrated the fabrication and characterization of a 4.5 cm microrobot using compliant footpad geometries to enhance electroadhesion when traversing rough conductive terrains. We conducted an investigation of the electroadhesive pad design space and characterized the shear force climbing capabilities of the robot with different pad designs. We find that on smooth, flat terrains, a large simple circular footpad structure exhibited the greatest shear forces. However, on rougher inclined surfaces, pads which adjusted the width, length, and number of spoke-like features provide greater compliance and achieve more consistent shear adhesion forces. Such compliant spoke pad designs on rough surfaces performed with 84% stick reliability and 1.02 kPa average adhesion pressures, compared to 45% stick reliability and 0.81 kPa average adhesion pressures for a comparable circular pad. We demonstrate the improved climbing capability of the 4.5 cm robot on terrain with 75 µm roughness and observe an average increase in climbing speed of 48% over a range of angles from 0-45 degrees.

In this chapter we characterize and demonstrate improved adhesion capabilities of a compliant spoke geometry with a primarily experimental approach. While differences between specific pad parameters were too small for drawing significant conclusions during

individual pad testing, we observed that longer spokes generally tended to perform better than shorter ones, supporting our hypothesis that cantilever beam-based designs with greater deflection capability may increase compliance and thus adhesion. The simple rectangular spoke investigated here was chosen for initial investigations primarily for simplicity, however complex shapes with more compliant space-filling 2D area distributions or fractal branching beam structures could potentially further enhance compliance and adhesion capabilities. A more comprehensive understanding of parameters involved and design options for improved performance alongside a model-based understanding could also be beneficial, and motivates work in the following chapter.

6

Extended Compliance: Designing Kirigami Patterns for Local Conformation on Rough Surfaces

This work can partially be found in "Compliance for Adhesion: Designing Kirigami Patterns for Local Conformation on Rough Surfaces" (under review).

In this section we aim to further improve the adhesion capabilities of electroadhesive pads on rough surfaces by designing compliance to increase effective contact area. We present a kirigami-based approach to enhancing compliance through an exploration of geometric features cut into an adhesive disk. We experimentally test a range of geometries, comparing shear adhesion strength to understand structure-function relationships in our chosen parameter space. Our findings indicate that introducing cuts to form serpentine paths in the disk results in longer effective lengths and enhanced compliance, thus requiring less energy to deform into a rough surface. Leveraging this insight and associated scaling analysis, we conclude that serpentine-like features arranged in a radially-symmetric wedge configuration achieve high levels of adhesion, even on rough surfaces, enabling robust adhesion relative to featureless electroadhesive disks.

6.1 Introduction

As described in Chapter 5, electroadhesion performance is generally dependent upon how closely pads achieve contact with the surface, and performance can decrease for non-flat or rough textured surfaces [57, 63, 64]. Real-world use cases for microrobots (e.g., inspection in industrial settings such as turbines or engines, manipulation of samples

or sensors, etc. [65, 66, 67]) can often include non-pristine, non-flat textured surfaces, thus motivating the desire to explore techniques for increased conformation to such rough surfaces.

Kirigami-style cuts, which introduce patterns of slits to tune the mechanical properties of a material, offer one promising approach to tuning the compliance of otherwise inextensible flat sheet materials [68]. Integrating a kirigami approach for adhesion pad designs (i.e., similar to the layer-by-layer "pop-up" techniques already used in fabrication of microrobots [8]) offers several benefits including the speed of fabrication, scalability, and the ability to use a large diversity of thin materials. Such kirigami techniques have previously been used for building a variety of robots [69, 70, 71, 72, 73, 74], for enhancing adhesion [75, 76], and for improving compliance when interacting with natural 3D surfaces [77, 78]. However, "real-world" studies often examine larger-scale robots, deformations, and curvatures rather than "microrough" (hundreds of microns) scales that may be relevant for a microrobot encountering diverse textures when operating in natural settings. This work examines several categories of kirigami-inspired designs and explores parameters that can be tuned to achieve greater local conformation to rough surfaces.

Prior research (in Chapter 5) explored the concept of local conformation by varying the geometry of electroadhesive pads [79]. This study found that a spoked design on a rough surface (75 μm height variation, 2 mm lateral feature spacing) exceeded the adhesion performance over an initial circular design, with an approximately 20% percent improved average shear adhesion stress [79]. However, it did not explore the effects of specific parameters such as spoke width and length, nor did it explore alternative geometries beyond a simple spoked design. For our current work, we sought to better understand how 2D pad shape enhances compliance and how this impacts adhesive strength, particularly for rough surfaces.

We can note that alternative options for compliance apart from 2D kirigami cut laminate structures do exist– for example, soft electroadhesives have been shown in the past to be useful for various compliant adhesion cases [80, 63], and such soft materials approaches could be considered for potential footpad designs. However, soft pads for compliance have their own drawbacks. In particular, it generally requires an elastomer (such as Polydimethylsiloxane (PDMS) or otherwise) to be used as a compliant substrate, and working with wet pour, electrode patterning, and curing processes could be nontrivial for high quality fabrication of thin compliant pads. It could be done, but using the same dry

fabrication laser layer methods already being used already for the base robot fabrication can speed the process and make overall fabrication efforts more efficient.

Even with the fabrication of such thin soft pads being possibility, practically speaking using such pads may also make less sense as footpads for an ambulatory microrobot, given robustness requirements. To get the high electroadhesion pressures needed to securely hold the robot (with some factor of safety, or perhaps with payload), the soft layers would need to be fairly thin (the comparatively robust kapton layers from the previous work being around 7.5 μm). At that level of thickness, it is likely that repeated sticking and peeling of footpads multiple times, as would be required for walking or climbing locomotion gait patterns of the robot, could cause tears. Slightly thicker soft pads for enhanced robustness could also be possible, but would then require higher electroadhesion voltages to reach similar adhesion pressures (which would increase the requirements for eventual future onboard electronics requirements as well). Thus while soft or more 3D type structures for compliance could be useful and interesting to explore in the future, we choose to further focus on and explore 2D laminate kirigami options that in the context of the microrobotic use case, may be more efficient to fabricate while being more robust for repeated robot usage.

Thus, in this chapter we focus on improvements using kirigami cut patterns, presenting an exploration of the diversity of base shapes by adjusting geometric parameters, and evaluating adhesion performance under different surface conditions.

6.2 Pad Design and Fabrication:

As before, we consider the adhesion behavior of these unipolar electroadhesive pad designs with the general behavior driven by Eq. 4.1. Considering the dielectric thickness d to potentially introduce localized air gaps reducing the actual area in contact, we aim to create compliant designs which can more closely adhere to the surface for enhanced adhesion.

6.2.1 Design Details

The 2D geometric designs considered in this chapter fall into several categories: circles, spirals, wedges, spikes, fractals, and serpentine patterns, as shown in Fig. 6.1. Several of these shapes were relatively straightforward to design given the common parameters – including length of a feature (from the center base circle of a pad to the outer edge), width

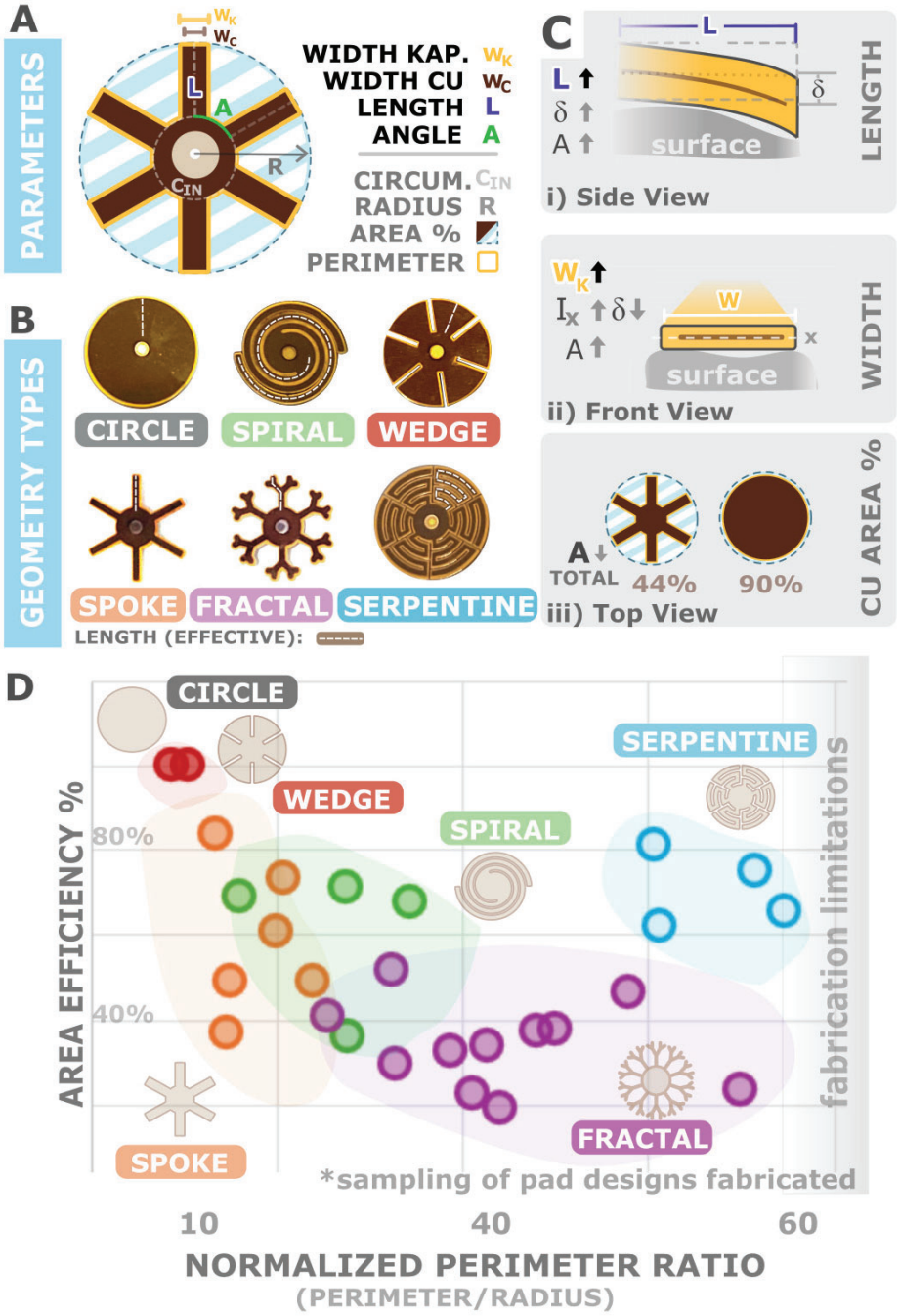


Figure 6.1: 2D electroadhesive pad designs for compliance on non-flat surfaces. A) Width, length, and angle parameters in design definitions. B) Geometry design candidates. C) Hypothesized interaction of pad design and rough surface, where increased length increases deflection δ. D) Area efficiency vs. perimeter for various pad types reflects a general trade-off between compliance complexity and area efficiency.

of an individual beam-like feature (as fabricated from kapton and copper material layers), and angle between feature patterns.

6.2.1.1 Fixed parameters

Apart from the common varying design parameters, other fixed parameters were kept the same across all designs. Such fixed parameters include the inner circle circumference. This central circular area (3 mm diameter) was included in all designs for electrical and mechanical attachment (for our experiments, attachment to a thin FR4 test fixture connector piece for load testing; for robot usage, an FR4 leg for walking). Another fixed parameter was the maximum outer radius – i.e., the overall circumscribed circular footprint radius which the design should fit within. This was chosen simply to have a standard limit for comparison, though in practice this is also physically constrained by the task or robot dimensions (e.g., robot feet should avoid stepping onto each other). This is also limited by surface constraints, as larger footpads will carry a greater chance of encountering different surface features (whether curvatures, cracks, blemishes, or other challenges that may make electroadhesion more difficult).

The width of the Kapton border surrounding each copper design was also fixed, and experimentally determined as at least 150 µm to meet the material breakdown requirements to reliably maintain the parallel plate capacitor charge distribution (i.e., given the limits of laser-based bulk micromachining and layer alignment limitations) within a reasonably factor of safety. Smaller thicknesses could work but could also lead to pads shorting and failing during trials. The brief tests in Appendix B (Fig. B.1) can serve as a reference for design limitations given the equipment used. However, future work could explore fine tuning the calibration and alignment of the laser (or using even higher precision lasers), or carefully tuning the cut settings to decrease the minimum border width.

6.2.1.2 Design-specific parameters

Some patterns required consideration of additional parameters to capture their complexity. For our **fractal** design definition, we adopted a design inspired by the conventions of a symmetric binary fractal tree [81]. The traditional definition of such a binary fractal tree includes a single initial branch, which splits into two symmetric branches of length r at some branching angle θ. It then splits again following the same θ and r^2, and

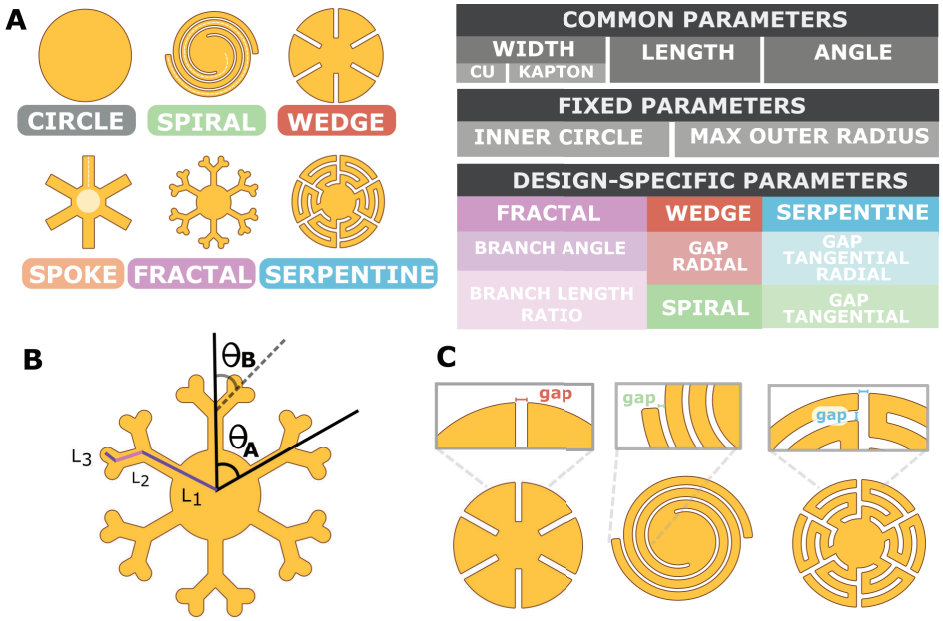


Figure 6.2: **Design details**: A) A brief review of the different design types presented with parameters (grey), and several design-type specific additional parameters in respective colors. B) Diagram of binary fractal design definition, including the branching angle, θ_B, and lengths (L_1, L_2, and L_3) which decrease outward from the center by a set branching ratio $R_B = \frac{L1}{L2}$, etc. C) A closer look at some of the additional gap parameters set in wedge, serpentine, and spiral-type shapes.

continues on indefinitely for an infinite number of branches [82, 83, 84]. Given that the goal in this work was to physically fabricate adhesive structures, a few adjustments were made to help avoid features too small to fabricate – i.e., the maximum number of 'layers' or steps of branching was selected as three, and the same ratio r was used to decrease the length at each branch (i.e., rather than squaring). By setting a θ_B for the angle between branches, initial length l_1 for the first branch, and shrinking the length of subsequent branches according to a branch length ratio R_B, we defined a symmetric branching structure, as seen in Fig 6.2. This was then revolved around in a circular pad shape according to θ_A, similar to other patterned features. In generating shapes, angles were selected such that they would not self-intersect (when accounting for the width and additional Kapton border) such that each branch could be freestanding, and calculated the branch lengths for the design based upon the desired maximum outer radius and selected branch ratio. The final fractal structures could then be *offset* such that a uniform width feature was constructed from the original line structure. By adjusting our definitions to account for the width of the branches, we

adopted the general structure and convention in a modified parameterized way that could be readily physically fabricated.

Other designs also had various other parameters to define. For example in the wedge shape, the gap distance between features, rather than the width itself, is a fixed parameter. For the wedge shape, this gap was kept to 0.4 mm throughout the study for ease of comparison. Similarly, both spirals and serpentine designs had gaps between the tangential rings of the design. While initially some larger gap designs were explored, this width was generally kept to be the minimum distance required for twice the outer kapton border, or around 0.3 mm (such that there was no excess gap between) to use the space most efficiently.

A view of some of the shapes generated can be seen in Fig. 6.3. We detail the design parameters of all successfully fabricated and tested designs from Fig 6.3 in Table B.1 (Appendix B).

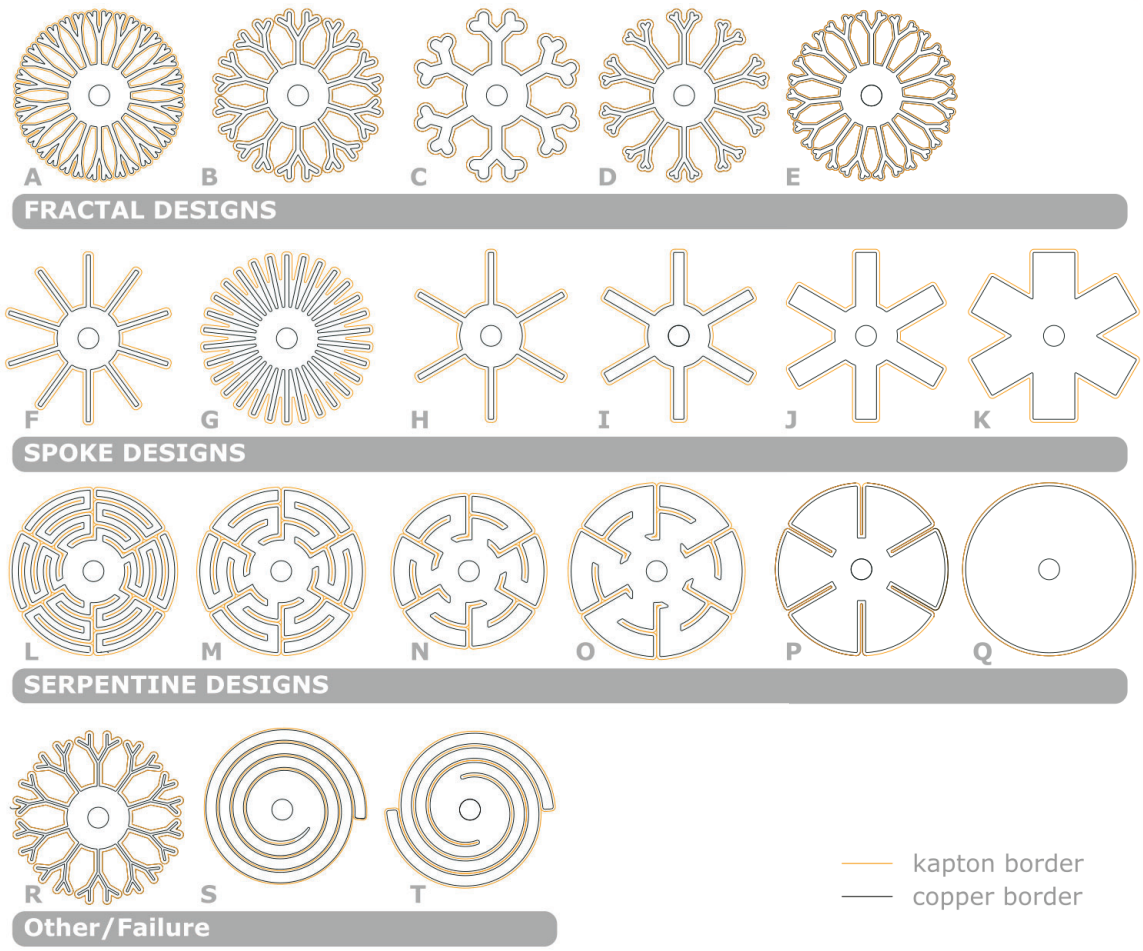


Figure 6.3: **CAD designs**: A)-E) Fractals of varying branching angle, branch length ratio, and rotational angle were generated for experimentation. A variety of spokes (F-K), serpentine (L-O), wedge (P), and circle (Q) designs are also shown. R) Thinner fractal patterns were designed but not made, with the 100μm thickness bring too thin for fabrication within the existing laser-based bulk micromachining and lamination approach used. S) Single Spiral and T) Double Spiral designs were successfully fabricated, but too easily peeled off during loading for any measurable adhesion, so were not included in shear experiments.

6.3 Fabrication

The fabrication primarily followed the lamination methods outlined in prior work [13, 79], with the slightly thinner 7.5 µm (vs. 12.5 µm) kapton and 3 µm (vs. 5µm) copper layers as shown to scale in Fig. 6.4 providing slightly stronger adhesion. In using thinner materials, additional attention was given to removing air bubbles and wrinkles from between the handling substrate (Gelpak) and the functional material (using rollers and glass slides to squeeze out any remaining air) in order to ensure the most accurate laser cuts.

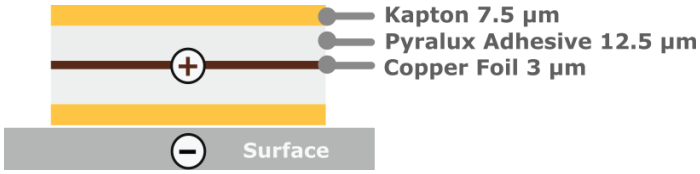


Figure 6.4: **Layer fabrication** layup of Kapton, adhesive, and copper foil materials (thickness to scale). Subsequent charges applied to the copper layer and grounded surface for use during electroadhesion testing are also indicated.

For the relatively small complex designs fabricated in this work, careful manual microscope-assisted removal of the outer excess unwanted copper foil was needed to leave the desired patterns in place on the Gelpak without moving or misaligning pieces. For an example of what could happen when excess foil was directly pulled off, see Fig. 6.6A. To avoid this, excess copper was removed as shown in Fig. 6.5B, gently poking at excess copper with a pair of fine-tipped tweezers, which led to the excess shapes curling away from the Gelpak. Once curled away and free from potential of entanglement with desired copper shapes, the excess copper could then be removed from the Gelpak. Future efforts could consider further tuning the cut settings to release the copper more easily (without burning too far into the trace itself). Future cut settings could also examine rastering away unwanted copper (either fully rastering to remove all unwanted copper, albeit potentially at the cost of extended laser cutting time, or partially rastering away a larger border from the desired designs such that any outer excess could be rapidly peeled away). A stronger adhesive Gelpak could also be used to help keep designs securely in place; in this work we use a very lightly tacky Gelpak x0 and could explore Gelpak x4 and x8 options which increase the sticking adhesion to materials. However, this comes with the limitation that it may lead to increased delamination potential during back-tack steps, as it must be removed before full layup.



Figure 6.5: **Manufacturing process** using a high resolution laser cutter, heat press, and alignment jigs to create a multilayer laminate.

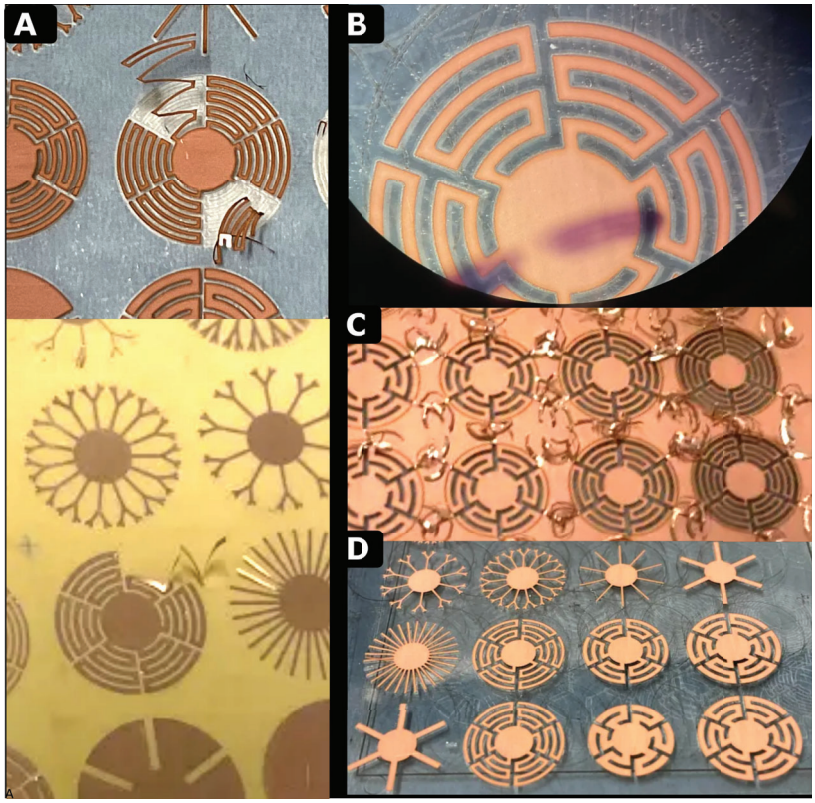


Figure 6.6: **Copper removal closeup.** A) Detachment and pulling of finely patterned copper geometries could occur, both in the original laser cutting step and during the Gelpak removal step after the first back tack. B) To avoid undesired peeling, shapes were examined under a microscope for manual removal of unwanted material. C) By poking at the excess copper foil, due to the thin nature of the material layer, unwanted parts peeled away. D) The excess copper could then be removed all at once, leaving behind the desired pad shapes on the lightly adhesive Gelpak substrate.

Alternatives to the laminate method for patterning of copper could also be considered in the future. For example, photolithography techniques could enable the patterning of etched copper with similar precision. However, because designs include not just patterned copper but also the aligned release kirigami cuts for Kapton that allows for actual pad bending, laser methods will likely still be required at some stage of the process.

6.4 Experimental Electroadhesive Evaluation:

6.4.1 Methods: Surface Fabrication and Experimental Setup

Pseudo-random surfaces were designed using a fractal Brownian motion (fBm) pattern technique [58] which utilizes two surface "roughness" spatial parameters: h the relative height between vertical peak and trough features, and s the relative horizontal spacing between features. We generate all terrains with Hurst parameter H = 0.1 (for qualitatively more "pitted" correlations between adjacent features). The randomly defined surfaces were generated using MATLAB, 3D printed (Objet30 Polyjet, 30 μm resolution, VeroWhite), and sputter coated (Denton Vacuum, Cu, 4 min, 300 mA, approx. 0.2-0.3 μm coating). Three progressively rougher surfaces were created using the above procedure with feature spacing, s, set to 2mm, 1mm, and 0.3mm, respectively. The height feature, $h = 75\mu$m, was the same for all designs, as shown in Fig 6.7A, in order to allow for comparison across results.

In the experimental setup [79], individual pads were electroadhesively engaged onto a surface by carefully placing a small (1 g) weight on top to bring them into initial contact with the surface. A voltage of 750 V was then applied and the weight was removed. Given the border thickness selected, 750 V was the maximum voltage we could test up to and avoid shorting. To quantify the electroadhesion performance in the shear mode, the pad is slowly pulled in the lateral direction by a stepper motor driving a linear stage (0.2 mm/sec) in series with a spring to exert a gradually increasing shear force. Trials were run until the pad slipped, with a force-torque sensor (ATI Nano-17) mounted to the bottom of the surface collecting shear force data at 1000 Hz.

6.4.2 Parameter Study

An evaluation of the adhesion performance for the chosen pad geometries on the three surfaces was conducted, as seen in Fig 6.7B. From initial tests on Surface 1, we identified promising pad design categories. We then narrowed down the types of pads for further testing on increasingly rougher surfaces to focus on those designs with clearer differences in geometry and performance while avoiding designs more prone to failure. For example, spiral designs exhibited high initial adhesion but failed at relatively low shear forces on all surfaces, and so were eliminated from further studies. Thus we narrowed from

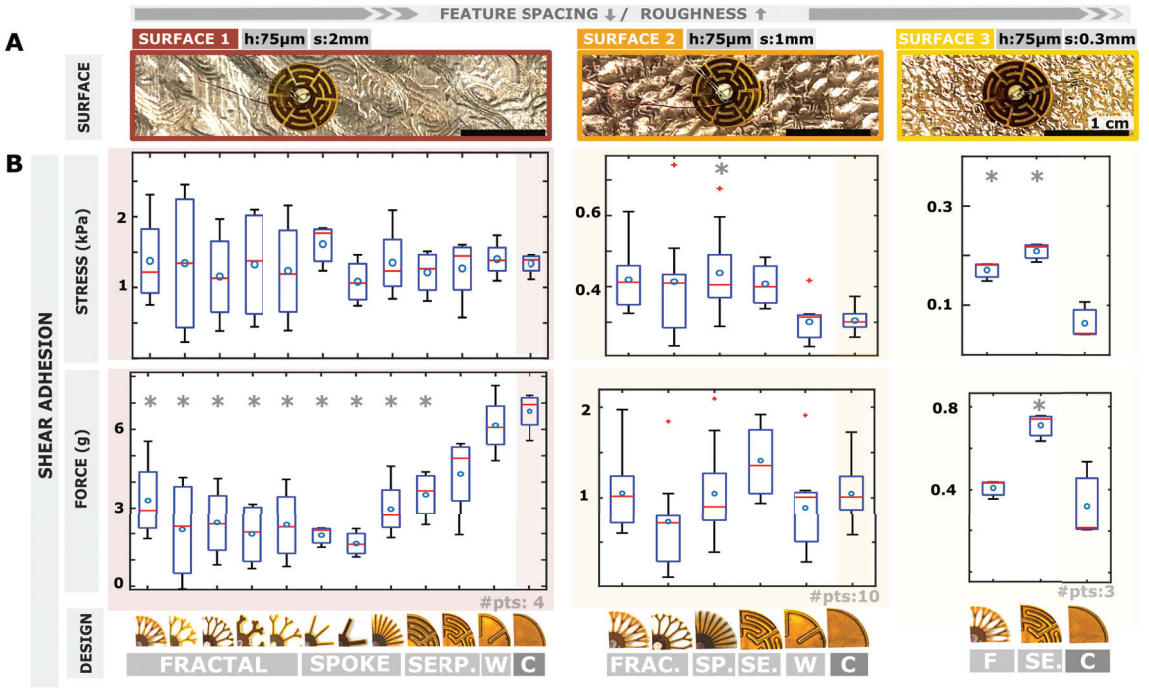


Figure 6.7: Shear adhesion tests for all considered pad geometry types on different roughness surfaces. A) Surfaces of increasing roughness (e.g., decreasing feature spacing), with the serpentine electroadhesive pad design for scale comparison. B) Shear adhesion performance reported both as stress (force normalized to the copper area) and force (grams). Boxplots show the interquartile ranges, the max and min points as whiskers, the red bars are the medians, the blue circles are the means, with red crosses for outliers (>1.5 times away from the median). Test results which were statistically significant from the circular baseline shape (highlighted on the right of each data set) according to a one-way ANOVA test are denoted with a grey asterisk (*).

twelve (surface 1) to six (surface 2) to three pad designs (surface 3) based on analyses of adhesion performance as roughness is increased.

In general, overall pad performance tended to decrease on rougher surfaces. For example, average shear forces for the baseline circular shape decreased with progressively rougher surfaces from 6.7 ± 0.8 g (surface 1), to 1.1 ± 0.3 g (surface 2), to 0.3 ± 0.2 g (surface 3). The circular design also comparatively decreased the most in performance on rougher surfaces, with an approximately 95 % drop in performance from surface 1 to surface 3. While a circle was the best performing pad type on surface 1, it was among the worst performing designs on the rougher surfaces (Figure 6.8). Despite overall lower forces, differences in adhesion stress between designs could be more prominent on rougher surfaces. For example on surface 1, a 0.5 mm width serpentine shape (1.3 ± 0.5 kPa) did not exhibit a statistically significant difference relative to the circular pad performance ($1.3 \pm$ 0.2 kPa). However, on surface 3 there was a statistically significant difference (0.2 ± 0.02 kPa compared to $0.060 \pm$ 0.040 kPa).

We observed that fractal shapes could adhere well occasionally, but could also interact with surface features at angles that prevent entire sides of the pad from adhering, leading to greater variability (see Fig. B.2 in Appendix B for attachment visuals). For example, the second fractal shape had 1.3 ± 1 kPa shear stress performance on surface 1, with the maximum of 2.5 kPa being one of the highest of the batch, but also with one of the largest variations. This category of designs also had relatively lower absolute adhesion force magnitudes (2.3 $g \pm 1.8$ g for the same fractal) due to their inefficient space usage.

Spoke and serpentine designs seemed to perform reasonably well on rougher surfaces 2 and 3 as shown in Fig. 6.7B. For example, on surface 2 the shear stress of both spokes (0.5 ± 0.2 kPa) and serpentine designs (0.4 ± 0.1 kPa) appeared slightly higher when compared against a circular pad (0.2 ± 0.07 kPa), with these trends even more apparent and statistically significant on surface 3.

Finally, we also performed some comparative analysis of the different pad types on different surfaces to better understand how much performance degrades on surfaces of increasing roughness, as shown in Fig. 6.8. These comparisons were generated using the same data as Fig. 6.7. We observe that while the circular pad has the greatest absolute force and stress performance on flat surfaces, it also experiences the greatest drop-off in performance as the surfaces become rougher (with features more tightly spaced). We also observe that the fractal pattern experiences some of the least drop-off in performance,

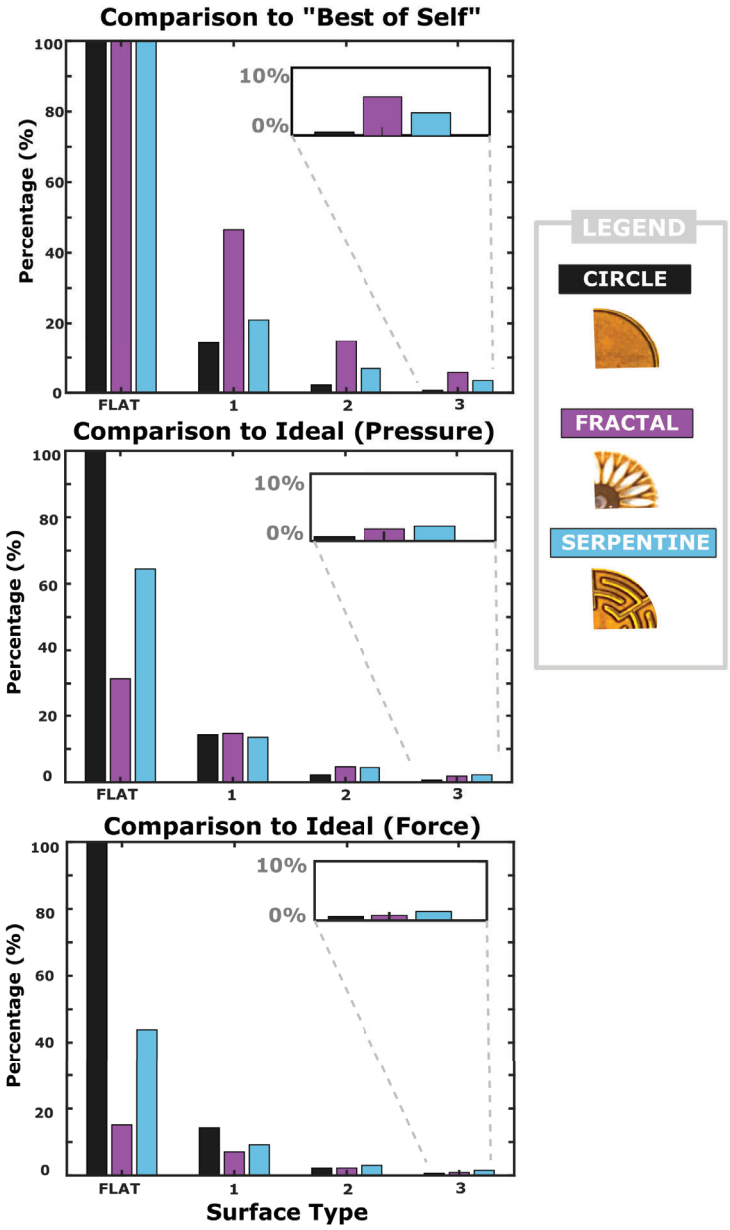


Figure 6.8: **Comparative performance and relative drop-off of adhesion strength.** Comparison of performance relative to best performing pad types/flat ground baseline. We can see that fractals retain the most adhesion when moving from a flat surface to a progressively rougher surface, while serpentine shapes retain better performance compared to a baseline 'ideal' case (circular pad on a flat surface). The decrease in overall performance on surfaces of greater roughness (as defined by closer spacing of features) is also apparent.

however it did not have as strong of a performance to begin with. Thus we observe also that the serpentine shape has the best overall performance on rougher surfaces (less of a drop-off compared to an absolute ideal case), and thus seems better equipped for adhesion on rougher surfaces.

These findings generally align with our initial hypotheses that designs which allow for greater compliance could enhance the adhesion capabilities of electroadhesive pads. We hypothesize that understanding the behavior of the simplest cantilever-based spoke category could provide us with insights applicable to other shapes, and first focus on the spoke shape for further analysis.

6.4.3 Spoke Geometry Analysis

To approximate the ability for spoke features to deflect, and thus more closely conform locally to a surface, we consider a beam-bending model for maximum deflection of a fixed-free cantilever beam under uniformly distributed loading:

$$\delta_{max} = \frac{Pl^4}{8EI_x} \tag{6.1}$$

where P is the pressure per unit length (F_{adh}/l), l is the length (i.e., spoke length), E is the modulus of elasticity, and I is the moment of inertia for the beam, where $I_x = (wt^3)/12$ for beam width w and thickness t. Given this simple model, we anticipate that increased spoke length will result in increased beam deflection (for a fixed pressure) and thus should allow for a reduced dielectric gap d and improved adhesion.

Given this model, we may anticipate that increasing spoke width will increase both the area moment of inertia (decreasing compliance) and the local feature area (increasing adhesion force), such that these two effects would cancel and therefore cause a negligible effect on adhesion force. However, we also note that there are constraints on spoke width. Specifically, fixed (i.e., scale-invariant) dielectric border width decreases the effective space efficiency for designs with larger perimeters. Similarly, the central hub and repeated radial pattern for all designs imposes a tradeoff between effective width and effective beam length. Furthermore, process-dependent fabrication constraints limit the ranges of lengths and widths possible to explore.

For example, we note the previously mentioned minimum 150 μm border becomes

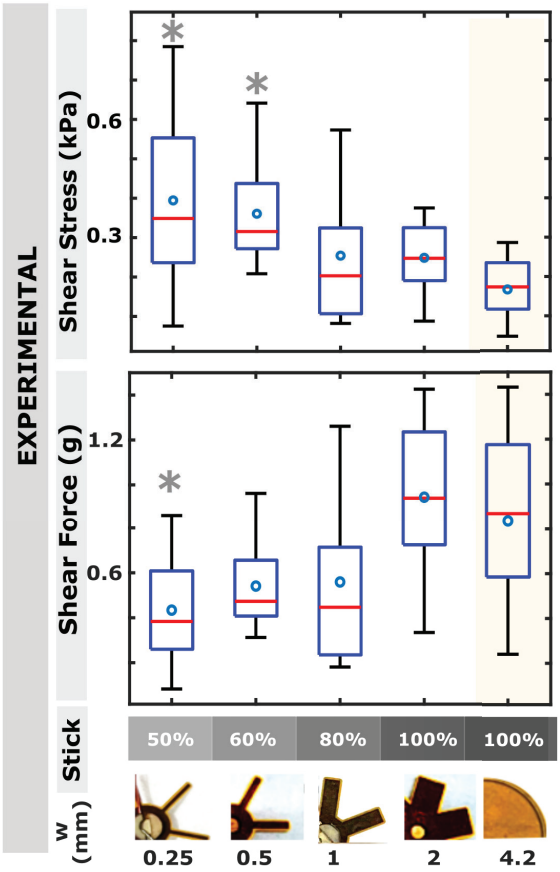


Figure 6.9: Spoke design with varying widths on surface 2. Experimental shear adhesion performance (expressed as both stress and force) of spokes with widths ranging 0.25-2 *mm* (plus circular baseline), with 15 data points each. Grey asterisks (*) denote statistical significance determined by a one-way ANOVA test. Successful stick percentage is also reported – from a separate test of ten trials, defined as the number of trials which adhered to the surface vs. detached completely before load could be applied.

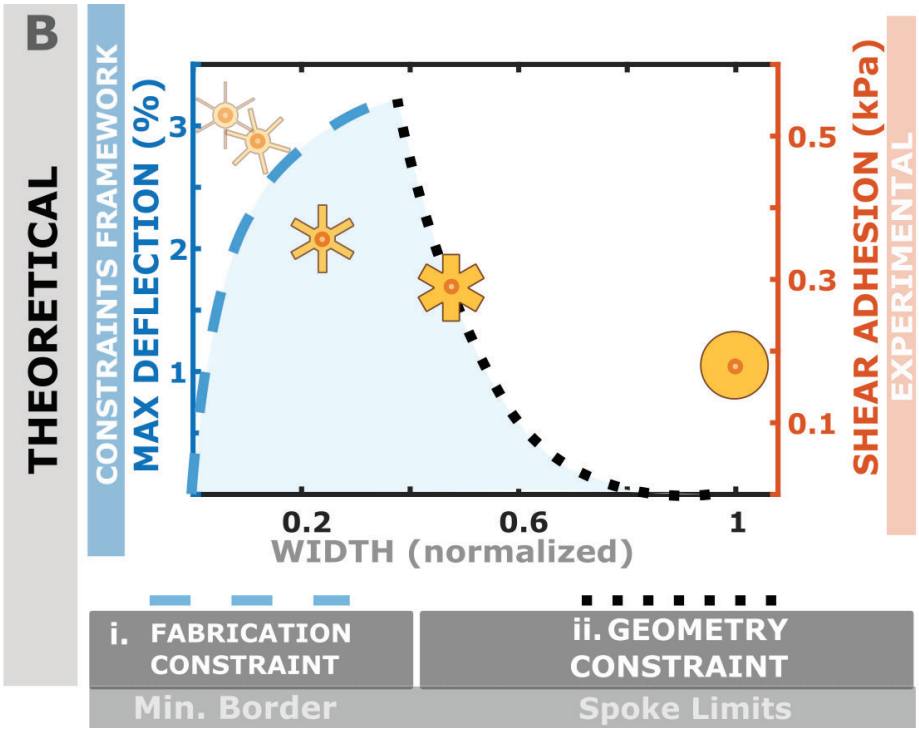


Figure 6.10: Spoke design with varying widths on surface 2. Theoretical framework of predicted compliance (blue) considering limitations due to fabrication (dashed (i)) based on Eq. 6.2 and geometric (dotted (ii)) based on Eq. 6.3 constraints. We approximate the maximum displacement of a spoked design based on Eq. (6.1) using an approximation of a fixed amount of electroadhesive force (Eq. 4.1) distributed over the piece, with changing width and several fixed parameters ($N_{spokes} = 6$, $C_{inner} = 3\ mm$). Experimental means plotted on top (orange).

increasingly relevant for smaller feature sizes. The width of a spoke can be split into two components:

$$w_{structural} = w_c + 2w_k \tag{6.2}$$

where w_c is the copper width and w_k is the kapton border width. When calculating the electroadhesive forces, we only include the active conductive copper area w_{cu}. As w_{cu} shrinks, the fixed border term dominates the width and thus substantially impacts the beam stiffness. For very thin features, in this case around the same relative scale of the 150 μm border or lower, we hypothesize that performance will decrease with shrinking width due to border constraints, as shown by the fabrication constraints in Fig. 6.10.

There are also geometry constraints for the pad (Fig. 6.10). Considering a spoke design with a fixed number of spokes, the maximum width possible for a spoke without

changing the length is constrained by both the overall circumscribed circular footprint and the minimum inner "hub" circle allocated for mechanical and electrical attachment. We anticipate that increasing the ratio of active to border width will improve performance up until the point at which increasing the width starts to self-intersect, causing a reduction in the effective length of the spoke features. For a reasonably large number of spokes, this geometric self-intersection constraint could be approximated as:

$$N_{spokes} \times w_{max} \leq C_{inner} \tag{6.3}$$

where N_{spokes} is the number of spokes, w_{max} is the maximum width for a spoke before otherwise shrinking the effective spoke length, and C_{inner} is the circumference of the inner circle. Beyond this limit, as the spoke length shrinks this is equivalent to growing the central circular attachment plate, in the limit approaching the baseline circular pad design. The maximum deflection for a circular plate under uniform loading is given as follows:

$$\delta = \frac{Pr^4(5+\nu)}{64D(1+\nu)} \tag{6.4}$$

where r is the radius of the disk, ν is the Poisson's ratio of the disk material, and $D = \frac{Et^3}{12(1-\nu^2)}$ is the flexural rigidity of the plate (with E the modulus of elasticity, and t thickness). Note that this is for a uniform load on a circular disk simply supported along the edge [85], but we assume similar scaling and approximate magnitude of deflections for centrally supported or edge supported cases.

Focusing on trends in the width parameter, an experimental sweep of different widths for a spoke geometry was performed, as seen in Fig. 6.9. We find that the experimental results support the hypothesized effects of the geometric constraints discussed above. Specifically, the 2 mm spoke design appears to perform slightly better in stress (0.25 ± 0.09 kPa) compared with a baseline circle (0.17 ± 0.7 kPa), although it was not statistically significant. We find that for smaller widths, decreasing spoke width results in decreased force performance (0.53 ± 0.24 g) compared with a circle. This lower force performance makes sense given both the fabrication constraints and the smaller area. When normalized to consider active area and only pad trials which successfully adhere, smaller width designs demonstrated increased shear stress (for the smallest 0.25 mm pad, 0.4 ± 0.2 kPa), albeit with a relatively large range (i.e., $0.08 - 0.8$ kPa). We also investigated adhesion

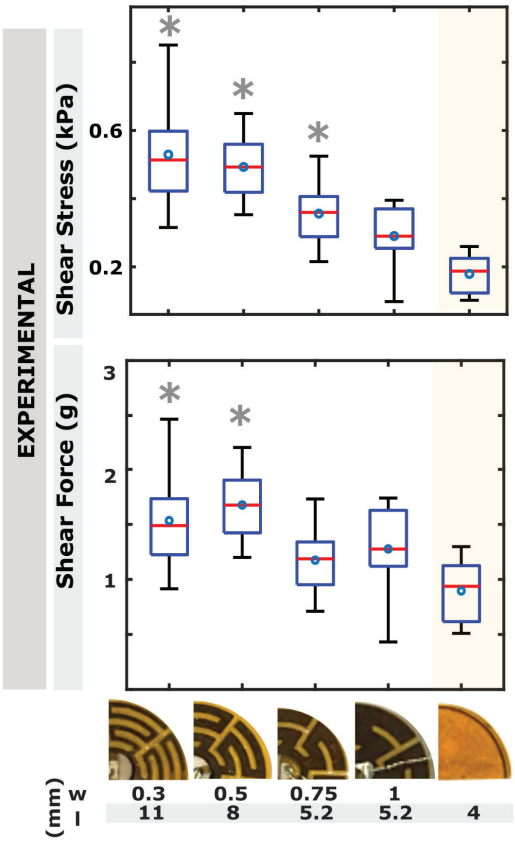


Figure 6.11: Serpentine design performance on surface 2; designs vary both width and length, with eight data points each. All pads exceeded a minimum threshold adhesion, so adhesion success was not evaluated. Increasing the length of a single feature appears to lead to higher forces and stresses. Grey asterisks (*) denote statistical significance determined by one-way ANOVA test.

success rates, defined as the number of trials where the pad actually adhered and a shear force data measurement could be taken normalized to the number of trials. We find that 50% the time the thinnest spoke designs do not adhere at all compared to a 100% adhesion rate for designs with larger widths. Thus while it appears that thinner widths can improve shear adhesion stress, the results are more variable. We hypothesize that this is due in part to interactions with features on the randomized surface, and whether it can meet the minimum electroadhesive force generated required to adhere.

6.4.4 Serpentine Pad Analysis

After finding that serpentine designs appeared to have some of the strongest shear adhesion forces, particularly on rougher surfaces with more closely spaced features (Fig. 6.7B), we further sought to explore the serpentine parameter space. The serpentine designs utilize the circumscribed area better than spokes or fractals, thus holding potential to increase adhesion force for a given area. The serpentine shapes also incorporate a beam-like geometry similar to spokes, thus we anticipate increased compliance resulting in similarly improved adhesion stress as well. We further hypothesized that longer lengths of an individual serpentine feature could translate to greater beam deflection and thus the ability to conform to rough surfaces, improving adhesion stress. Given the overall area constraints (4 mm outter radius), increasing serpentine length is associated with a commensurate decrease in beam width. Despite multiple parameters changing simultaneously, on the basis of Eq. (6.1) we thus anticipate the length term to dominate over width effects.

From experimental trials shown in Fig 6.11, performance increased with increasing length (and thus decreasing beam width) for serpentine shapes, lending support to our hypothesis that longer lengths may achieve greater deflection to maximize contact and better adhere locally. The longest design, with an 11 mm effective length, aachieved an average shear force of 1.53 ± 1.48 g and a stress of 0.52 ± 0.17 kPa. This stress performance was approximately three times that of the baseline circle, a significant difference. The border performance drop-off seen with spokes might have also occurred at lower widths (given the points tested, we do see a slight variability increase with the thinnest design), but due to fabrication constratints, 0.3 mm widths were the thinnest features tested in this study. The 0.5 mm pad demonstrates the highest average force, reaching 1.68 ± 0.33 g or roughly 1.7 times the force output of the best-performing spoke design and 1.9 times the force output of the circular pad.

6.5 Conclusions

In this chapter we explored a variety of cut patterns for small-scale kirigami-inspired electroadhesive pads. We present a framework for understanding width and length parameters and apply this analysis to several classes of pad geometries. Leveraging laminate-based microfabrication methods we construct and experimentally evaluate multiple in-

stances of these designs. We observed that on smooth surfaces with more spaced out features, circular shapes tended to have the greatest adhesion forces, while adhesion stresses are similar across all design types. On rougher surfaces with more tightly packed features, we observed clearer distinctions in behavior, with improved performance of more compliant serpentine designs over circular designs. From a closer look at width parameter effects on a spoked design, we hypothesized there may be limitations imposed by fabrication constraints on border width. We present evidence of increasing shear force with increasing width supporting this hypothesis, up to a point where geometric constraints begin to limit the effective spoke length. We further found evidence of increasing performance with increasing feature length for a serpentine design, with the 0.3 mm width design achieving on average three times the shear adhesion stress compared to a circular design on rough 75 μm height terrains with relatively close (1 mm) feature packing. Thus by considering the fabrication and geometric constraints that bound the design space while striving to increase compliance, we are able to design geometries for enhanced adhesion on rougher terrains.

Future work could explore more expansive design parameters, more detailed theoretical models, or more complex environmental conditions (considering humidity, temperature, surface lubrication, or biofouling), with more varied operation modes (e.g., normal or peel adhesion as detachment options). Extended robotics efforts could also examine adding sensors for adhesion detection to better take advantage of designs with stronger stress performance but lower adhesion reliability. All pad designs included in this study, with the exception of the less compliant wedge and circle shapes, aimed to fill space with designs that roughly had a singular rectangular beam cross-section as the basis, repeated and rotated at intervals, as opposed to more irregular kirigami shapes. However, alternative kirigami techniques (for example, those made with parallel-cut or cross-cut patterns [68], or that may also feature out-of-plane buckling, rotating units, and other similar properties [77]) could be interesting to explore in future studies.

While differing environmental conditions may impact performance, we envision the overall behaviors of beam-based kirigami designs explored here to be translatable to other scenarios facing tradeoffs of adhesion and enhanced compliance for local conformation to small-scale rough surfaces.

7

"Real-World" Electroadhesion Demonstrations and Applications

7.1 Adhesion on Industrial Rough Surfaces

While our efforts thus far have primarily characterized, tested, and demonstrated the capabilities of a robot on lab generated terrains using 3D printing and sputter coating technology, we also believe that considerations for successful attachment on rougher terrain are important for robotics and real-world applications. We therefore examine the capability for electroadhesive pads and robots to adhere on more real world terrains and environments, and here demonstrate adhesion using the explored pad geometries on actual surfaces.

7.1.1 Robot with Spoked EA Pad Inclined Climbing on Aluminum Tooling Plate and Tools

We first demonstrate the ability for the robot with spoked pads to climb on various real surfaces that may be found in an industrial inspection situation. As shown in Fig. 7.1A, the robot can climb an aluminum tooling plate with some roughness and scratches from wear, as well as holes. The robot is also able to climb up tools themselves, with inclined climbing on a set of two wrenches.

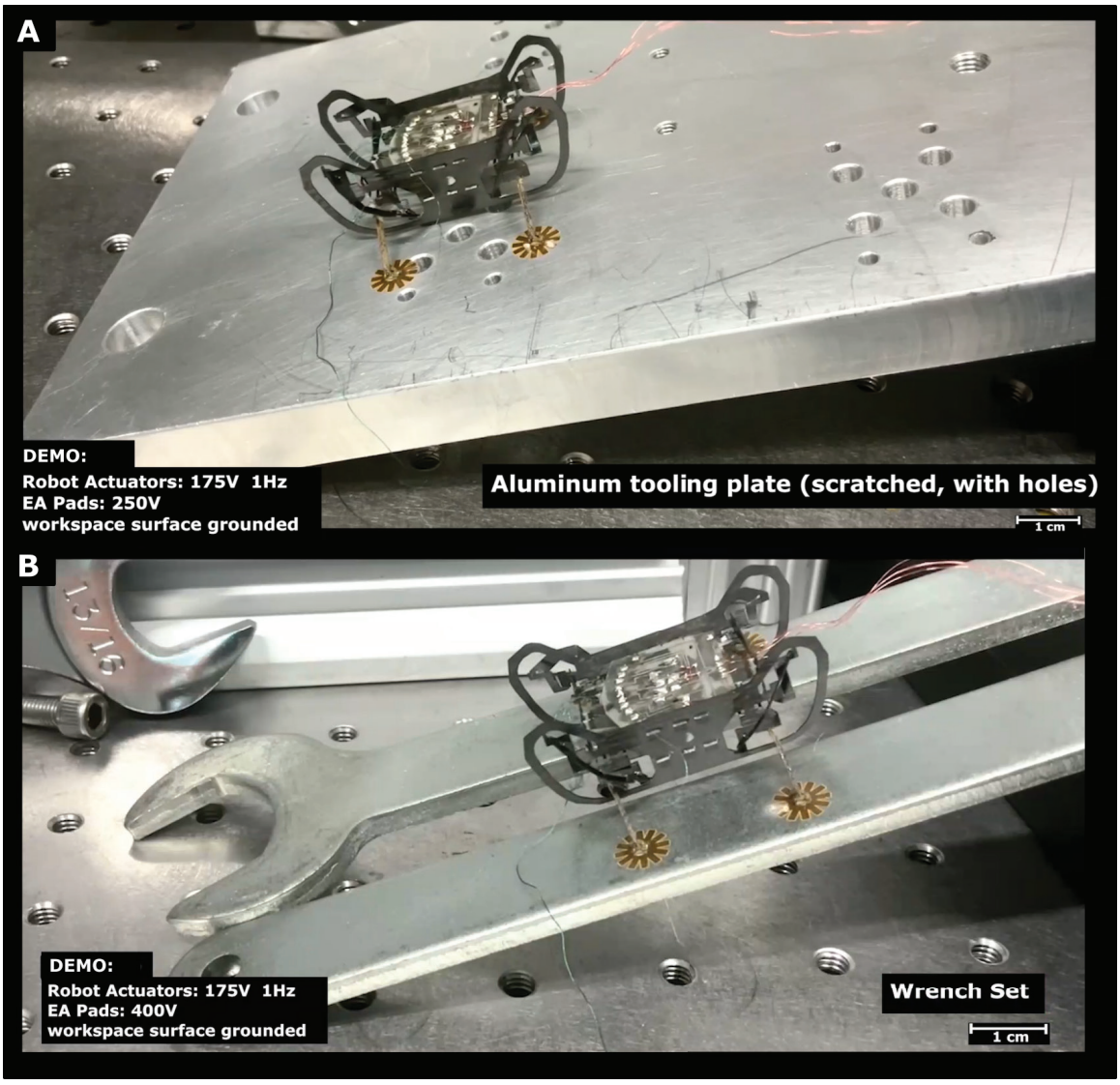


Figure 7.1: Demonstration of robot with spoked EA pads climbing in industrial environments at 500V. A) The robot climbs on an aluminum tooling plate. B) The robot climbs on a set of two wrenches. These surfaces and items are conductive and grounded through their contact with the bottom conductive grounded working surface.

7.1.2 Serpentine EA Pad Design Conforming to Large Curvatures on Automobile Transmission

We also integrate the more compliant serpentine pad types with a legged microrobot to more effectively engage with with the environment around it. By integrating the best-performing serpentine design as the robot feet, electroadhesive pads can be used to achieve local conformation even to irregular and rough shapes that may have convex or concave curvatures and crevasses that a large non-compliant pad may struggle to adhere to (Fig. 7.2). An example of this can be seen with standard circular pad design shown in Fig. 7.2(D), in which the pad manages to readjust itself when electroadhesion is turned on (E), but cannot fully wrap around the car transmission feature very well. In comparison, Fig. 7.2(B) shows a serpentine pad, which in (C) is able to more closely wrap around and conform to the feature for electroadhesion when voltage is turned on.

7.1.3 Robot with Serpentine EA Pad Design Conforming to Rough Textured Curvatures on Automobile Break Caliper

These designs can also improve robot locomotion on other rougher surfaces, including climbing capabilities on steep inclines or potentially inverted surfaces. For example, our demonstration highlights the pad's ability to conform to rough textured and curved surfaces of internal car components, which could be useful for inspection routines and tasks (Fig. 7.3). Thus we can find that the compliant serpentine pads can aid in locomotion and traversal across uneven rough surfaces and curvatures that may be encountered in real world inspection or maintenance tasks.

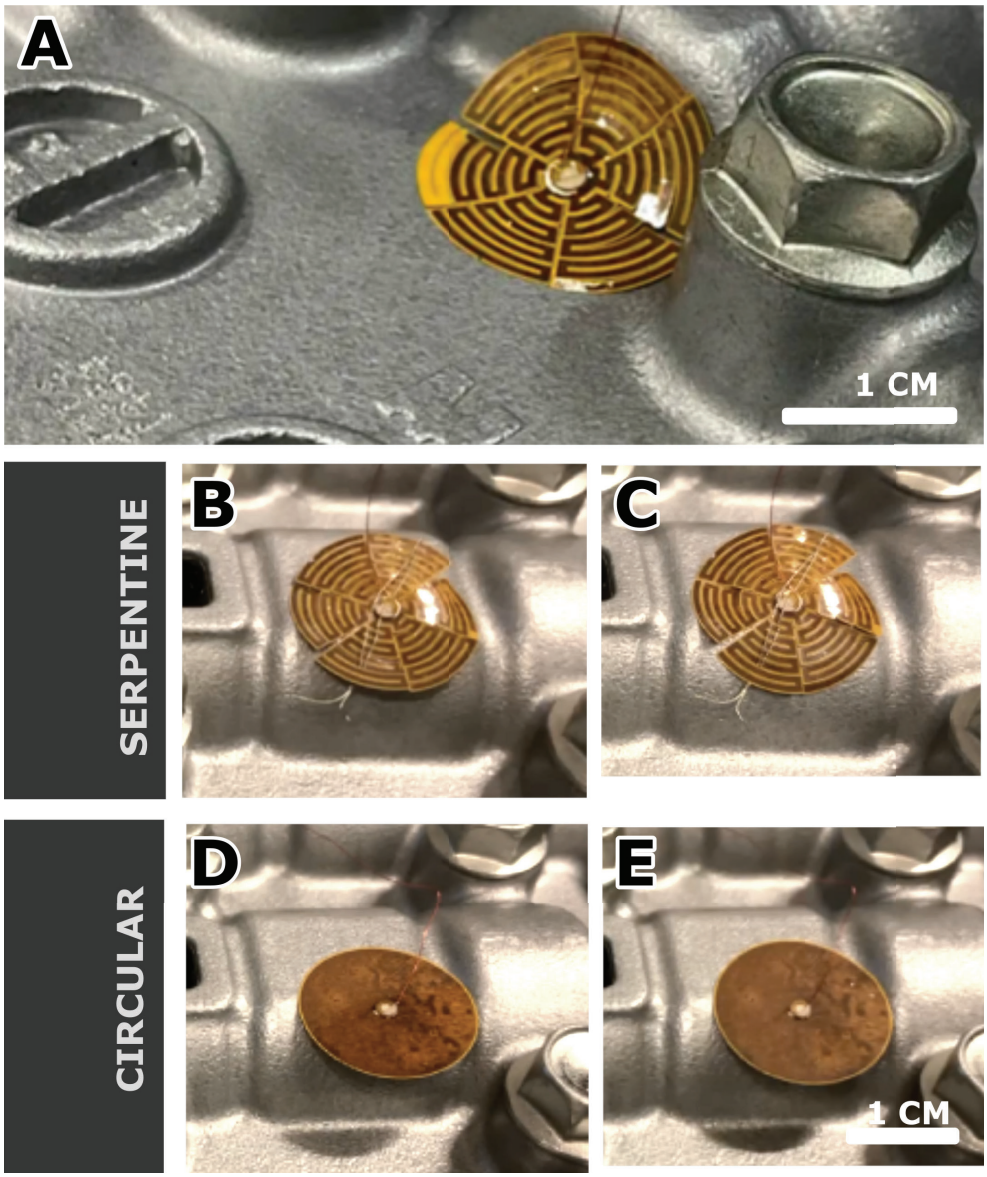


Figure 7.2: Demonstration of how designs with increased compliance can improve the ability of electroadhesive pads to adhere to irregular real world surfaces. Example of how a scaled-up (1.6 cm diamater) compliant serpentine pad design engaged at 500V can enable closer adhesion to a non-flat component for inspection (grounded automobile transmission surface: *"CVT Transmission Valve Body Compatible with Nissan Altima Pathfinder Murano Infinity"*). A) Concave surface: the pad is able to adhere into corner-like spaces. B) Serpentine design adheres to a convex rounded part, which conforms to the piece in C) when voltage is turned on. D) Circular design for comparison adheres to a convex rounded part, which is not able to conform as well to the piece in E) when voltage is turned on.

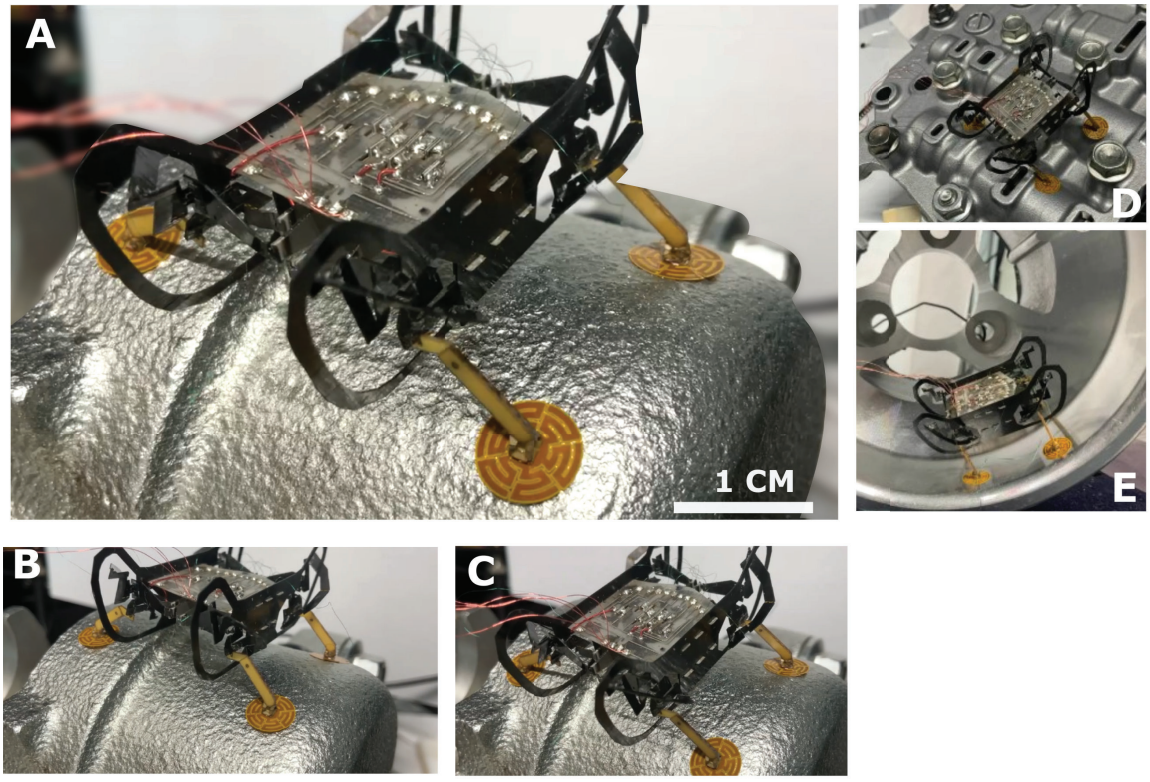


Figure 7.3: Demonstration of how compliant pad designs can improve the ability of electroadhesive pads to adhere to irregular real world surfaces. A) Demonstration of robot locomotion on a rough, curved, textured, industrial grounded surface (automobile brake caliper). B) Initial locomotion and C) continued locomotion on the curved, rough surface. D) Robot on the automobile transmission valve part shown in Fig. 7.2. E) Robot on a curved aluminum wheel rim.

7.2 Gripping and Object Manipulation

The compliant designs explored in this work could also be integrated into grippers or other manipulation devices for small scale robotic applications attempting to grasp irregular or textured objects.

7.2.1 Prior Work: Piezoelectric Grippers

The work we have shown here thus far has focused on the robotic platform itself and its capability to achieve locomotion on challenging surfaces - though as we seek to improve the eventual usefulness of microrobotics in the field, the ability to manipulate and interact with an environment is beneficial. Manipulation for small scale microrobots is an area which could vastly expand the capabilities of these small robotic devices beyond just locomotion. Such manipulation capabilities could someday enable a robot to even better navigate a diverse landscape, for example by moving obstacles, operating switches, angling itself to approach different surfaces and transitions more effectively, and/or by changing the environment around itself via construction efforts. Such manipulation capabilities could also be used to investigate items around it, for instance probing items for inspection or retrieving small found items for analysis.

We have previously worked on developing microrobot manipulation capabilities through the implementation of piezoelectric-driven grippers for the robot, which allowed manipulation of payloads up to 2.8g [86]. The gripper itself could hold 4.1g; in excess of robot payload capabilities. The gripper integrated robot was able to move small payloads around while walking and demonstrate drop-off capabilities for such materials.

However while the gripper itself was very strong and lightweight, in tandem with the robot it was difficult to operate effectively without precise controls; aligning the robot such that the tiny gripper jaws could grab an object using solely open loop commands was challenging. The maximum free deflection of the gripper was 268 μm (when operating at 200V), and could hold objects ranging in thickness 100-368 μm [86]. In the grasping task shown in Fig. 7.4 for example, objects had to be manually placed and multiple attempts made for successful grasping. Larger objects (such as those used in drop off demonstrations) also required specifically designed attachment points to grasp. To be used effectively beyond simple demonstration would require integration with more complex control. For example, grasp sensing could allow for the robot to determine whether it may need to realign itself

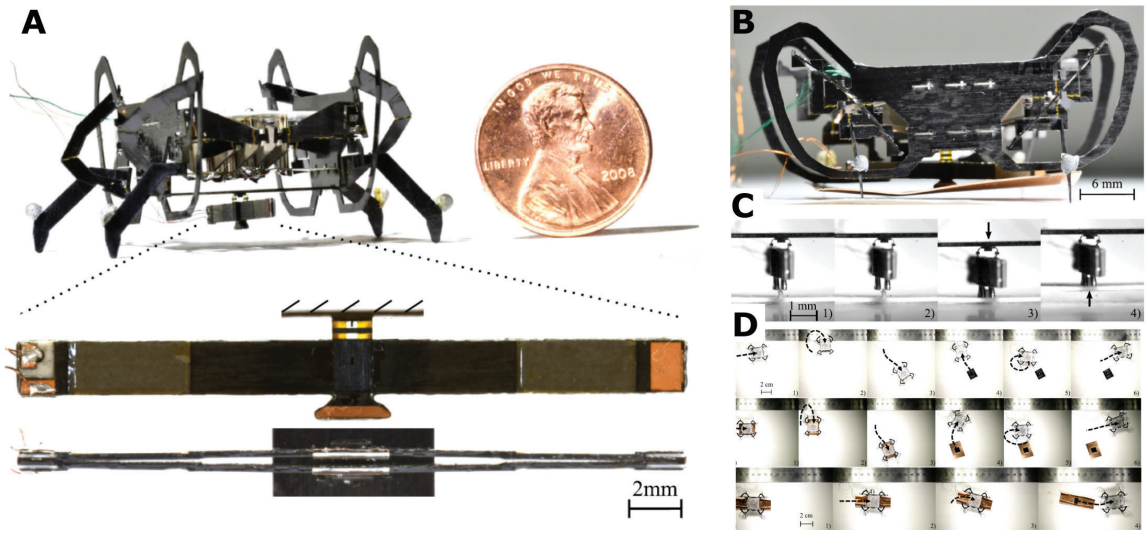


Figure 7.4: HAMR piezoelectric gripper [86]. A) The HAMR-VI based robot with gripper mounted beneath the robot. The sideview and bottom view of the gripper is also shown. B) The robot carrying a payload. C) The gripping process, which must position directly above a small handle on the material to grasp and pull the material up. D) Examples of the robot carrying a material payload for drop-off.

or shift its position to be able to grab an object. A thoughtful consideration of the types of objects that would make sense to manipulate or further design work to extend the deflection capabilities may be beneficial for extension of this work.

7.2.2 Future Potential Work: Electroadhesive Grippers for Micromanipulation

In comparison to such options, the electroadhesive elements presented this thesis could provide a more robust and readily adaptable means for gripping capabilities in the real world. Because the adhesion can 'zip' itself in to an otherwise less ideal attachment as long as it has made enough contact to start attaching, with this adaptive capability even moreso apparent with the new compliant designs outlined in prior chapters, this can allow for manipulation with less precise control or targeting. Because electroadhesion is conducted on a surface or item to pull surfaces together rather than trying to fit objects within specific limits of a fixed compression or grasping zone, this allows a wider variety of surface structures to potentially be manipulated (e.g., a large piece of material extending beyond the grasping workspace).

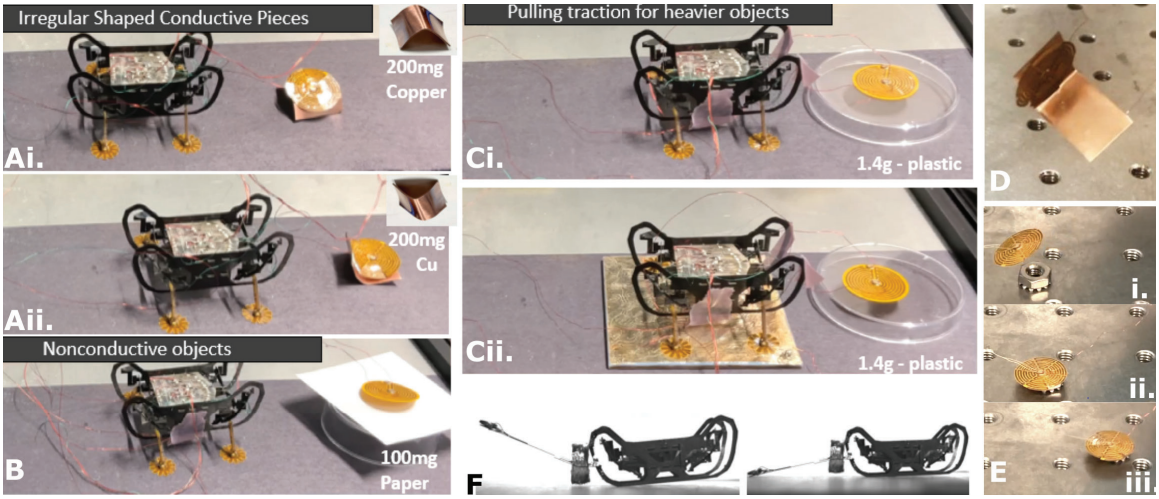


Figure 7.5: Potential HAMR electroadhesive gripping opportunities. A) Manipulation of irregular, (i) convex, and (ii) concave, copper pieces with a serpentine unipolar pad. B) Manipulation of more common household items like paper (using a nonconductive (bipolar) design with standard non-compliant circular geometry just for demonstration). C) Pulling a heavy payload can cause slipping (i), with the potential for locomotion electroadhesion to provide pulling traction (ii). D) Vertical lift manipulation of a grounded item. E) Pulling hardware across a grounded surface. F) Active tail mechanism for potential future integration for gripping.

7.2.2.1 Electrostatic manipulation examples

We can consider a few potential examples of what a robot with electroadhesion implemented for manipulation could accomplish in Fig. 7.5. In (A) through (C) the robot has an electroadhesive pad attached via wire to follow behind the robot in a passive tail manner. For example, in (A) a compliant serpentine pad could potentially be be used to attach to irregular/bent/non-flat items. In (B) we demonstrate that nonconductive electroadhesive pad designs (which employ a bipolar high voltage and ground design) could be used to manipulate more common household items like paper – albeit further work would be needed to explore how compliance could be added to such designs. (C)i. A robot seeking to pull a heavy payload may slip in place with the prior foot design when trying to pull a heavy object, but with electroadhesion used for both manipulation and locomotion in tandem (C)ii, electroadhesion could provide the foot adhesion traction necessary to pull forward with higher payload items. (D) Demonstrates vertical lifting capability for a light (300 mg) copper grounded object, while (E) demonstrates pulling of a piece of hardware (locknut) on a grounded industrial surface.

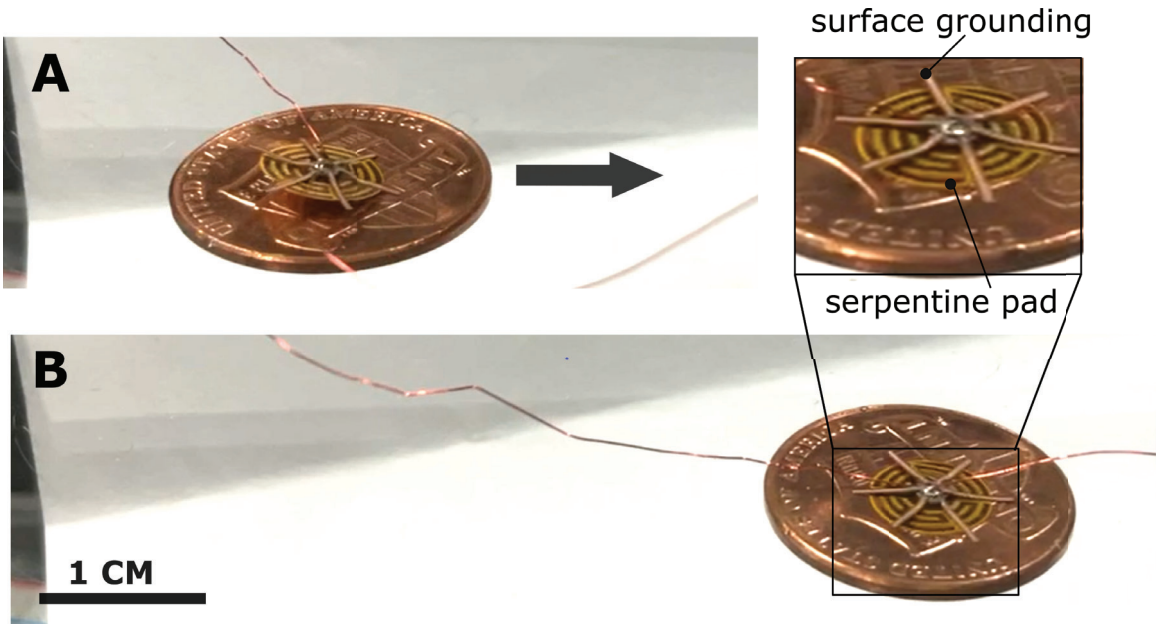


Figure 7.6: EA pad used to pull an ungrounded Cu penny (2.5g) on an acrylic plate. Additional grounding prongs were added to the pad to help ground otherwise ungrounded conductive object.

Electroadhesive pads could potentially be even more effective integrated with a tail device. Such a tail could be used alone (for stabilization while climbing inclines, similar to passive tails described in [12]) but also for actively for positioning of an electroadhesion gripper. An active tail (F) controlled by a 0-10 V signal *(in collaboration with Kahlil Wassel et. al.)* originally intended for payload manipulation for robot center of mass shifting and angling could potentially be incorporated with electroadhesive pads for the ability to actively pick up items or grab items from different heights in the future.

7.2.2.2 Self-grounded serpentine pad gripper

Within inspection or industrial environments, we assume ensuring grounded surfaces for traversal or adhesion to be a relatively reasonable condition. However, if we consider wanting to manipulate objects, expecting isolated items to be actively grounded (as in Fig. 7.5F), or otherwise always achieving strong contact to a grounded surface, may not be particularly reasonable.

We briefly demonstrate a potential design exploration for attempting to add a ground component to a unipolar pad design for attachment to conductive materials in the

case of no environmental grounding options. While further studies would be beneficial (there may still be some degree of charge buildup and variability with repeated use), we can demonstrate preliminary ability to attach to a conductive penny on a non-conductive acrylic surface and pull it across the surface successfully with this pad. Exploring further methods of grounding and manipulation of conductive objects in the absence of environmental grounding may be interesting for future work.

8

Conclusions

8.1 Summary of Work

In this work we explored the HAMR fabrication process, improved the processes used for robot manufacturing, and demonstrated fabrication of a small half-scaled (2 mm) HAMR-JR robot. Indepth characterizations and improvements to electroadhesion design and fabrication were made both for smooth prinstine terrains, as well as rough terrains of varying feature density. We sought to improve performance of electroadhesive capabilities on flat pristine surface, tuning fabrication process and design parameters to develop a pad with improved 60 g pad payload capacity, more than sufficient pure adhesion capabilities to carry gram-scale robots on flat pristine surfaces.

We further characterized and improved the performance on rough terrains, developing a rigorous test method to measure shear adhesion pressure performance of electroadhesive footpads. By adding compliance to electroadhesive pads through geometric design explorations, pads were designed to conform more closely to rough surfaces. Alongside experimental characterizations of both spoked and serpentine pads, we identified improved compliance of serpentine designs (which yielded roughly twice the adhesion pressures of their circular counterparts), and demonstrated performance with a variety of potential real-world industrial environment demos.

8.2 Future Work

Future work could continue improvements to the manufacturing techniques of these robots, with developments to improve the speed, reliability, and consistency of fabrication, both for regular manufacturing as a platform for research questions, as well as for transfer

from one researcher to another. While the practical fabrication of such precise robots can take time to achieve in research environments where materials, equipment performance, and processes are always in some degree of flux inbetween fabrication efforts, we've shown it is possible to transfer such processes out of the lab (as briefly mentioned in Chapter 3). With dedicated streamlined manufacturing and potential commercialization efforts of such systems someday, such robots could realistically be manufactured in larger batches with reasonable time and resource costs.

Future work to improve electroadhesion efforts specifically could build beyond the initial explorations of this thesis to further investigate additional 2D and 3D pad geometries. Pad designs could also be adapted to directional climbing, where asymmetrical designs for either pad shapes or legs of the robot might improve climbing capabilities. With more varied fabrication methods, 3D fibrous or soft compliant pads could provide another bioinspired approach and potentially enable the robot to tackle even more complex terrains.

Explorations of electroadhesion in tandem with other adhesion approaches like spines or feet structures could also be interesting to explore. This could be useful for more adaptable microrobots that could perhaps use different modes of adhesion on different types of surfaces to more appropriately tackle the specific challenge at hand. Multiple methods of adhesion used in parallel could also potentially enhanced the adhesion beyond what may be possible with a single mode [56]. Climbing strategies to tackle transitions between different types of inclines and surfaces would also be beneficial in enhancing the capabilities of robots to tackle the diversity of changing surfaces found in the real world.

More broadly, platform-level strategies could further expand robot climbing capabilities. These efforts could include robot transmission redesigns, robot center of mass alterations, or implementation of complimentary climbing appendages such as passive or active tails, claws, or spines. Alternative mechanisms for controlled peeling of pads via toe-like appendages similar to other climbing robots [87] could improve the foot release. Laterally compliant ankle and foot joint design could perhaps add additional in-plane compliance, allowing for robot flexibility in step placement to avoid center of mass drifts that buildup over the course of repeated open loop steps. Legs which could adjust their length could be interesting avenues for exploring adaptive transmission ratios, allowing for lower center of mass stability when needed during climbing, or tuning of payload verses speed capabilities. Additional sensing capabilities to detect contact can improve the ability to recover from a missed step, enabling climbing in the presence of more uncertain and uneven

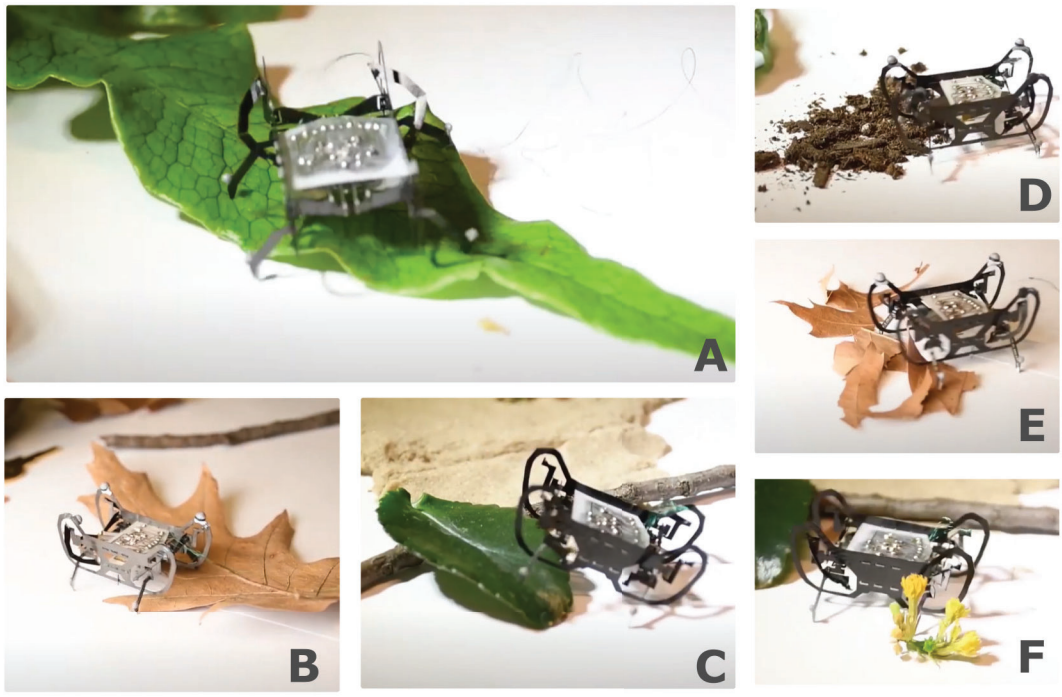


Figure 8.1: Natural envionments pose a variety of rough, inclined, and challenging obstacles for robots to navigate.

obstructions in the environment. Designs could aim to improve performance at different asperity scales or extend to compliant interdigitated pad designs for nonconductive surfaces. For remote usage, onboard power and control should be integrated [11] and improved for ease of autonomy integration and capability. Given the payload capacity characterizations conducted in this study, the mechanical capabilities of the robot should be sufficient, so actual integration of such boards onto a climbing robot would be a reasonable next step, and could allow for more interesting controls (to conduct actual inspection, real-time data collection or streaming, more informed step decisions, etc.) during climbing.

As we envision these robots eventually making their way into diverse terrains for industrial inspection or exploration tasks, we consider that increased understanding of performance on wide varieties of real world surfaces will be important. Effects of both macro curvatures and micro roughnesses interacting concurrently, or potential effects of surface and pad parameter combinations (e.g., pad width to terrain spacing dependence) could be explored. We further consider that complex real-world terrains may have varied surface chemistries (films, lubricants, dust, bio-fouling, etc.), and potentially unreliable grounding

options. Friction may vary due to surface contaminants, with roughness or lubrication impacting the contact interactions. Future studies of how terrain elements beyond just structural roughness impact performance would be beneficial. Beyond industrial inspection tasks (in which we might anticipate conductive surfaces and grounding options), work on small inspection robots could further consider how to tackle natural environments that may not have such readily convenient conditions. Such robots may consider nontoxic or even bio-degradeable materials in the event that all agents in a multi-robot exploration do not all return, with actuation and power to match such methods.

Whether future efforts focus on improvement of the fabrication process and robotic platform itself, enhancing capabilities through improved mechanical designs and electronics integration, further test the limits of geometrical and structural design for more broadly applicable compliance and adhesion applications, or explore the intricacies of environmental conditions, terrains, and surfaces to inform efforts to adapt during interactions, there are no shortage of avenues which could develop into interesting pathways for continued research. By improving the design of microrobots with environmental adaptability in mind, we look forward to seeing robots more robustly climbing inclined, rough, and diverse real-world surfaces into the future.

Bibliography

[1] R. J. Wood, "The first takeoff of a biologically inspired at-scale robotic insect," *IEEE transactions on robotics*, vol. 24, no. 2, pp. 341–347, 2008.

[2] Y. M. Chukewad, J. James, A. Singh, and S. Fuller, "Robofly: An insect-sized robot with simplified fabrication that is capable of flight, ground, and water surface locomotion," *IEEE Transactions on Robotics*, vol. 37, no. 6, pp. 2025–2040, 2021.

[3] K. Johnson, V. Arroyos, R. Villanueva, A. Schulz, S. Fuller, and V. Iyer, "Toward sub-gram helicopters: Designing a miniaturized flybar for passive stability," in *2023 IEEE/RSJ International Conference on Intelligent Robots and Systems (IROS)*, pp. 2701–2708, 2023.

[4] Y. Chen, C. Arase, Z. Ren, and P. Chirarattananon, "Design, characterization, and liftoff of an insect-scale soft robotic dragonfly powered by dielectric elastomer actuators," *Micromachines*, vol. 13, no. 7, p. 1136, 2022.

[5] R. S. Pierre and S. Bergbreiter, "Toward autonomy in sub-gram terrestrial robots," *Annual Review of Control, Robotics, and Autonomous Systems*, 2019.

[6] D. Kim, Z. Hao, J. Ueda, and A. Ansari, "A 5 mg micro-bristle-bot fabricated by two-photon lithography," *Journal of Micromechanics and Microengineering*, vol. 29, no. 10, p. 105006, 2019.

[7] R. J. Wood, S. Avadhanula, R. Sahai, E. Steltz, and R. S. Fearing, "Microrobot design using fiber reinforced composites," 2008.

[8] J. P. Whitney, P. S. Sreetharan, K. Y. Ma, and R. J. Wood, "Pop-up book mems," *Journal of Micromechanics and Microengineering*, vol. 21, no. 11, p. 115021, 2011.

[9] A. T. Baisch and R. J. Wood, "Design and fabrication of the harvard ambulatory microrobot," in *Robotics Research: The 14th International Symposium ISRR*, pp. 715–730, Springer, 2011.

[10] N. Doshi, B. Goldberg, R. Sahai, N. Jafferis, D. Aukes, R. J. Wood, and J. A. Paulson, "Model driven design for flexure-based microrobots," in *2015 IEEE/RSJ International Conference on Intelligent Robots and Systems (IROS)*, pp. 4119–4126, IEEE, 2015.

[11] B. Goldberg, R. Zufferey, N. Doshi, E. F. Helbling, G. Whittredge, M. Kovac, and R. J. Wood, "Power and control autonomy for high speed locomotion with an insect-scale legged robot," *IEEE Robotics and Automation Letters*, vol. 3, no. 2, pp. 987–993, 2018.

[12] B. F. Seitz, B. Goldberg, N. Doshi, O. Ozcan, D. L. Christensen, E. W. Hawkes, M. R. Cutkosky, and R. J. Wood, "Bio-inspired mechanisms for inclined locomotion in a legged insect-scale robot," in *2014 IEEE international conference on robotics and biomimetics (ROBIO 2014)*, pp. 791–796, IEEE, 2014.

[13] S. D. de Rivaz, B. Goldberg, N. Doshi, K. Jayaram, J. Zhou, and R. J. Wood, "Inverted and vertical climbing of a quadrupedal microrobot using electroadhesion," *Science Robotics*, vol. 3, no. 25, p. eaau3038, 2018.

[14] S. Seok, A. Wang, M. Y. Chuah, D. Otten, J. Lang, and S. Kim, "Design principles for highly efficient quadrupeds and implementation on the mit cheetah robot," in *2013 IEEE International Conference on Robotics and Automation*, pp. 3307–3312, IEEE, 2013.

[15] N. Kau, A. Schultz, N. Ferrante, and P. Slade, "Stanford doggo: An open-source, quasi-direct-drive quadruped," in *2019 International conference on robotics and automation (ICRA)*, pp. 6309–6315, IEEE, 2019.

[16] M. Raibert, K. Blankespoor, G. Nelson, and R. Playter, "Bigdog, the rough-terrain quadruped robot," *IFAC Proceedings Volumes*, vol. 41, no. 2, pp. 10822–10825, 2008.

[17] H. Hughes, C. McKinnell, T. Bartlett, L. Cunamay, J. Harmon, M. Treptau, C. Tossell, and J. Walliser, "Model-based systems engineering (mbse) a ghost robotics vision 60 q-ugv for future power systems and emerging military requirements," in *Proceedings of the Annual General Donald R. Keith Memorial Conference*, 2023.

[18] S. A. Burden, T. Libby, K. Jayaram, S. Sponberg, and J. M. Donelan, "Why animals can outrun robots," *Science Robotics*, vol. 9, no. 89, p. eadi9754, 2024.

[19] K. Y. Ma, P. Chirarattananon, S. B. Fuller, and R. J. Wood, "Controlled flight of a biologically inspired, insect-scale robot," *Science*, vol. 340, no. 6132, pp. 603–607, 2013.

[20] A. T. Baisch and R. J. Wood, "Pop-up assembly of a quadrupedal ambulatory microrobot," in *2013 IEEE/RSJ International Conference on Intelligent Robots and Systems*, pp. 1518–1524, IEEE, 2013.

[21] Y. Wu, J. K. Yim, J. Liang, Z. Shao, M. Qi, J. Zhong, Z. Luo, X. Yan, M. Zhang, X. Wang, *et al.*, "Insect-scale fast moving and ultrarobust soft robot," *Science Robotics*, vol. 4, no. 32, p. eaax1594, 2019.

[22] J. Liang, Y. Wu, J. K. Yim, H. Chen, Z. Miao, H. Liu, Y. Liu, Y. Liu, D. Wang, W. Qiu, *et al.*, "Electrostatic footpads enable agile insect-scale soft robots with trajectory control," *Science Robotics*, vol. 6, no. 55, p. eabe7906, 2021.

[23] J. Li, J. Deng, S. Zhang, W. Chen, J. Zhao, and Y. Liu, "Developments and challenges of miniature piezoelectric robots: A review," *Advanced Science*, vol. 10, no. 36, p. 2305128, 2023.

[24] C. Tang, B. Du, S. Jiang, Q. Shao, X. Dong, X.-J. Liu, and H. Zhao, "A pipeline inspection robot for navigating tubular environments in the sub-centimeter scale," *Science Robotics*, vol. 7, no. 66, p. eabm8597, 2022.

[25] W. Zou, E. Ma, H. Chen, F. Lin, Z. Xiao, Z. Zhang, J. Jiang, Y. Niu, P. Yu, and C. Wang, "Locomotion for insect-scale robots with bionic strategies: A review," *Journal of Field Robotics*, 2024.

[26] H. Kabutz and K. Jayaram, "Design of clari: A miniature modular origami passive shape-morphing robot," *Advanced Intelligent Systems*, vol. 5, no. 12, p. 2300181, 2023.

[27] H. Kabutz, A. Hedrick, W. P. McDonnell, and K. Jayaram, "mclari: a shape-morphing insect-scale robot capable of omnidirectional terrain-adaptive locomotion in laterally confined spaces," in *2023 IEEE/RSJ International Conference on Intelligent Robots and Systems (IROS)*, pp. 8371–8376, IEEE, 2023.

[28] P. Rajagopalan, M. Muthu, Y. Liu, J. Luo, X. Wang, and C. Wan, "Advancement of electroadhesion technology for intelligent and self-reliant robotic applications," *Advanced Intelligent Systems*, vol. 4, no. 7, p. 2200064, 2022.

[29] J. C. Spagna, D. I. Goldman, P.-C. Lin, D. E. Koditschek, and R. J. Full, "Distributed mechanical feedback in arthropods and robots simplifies control of rapid running on challenging terrain," *Bioinspiration & biomimetics*, vol. 2, no. 1, p. 9, 2007.

[30] K. A. Daltorio, T. E. Wei, A. D. Horchler, L. Southard, G. D. Wile, R. D. Quinn, S. N. Gorb, and R. E. Ritzmann, "Mini-whegs tm climbs steep surfaces using insect-inspired attachment mechanisms," *The International Journal of Robotics Research*, vol. 28, no. 2, pp. 285–302, 2009.

[31] A. T. Asbeck, S. Kim, M. R. Cutkosky, W. R. Provancher, and M. Lanzetta, "Scaling hard vertical surfaces with compliant microspine arrays," *The International Journal of Robotics Research*, vol. 25, no. 12, pp. 1165–1179, 2006.

[32] P. Borijindakul, A. Ji, Z. Dai, S. Gorb, and P. Manoonpong, "Mini review: Comparison of bio-inspired adhesive feet of climbing robots on smooth vertical surfaces. front. bioeng. biotechnol. 9: 765718. doi: 10.3389/fbioe. 2021.765718," *Frontiers in Bioengineering and Biotechnology— www. frontiersin. org*, vol. 9, 2021.

[33] B. Aksak, M. P. Murphy, and M. Sitti, "Gecko inspired micro-fibrillar adhesives for wall climbing robots on micro/nanoscale rough surfaces," in *2008 IEEE international conference on robotics and automation*, pp. 3058–3063, IEEE, 2008.

[34] P. Perez Goodwyn, A. Peressadko, H. Schwarz, V. Kastner, and S. Gorb, "Material structure, stiffness, and adhesion: why attachment pads of the grasshopper (tettigonia viridissima) adhere more strongly than those of the locust (locusta migratoria)(insecta: Orthoptera)," *Journal of comparative physiology A*, vol. 192, pp. 1233–1243, 2006.

[35] Y. Zhou, A. Robinson, C. Viney, and W. Federle, "Effect of shear forces and ageing on the compliance of adhesive pads in adult cockroaches," *The Journal of Experimental Biology*, vol. 218, no. 17, pp. 2775–2781, 2015.

[36] Y. Chen, N. Doshi, and R. J. Wood, "Inverted and inclined climbing using capillary

adhesion in a quadrupedal insect-scale robot," *IEEE Robotics and Automation Letters*, vol. 5, no. 3, pp. 4820–4827, 2020.

[37] M. A. Graule, P. Chirarattananon, S. B. Fuller, N. T. Jafferis, K. Y. Ma, M. Spenko, R. Kornbluh, and R. J. Wood, "Perching and takeoff of a robotic insect on overhangs using switchable electrostatic adhesion," *Science*, vol. 352, no. 6288, pp. 978–982, 2016.

[38] J. Guo, J. Leng, and J. Rossiter, "Electroadhesion technologies for robotics: A comprehensive review," *IEEE Transactions on Robotics*, vol. 36, no. 2, pp. 313–327, 2019.

[39] H. Prahlad, R. Pelrine, S. Stanford, J. Marlow, and R. Kornbluh, "Electroadhesive robots—wall climbing robots enabled by a novel, robust, and electrically controllable adhesion technology," in *2008 IEEE international conference on robotics and automation*, pp. 3028–3033, IEEE, 2008.

[40] P. S. Sreetharan, J. P. Whitney, M. D. Strauss, and R. J. Wood, "Monolithic fabrication of millimeter-scale machines," *Journal of Micromechanics and Microengineering*, vol. 22, no. 5, p. 055027, 2012.

[41] N. Doshi, K. Jayaram, B. Goldberg, Z. Manchester, R. J. Wood, and S. Kuindersma, "Contact-implicit optimization of locomotion trajectories for a quadrupedal microrobot," *arXiv preprint arXiv:1901.09065*, 2019.

[42] K. Jayaram, J. Shum, S. Castellanos, E. F. Helbling, and R. J. Wood, "Scaling down an insect-size microrobot, hamr-vi into hamr-jr," in *2020 IEEE International Conference on Robotics and Automation (ICRA)*, pp. 10305–10311, IEEE, 2020.

[43] Y. Chen, N. Doshi, B. Goldberg, H. Wang, and R. J. Wood, "Controllable water surface to underwater transition through electrowetting in a hybrid terrestrial-aquatic microrobot," *Nature communications*, vol. 9, no. 1, pp. 1–11, 2018.

[44] A. T. Baisch, *Design, manufacturing, and locomotion studies of ambulatory microrobots*. PhD thesis, Harvard, 2013.

[45] N. Doshi, K. Jayaram, S. Castellanos, S. Kuindersma, and R. J. Wood, "Effective locomotion at multiple stride frequencies using proprioceptive feedback on a legged microrobot," *Bioinspiration & biomimetics*, vol. 14, no. 5, p. 056001, 2019.

[46] N. T. Jafferis, M. J. Smith, and R. J. Wood, "Design and manufacturing rules for maximizing the performance of polycrystalline piezoelectric bending actuators," *Smart Materials and Structures*, vol. 24, no. 6, p. 065023, 2015.

[47] N. T. Jafferis, M. Lok, N. Winey, G.-Y. Wei, and R. J. Wood, "Multilayer laminated piezoelectric bending actuators: design and manufacturing for optimum power density and efficiency," *Smart Materials and Structures*, vol. 25, no. 5, p. 055033, 2016.

[48] R. St. Pierre and S. Bergbreiter, "Toward autonomy in sub-gram terrestrial robots," *Annual Review of Control, Robotics, and Autonomous Systems*, vol. 2, pp. 231–252, 2019.

[49] R. S. Pierre, W. Gosrich, and S. Bergbreiter, "A 3d-printed 1 mg legged microrobot running at 15 body lengths per second," in *Solid-State Sensors, Actuators, and Microsystems Workshop, Hilton Head, SC*, vol. 3, 2018.

[50] B. H. Shin and S.-Y. Lee, "Micro mobile robots using electromagnetic oscillatory actuator," in *2012 4th IEEE RAS & EMBS International Conference on Biomedical Robotics and Biomechatronics (BioRob)*, pp. 575–580, IEEE, 2012.

[51] D. S. Contreras and K. S. Pister, "A six-legged mems silicon robot using multichip assembly," in *Hilton Head Workshop*, 2018.

[52] Z. Zhakypov, K. Mori, K. Hosoda, and J. Paik, "Designing minimal and scalable insect-inspired multi-locomotion millirobots," *Nature*, vol. 571, no. 7765, pp. 381–386, 2019.

[53] M. H. Dickinson, C. T. Farley, R. J. Full, M. Koehl, R. Kram, and S. Lehman, "How animals move: an integrative view," *science*, vol. 288, no. 5463, pp. 100–106, 2000.

[54] N. T. Jafferis, K. Jayaram, P. A. York, and R. J. Wood, "A streamlined fabrication process for high energy density piezoelectric bending actuators," *Sensors and Actuators A: Physical*, vol. 332, p. 113155, 2021.

[55] T. Wöhrl, A. Richter, S. Guo, L. Reinhardt, M. Nowotny, and R. Blickhan, "Comparative analysis of a geometric and an adhesive righting strategy against toppling in inclined hexapedal locomotion," *Journal of Experimental Biology*, vol. 224, no. 15, p. jeb242677, 2021.

[56] D. Ruffatto III, A. Parness, and M. Spenko, "Improving controllable adhesion on both rough and smooth surfaces with a hybrid electrostatic/gecko-like adhesive," *Journal of The Royal Society Interface*, vol. 11, no. 93, p. 20131089, 2014.

[57] J. Guo, M. Tailor, T. Bamber, M. Chamberlain, L. Justham, and M. Jackson, "Investigation of relationship between interfacial electroadhesive force and surface texture," *Journal of Physics D: Applied Physics*, vol. 49, no. 3, p. 035303, 2015.

[58] P. E. Schiebel, J. Shum, H. Cerbone, and R. J. Wood, "An insect-scale robot reveals the effects of different body dynamics regimes during open-loop running in feature-laden terrain," *Bioinspiration & Biomimetics*, vol. 17, no. 2, p. 026006, 2022.

[59] Y. Yokokohji, S. Chaen, and T. Yoshikawa, "Evaluation of traversability of wheeled mobile robots on uneven terrains by a fractal terrain model," *Advanced Robotics*, vol. 21, no. 1-2, pp. 121–142, 2007.

[60] P.-L. Lechère, P. E. Schiebel, M. C. Yuen, J. Shum, and R. J. Wood, "Passive compliant foot design for improved micororobotic mobility on rough terrains," in *2022 IEEE/RSJ International Conference on Intelligent Robots and Systems (IROS)*, pp. 2526–2533, IEEE, 2022.

[61] A. M. Hernandez, P. E. Schiebel, J. Shum, and R. J. Wood, "Spines and inclines: Bioinspired spines on an insect-scale robot facilitate locomotion on rough and inclined terrain," *Integrative And Comparative Biology*, p. icae145, 2024.

[62] S. Catalán Izquierdo, J. M. Bueno Barrachina, C. S. Cañas Peñuelas, and F. Cavallé Sesé, "Capacitance evaluation on parallel-plate capacitors by means of finite element analysis," *Renewable energy and power quality journal*, vol. 1, no. 7, pp. 613–616, 2009.

[63] B. N. Persson and J. Guo, "Electroadhesion for soft adhesive pads and robotics: theory and numerical results," *Soft matter*, vol. 15, no. 40, pp. 8032–8039, 2019.

[64] M. Ciavarella and A. Papangelo, "A simplified theory of electroadhesion for rough interfaces," *Frontiers in mechanical engineering*, vol. 6, p. 27, 2020.

[65] D. Axinte, X. Dong, D. Palmer, A. Rushworth, S. C. Guzman, A. Olarra, I. Arizaga, E. Gomez-Acedo, K. Txoperena, K. Pfeiffer, *et al.*, "Miror—miniaturized robotic sys-

tems for holistic in-situ repair and maintenance works in restrained and hazardous environments," *IEEE/ASME Transactions on Mechatronics*, vol. 23, no. 2, pp. 978–981, 2018.

[66] X. Dong, D. Axinte, D. Palmer, S. Cobos, M. Raffles, A. Rabani, and J. Kell, "Development of a slender continuum robotic system for on-wing inspection/repair of gas turbine engines," *Robotics and computer-integrated manufacturing*, vol. 44, pp. 218–229, 2017.

[67] D. Axinte, "Portable robotised machines tools (robomach), for in-situ inspection and (re) manufacture: Research challenges and opportunities," 2024.

[68] J. Tao, H. Khosravi, V. Deshpande, and S. Li, "Engineering by cuts: How kirigami principle enables unique mechanical properties and functionalities," *Advanced Science*, vol. 10, no. 1, p. 2204733, 2023.

[69] A. Firouzeh, T. Higashisaka, K. Nagato, K. Cho, and J. Paik, "Stretchable kirigami components for composite meso-scale robots," *IEEE Robotics and Automation Letters*, vol. 5, no. 2, pp. 1883–1890, 2020.

[70] B. Liu, Y. Ozkan-Aydin, D. I. Goldman, and F. L. Hammond, "Kirigami skin improves soft earthworm robot anchoring and locomotion under cohesive soil," in *2019 2nd IEEE International Conference on Soft Robotics (RoboSoft)*, pp. 828–833, IEEE, 2019.

[71] Y.-C. Cheng, H.-C. Lu, X. Lee, H. Zeng, and A. Priimagi, "Kirigami-based light-induced shape-morphing and locomotion," *Advanced Materials*, vol. 32, no. 7, p. 1906233, 2020.

[72] C. Ai, Y. Chen, L. Xu, H. Li, C. Liu, F. Shang, Q. Xia, and S. Zhang, "Current development on origami/kirigami-inspired structure of creased patterns toward robotics," *Advanced Engineering Materials*, vol. 23, no. 10, p. 2100473, 2021.

[73] C. Branyan, R. L. Hatton, and Y. Mengüç, "Snake-inspired kirigami skin for lateral undulation of a soft snake robot," *IEEE Robotics and Automation Letters*, vol. 5, no. 2, pp. 1728–1733, 2020.

[74] K. Zhang, C. Qiu, and J. S. Dai, "Helical kirigami-enabled centimeter-scale worm robot with shape-memory-alloy linear actuators," *Journal of Mechanisms and Robotics*, vol. 7, no. 2, p. 021014, 2015.

[75] D.-G. Hwang, K. Trent, and M. D. Bartlett, "Kirigami-inspired structures for smart adhesion," *ACS applied materials & interfaces*, vol. 10, no. 7, pp. 6747–6754, 2018.

[76] R. Zhao, S. Lin, H. Yuk, and X. Zhao, "Kirigami enhances film adhesion," *Soft Matter*, vol. 14, no. 13, pp. 2515–2525, 2018.

[77] L. Jin and S. Yang, "Engineering kirigami frameworks toward real-world applications," *Advanced Materials*, vol. 36, no. 9, p. 2308560, 2024.

[78] C. Yang, H. Zhang, Y. Liu, Z. Yu, X. Wei, and Y. Hu, "Kirigami-inspired deformable 3d structures conformable to curved biological surface," *Advanced Science*, vol. 5, no. 12, p. 1801070, 2018.

[79] J. A. Shum, P. E. Schiebel, A. M. Hernandez, and R. J. Wood, "Electroadhesive pad design for increased adhesion of climbing microrobots on diverse terrains," *Under Review*, 2024.

[80] V. Cacucciolo, H. Shea, and G. Carbone, "Peeling in electroadhesion soft grippers," *Extreme Mechanics Letters*, vol. 50, p. 101529, 2022.

[81] B. Mandelbrot and M. Frame, "Fractal tree definitions, url = https://www.math.union.edu/research/fractaltrees/FractalTreesDefs.html. urldate = 2024-08-10," 2024.

[82] B. Mandelbrot, M. Frame, and N. Neger, "Fractal geometry - dimensions of fractal trees, url = https://gauss.math.yale.edu/fractals/FracTrees/Definitions/BinTreeAnim.html. urldate = 2024-08-10," 2024.

[83] R. Allain, "How to make a tree with fractals, url = https://www.wired.com/story/how-to-make-a-tree-with-fractals/. urldate = 2024-08-10," 2024.

[84] L. Riddle, "Agnes scott college, classic iterated functions- symmetric binary tree, url = https://larryriddle.agnesscott.org/ifs/pythagorean/symbinarytree.htm. urldate = 2024-08-10," 2024.

[85] A. C. Ugural, *Circular Plates*, p. 34. McGraw-Hill Publishing Company, 1981.

[86] T. Abondance, K. Jayaram, N. T. Jafferis, J. Shum, and R. J. Wood, "Piezoelectric grippers for mobile micromanipulation," *IEEE Robotics and Automation Letters*, vol. 5, no. 3, pp. 4407–4414, 2020.

[87] S. Kim, M. Spenko, S. Trujillo, B. Heyneman, V. Mattoli, and M. R. Cutkosky, "Whole body adhesion: hierarchical, directional and distributed control of adhesive forces for a climbing robot," in *Proceedings 2007 IEEE International Conference on Robotics and Automation*, pp. 1268–1273, IEEE, 2007.

A

Robot Toppling Avoidance

With contributions from Arjun Batra.

Climbing on inclined surfaces is an essential capability for insects to traverse and explore varied locations and lends insight for small bio-inspired robotic devices looking to reach similarly diverse sets of environments. However, such locomotion presents a few challenges: how does an insect avoid tipping over when climbing? And if a robot attempting similar locomotion patterns requires additional payload (due to power and controls electronics, etc.) where could it be optimally placed to avoid compounding the toppling challenge? With these considerations in mind, we explore: How does the center of mass distribution of a climbing robot influence the tipping angle limits of a purely geometric balance, and what adhesion forces are required to achieve climbing at higher angles? The Cataglyphis ant and Formica ant provide biological inspiration for addressing these challenges, each employing two different strategies against toppling (geometric and adhesion-based) with research having been done to examine how both adjusting the geometric distribution of the center of mass, and increasing the force of adhesion of the legs influences toppling prevention capabilities of a hexapedal tripod locomotion gait [55].

We apply insights from these ants to analysis on the HAMR platform, a small four-legged, 4.5cm, 1.5g robot that has been used for climbing tasks through use of electroadhesive pads and a bioinspired tripod gait . Although adhesion failures can cause robot falling/tipping (see Fig. A.3), this robot has been used to demonstrate climbing inclines of 0 to 180 degrees/inverted, with improvements to the electroadhesion being explored for improved payload and terrains capabilities. We hypothesize that by drawing on the two ant-inspired techniques, calculating the tipping angles possible via geometric center of mass payload allocation as well as adhesive force required, we can determine the relationship

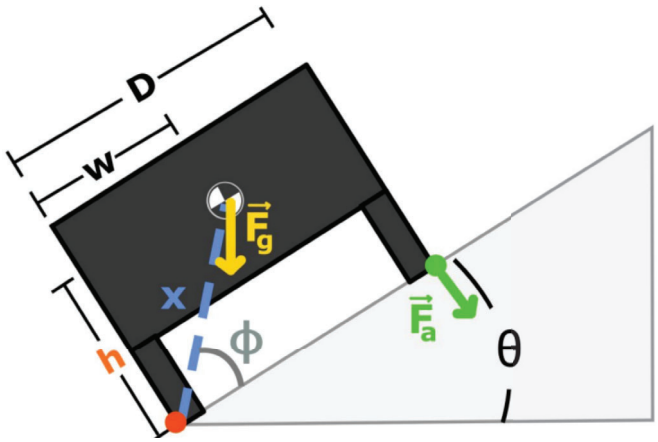


Figure A.1: Tipping model of inclined robot. The red dot denotes the tipping axis (at the robot hind legs). The center of mass height (h) from ground and width (w) from the leg, surface incline (θ), distance from tipping point to center of mass (x), and forces of gravity (F_g) and adhesion (F_a) are shown.

between these variables to better understand and drive the future test and design of such climbing robots.

We set out to find a relationship between the force applied from adhesion (F_a), the angle of the inclination (θ), and the height between the center of mass and the incline (h). These variables, and other measurements associated with the robot, are depicted in Fig. A.1. Our approach differed from that of Wöhrl et al. [55], where that paper used techniques related to static stability margin to project the inclined locomotion of the ant on a flat surface. We instead used direct calculation of the forces and torques. Another difference is that for ants, the tipping axis is diagonal along the inclined surface due to the hexapedal gait; the analysis for the quadrupedal HAMR robot with a tripod gait is made simpler by the fact that the tipping axis is orthogonal along the inclined surface. Our calculations for the relationship are shown in Fig. A.2.

Using the relationship described previously, we arrived at the following results: If there is no applied force due to adhesion, then the relationship simplifies to the equations below.

$$mg(hsin(\theta) - wcos(\theta)) \leq 0 \tag{A.1}$$

$$tan\theta \leq \frac{w}{h} \tag{A.2}$$

Forces Felt by the Robot:

$$\vec{F}_g = \begin{bmatrix} 0 \\ -mg \end{bmatrix}$$

$$\vec{F}_a = \begin{bmatrix} F_a \sin(\theta) \\ -F_a \cos(\theta) \end{bmatrix}$$

Moment Arms for the Forces:

$$\vec{r}_{CM} = \begin{bmatrix} x\cos(\theta+\phi) \\ x\sin(\theta+\phi) \end{bmatrix} = \begin{bmatrix} x[\cos(\theta)\cos(\phi) - \sin(\theta)\sin(\phi)] \\ x[\sin(\theta)\cos(\phi) + \cos(\theta)\sin(\phi)] \end{bmatrix}$$

$$= \begin{bmatrix} [x\cos(\phi)]\cos(\theta) - [x\sin(\phi)]\sin(\theta) \\ [x\cos(\phi)]\sin(\theta) + [x\sin(\phi)]\cos(\theta) \end{bmatrix} = \begin{bmatrix} w\cos(\theta) - h\sin(\theta) \\ w\sin(\theta) + h\cos(\theta) \end{bmatrix}$$

$$\vec{r}_a = \begin{bmatrix} D\cos(\theta) \\ D\sin(\theta) \end{bmatrix}$$

Torques due to the individual forces (positive torque contributes to tipping):

$$\tau_g = \vec{r}_{CM} \times \vec{F}_g = \begin{bmatrix} w\cos(\theta) - h\sin(\theta) \\ w\sin(\theta) + h\cos(\theta) \end{bmatrix} \times \begin{bmatrix} 0 \\ -mg \end{bmatrix} = mg(h\sin(\theta) - w\cos(\theta))$$

$$\tau_a = \vec{r}_a \times \vec{F}_a = \begin{bmatrix} D\cos(\theta) \\ D\sin(\theta) \end{bmatrix} \times \begin{bmatrix} F_a\sin(\theta) \\ -F_a\cos(\theta) \end{bmatrix} = -F_a D(\cos^2(\theta) + \sin^2(\theta)) = -F_a D$$

Relationship to prevent tipping (only considering not having positive torque):

$$\tau_{net} \leq 0 \qquad \tau_{net} = \tau_g + \tau_a = \boxed{mg(h\sin(\theta) - w\cos(\theta)) - F_a D \leq 0}$$

Figure A.2: Calculations for tipping torques as a result of gravity and potential counter-balancing adhesive forces.

This signifies that in order to not tip, the general considerations are to have a low inclination angle, a center of mass closer to the front of the robot, and a smaller distance between the center of mass and the inclined platform. If the above equations cannot be satisfied (tipping naturally occurs), then the robot will need to employ strategies in order to prevent itself from tipping. In an example HAMR robot (m = 1.529 g, h = 11 mm, w = 11 mm, D = 22 mm), if it is at an incline of 50°, then the robot will tip over since tan(50°)=1.2 > (11 mm/11 mm)=1. As performed in Cataglyphis ants, the robot could change its location of center of mass (effectively changing h) in order to no longer tip.

For the example HAMR robot, this can be achieved by changing the location of the center of mass to be around 8 mm (as opposed to its previous value of 11 mm), since tan(50°) < (11 mm/8 mm) = 1.4. On the other hand, using the strategy employed by Formica ants, another way to prevent tipping is to apply an adhesion force, which has to be at least a certain value to overcome the tipping. This lower bound can be determined from the boxed equation in Fig. A.2, arriving at the following equation.

$$F_a \geq \frac{mg(hsin(\theta) - wcos(\theta))}{D} \tag{A.3}$$

Applying the biomechanics analysis performed on ants, we were able to calculate the moments and showcase the difference between adjusting the center of mass or the adhesion force, as is described when contrasting Cataglyphis and Formica ants. Instead of

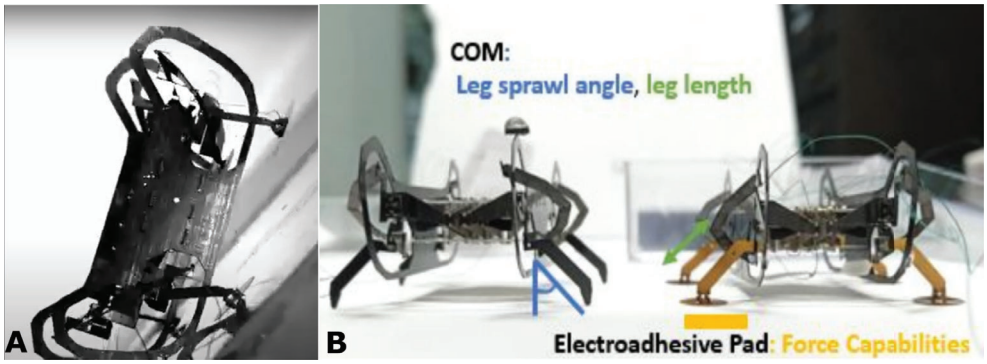


Figure A.3: A) HAMR falling/tipping during inclined locomotion when adhesion fails on the front legs. B) Strategies for changing center of mass (beyond just payload location).

just focusing on the two extremes of locomotion, future work could find an optimal combination that uses both, particularly in a robotic setting. Less energy/voltage is needed for geometric solutions of adjusting the center of mass, while applying adhesion force allows for more versatility when dealing with inclines. Especially with limitations in current technologies in terms of chassis adjustment and electroadhesion pads, it is important to keep both strategies in mind, to reach the goal of constructing a general purpose, bioinspired robot.

B

Compliant Kirigami Designs: Data Tables and ANOVA Tests

B.1 Design Parameters of Various Kirigami EA Pads Investigated

The design parameters for all pads fabricated are found in Table B.1. Both design parameters and geometry shape measurements[1] can be found. Border width[2] is mostly fixed, but had to be tweaked slightly for certain designs given geometries for feasible fabrication. Some parameters, like width for a circle or wedge[3], are continuous or variable, and do not fit the same characterization metrics as other shapes.

[1] # = number of branch/spokes revolved around the circular base, w = width, l_{eff} = effective length of a single pad from center base circle to outer edge, l_{total}='total' length of all pad branches added up together, Cu_{area} is the total area of the designed copper area, Cu_p is the total perimeter of designed copper area, b_w is the width of the Kapton border surrounding the copper, k_{area} is the total area of the pad including the kapton border, k_{perim} is the total perimeter of the pad including the Kapton border, A_{tot} is the total "footprint" area that examines the total area of a bounding circle required to fit the entire design inside, P/A is the ratio of perimeter to area (of the active copper material), and % Use is $\frac{Cu_{area}}{Area_{total}}$ or the % of the total footprint area that the active copper trace occupies, a rough measure of how efficiently the area is being used.

[2] Border width is generally fixed to $150\mu m$ for the most reliable fabrication to avoid breakdown/shorting, but to avoid self-intersection of some fractal designs, a slightly smaller width used.

[3] Wedge "width" was variable, changing along the length of each branch, from 1.5-4 mm

Table B.1: Electroadhesive Pad Geometry Designs

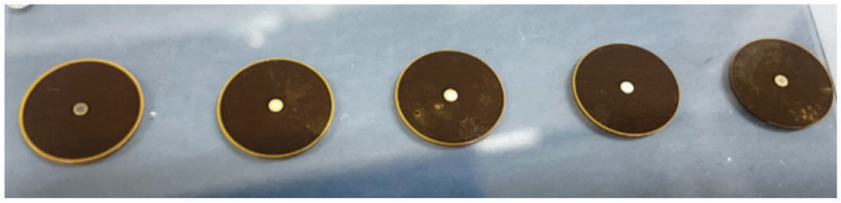
	Design Parameters				**Measurements** [1]						**Analysis**		
Design	Type	Descr.	#	w (mm)	l_{eff} (mm)	l_{total} (mm)	Cu_{area} (mm^2)	Cu_p (mm)	b_w[2] (mm)	k_{area} (mm^2)	k_{perim} (mm)	A_{tot} (mm^2)	P/A ratio	Use (%)
A[1]	Frac.	R_b 0.75, ∠15°	18	0.2	2.6	46	24	162	0.085	37	145	54	6.8	45
B	Fractal	R_b 0.75, ∠30°	10	0.2	2.6	26	17	105	0.15	32	97	55	6.2	31
C	Frac.	R_b 0.75, ∠45°	6	0.2	2.2	13	21	65	0.15	31	64	55	3.1	38
D	Frac.	R_b 0.5, ∠30°	10	0.2	2.6	26	15	87	0.15	28	82	55	5.8	27
E	Frac.	R_b 0.5, ∠30°	15	0.2	2.6	39	19	125	0.085	30	120	53	6.6	36
F	Spoke	thin (x10)	10	0.2	2.5	25	12	59	0.15	21	59	54	4.9	22
G	Spoke	thin (x30)	30	0.2	2.5	75	22	157	0.15	44	92	54	7.1	41
H	Spoke	w: 0.25 mm	6	0.25	2.5	15	11	38	0.15	17	39	54	3.5	20
I	Spoke	w: 0.5 mm	6	0.5	2.5	15	15	39	0.15	21	40	54	2.7	27
J	Spoke	w: 1 mm	6	1	2.5	15	22	40	0.15	28	41	54	1.8	41
K	Spoke	w: 2 mm	6	2	2.5	15	38	39	0.15	43	38	54	1.0	70
L	Serp.	w: 0.3 mm	6	0.3	11.8	71	29	150	0.15	50	148	51	5.3	56
M	Serp.	w: 0.5 mm	6	0.5	8.8	53	34	115	0.15	51	113	51	3.4	66
N	Serp.	w: 0.75 mm	6	0.75	5.5	33	33	75	0.15	44	74	44	2.3	74
O	Serp.	w: 1 mm	6	1	6.0	36	44	81	0.15	56	79	55	1.8	80
P	Wedge	(x6)	6	2.75[3]	2.5	15	44	55	0.15	48	55	54	1.2	82
Q	Circle		1	n/a	2.5	2.5	50	25	0.15	54	26	54	0.5	92

B.2 Test of Breakdown Voltage / Shorting of EA Pads

A



B



C

Border (mm)	0.2	0.15	0.1	0.075	0.05	0.025	0.01
Shorting (V)	2000+	2000+	2000+	2000+	1300	500	400

Figure B.1: Breakdown and laser resolution explorations. A) Small ring cut tests with varying thickness were conducted on two precision lasers to determine structural feature size limitations. On the first laser with no movement between cuts, rings with as thin as $50\mu m$ designed widths could be cut (and maintain a full circle design without cutting off part of the ring), while after a removal and realignment procedure the minimum as-designed width was around $75\mu m$. On the second laser it was around $150\mu m$. Both could potentially be improved by tuning the cut parameters to reduce burning (lighter power, but longer cuts) as well as further laser calibration. B) Examples of EA Pads fabricated with varying borders. C) Shorting tests (one trial each) for pads designed with different border widths indicate that thinner borders short sooner. The theoretical dielectric breakdown voltage for a slightly thicker $25\mu m$ kapton is around 300 V/μm so in theory a 7.5 μm should be sufficient for over 2000V, but due to alignment some edges are thinner than designed. A width of 0.15 mm was selected for border fabrication to safely avoid potential for shorting.

B.3 EA Pad Performance Data on Rough Surfaces

A representation of some of the individual trial runs from various pad types can be seen in Fig B.2, where it is possible to observe both the general force profile of data as well as the slight differences among different design types.

The raw data collected by the force sensor was filtered (using MATLAB filter parameters: *butter(6,0.003)*) and the peak maximum force of a trial run was measured. The result was zeroed by taking an average of 500 points (0.5 seconds of data) from both the start and from the maximum force. After subtracting the initial offset, the peak maximum force was recorded for each trial and used in subsequent analysis. All data can be found in tables below. Both the absolute force (in g) as well as the calculated pressure (force normalized by area of the copper only) are reported in Table B.7 for spoke tests and Table B.8 for serpentine tests.

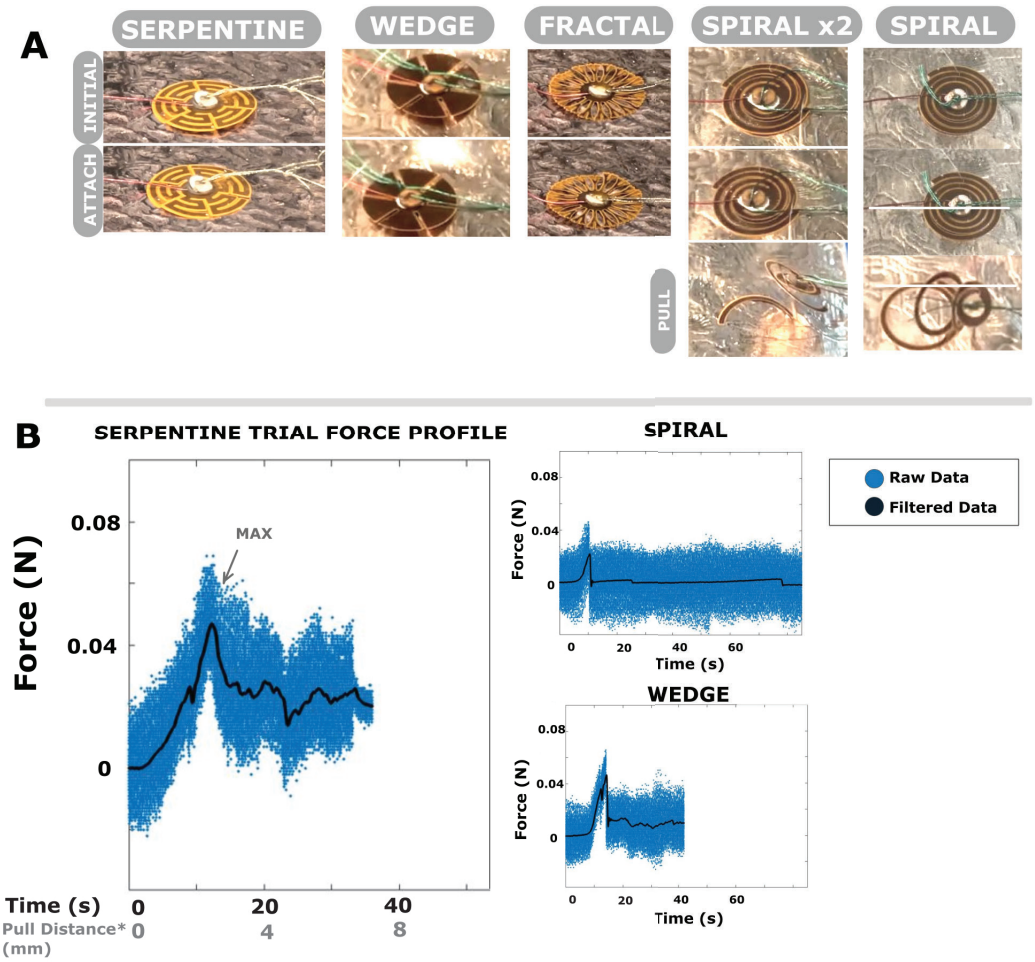


Figure B.2: A) Visualization of behavior of different geometry types when attaching. Note the shadowy regions which help indicate where pad is not attached. "Initial" represents the initial state, and "attach" shows the pad after the electroadhesive voltage is turned on. The wedge and fractal shapes can land at a slight angle such that not all parts of the pad contact the surface (seen with the shadowed regions both before and after), whereas with the serpentine shape we can see the pad more closely conform. B) Representative force profiles, with both raw and filtered data shown. (*) Pull distance is calculated from the time and the speed of the linear stage for reference. An indeterminate amount of string slack exists in the beginning of all trials prior to starting a run, meaning the distance does not directly correlate with pulling at the pad end of the setup.

Table B.2: Initial tests taken on a pristine conductive (Cu) flat surface with three to four data points per pad design.

	Shear Stress (Pa)											
Design	A	B	E	C	D	F	I	G	L	M	P	Q
Trial												
1	2352	753	6356	8090	3144	4937	3083	4059	2794	12897	6396	12982
2	2008	2947	5359	4719	3491	4433	2424	5786	3726	2766	4772	12707
3	3794	1495	2599	4042	2586	6115	3413	4250	1631	4636	5523	7451
4	3656	1200	3119	2925			2902		2824	3897		4385
mean	2953	1599	4358	4944	3074	5162	2955	4698	2744	6049	5563	9381
std	905	949	1791	2224	457	863	413	947	858	4630	1148	4192
significant	x	x			x		x		x			

	Shear Force (g)											
Design	A	B	E	C	D	F	I	G	L	M	P	Q
Trial												
1	5.65	1.28	13.35	12.14	5.97	5.92	4.62	8.93	8.10	43.85	28.14	64.91
2	4.82	5.01	11.25	7.08	6.63	5.32	3.64	12.73	10.80	9.40	20.99	63.54
3	9.11	2.54	5.46	6.06	4.91	7.34	5.12	9.35	4.73	15.76	24.30	37.25
4	8.77	2.04	6.55	4.39			4.35		8.19	13.25		21.92
mean	7.09	2.72	9.15	7.42	5.84	6.19	4.43	10.34	7.96	20.57	24.48	46.91
std	2.17	1.61	3.76	3.34	0.87	1.04	0.62	2.08	2.49	15.74	5.05	20.96
significant	x	x	x	x	x	x	x	x	x	x		

Table B.3: Initial tests taken on **Surface 1** (s:75 µm, h:2 mm) with four data points per pad design.

	Shear Stress (Pa)											
Design	A	B	E	C	D	F	I	G	L	M	P	Q
Trial												
1	1087	2454	916	446	393	1770	742	2093	1116	577	1094	1355
2	2311	641	1967	1939	2160	1235	915	1195	1512	1530	1373	1458
3	1341	231	387	2100	1458	1840	1460	840	1411	1605	1390	1422
4	755	2040	1342	809	919	1630	1207	1267	809	1355	1739	1115
mean	1374	1342	1153	1324	1232	1615	1081	1349	1212	1267	1399	1338
std	670	1072	669	820	756	271	317	530	317	472	264	154
significant												

	Shear Force (g)											
Design	A	B	E	C	D	F	I	G	L	M	P	Q
Trial												
1	2.61	4.17	1.92	0.67	0.75	2.12	1.11	4.60	3.24	1.96	4.81	6.77
2	5.55	1.09	4.13	2.91	4.10	1.48	1.37	2.63	4.39	5.20	6.04	7.29
3	3.22	0.39	0.81	3.15	2.77	2.21	2.19	1.85	4.09	5.46	6.12	7.11
4	1.81	3.47	2.82	1.21	1.75	1.96	1.81	2.79	2.35	4.61	7.65	5.58
mean	3.30	2.28	2.42	1.99	2.34	1.94	1.62	2.97	3.52	4.31	6.16	6.69
std	1.61	1.82	1.40	1.23	1.44	0.32	0.48	1.17	0.92	1.60	1.16	0.77
significant [2]	x	x	x	x	x	x	x	x	x			

Table B.4: Initial tests taken on **Surface 2** (s:75 µm, h:1 mm) with 10 data points per pad design.

	Shear Stress (Pa)						**Shear Force (g)**					
Design	A	E	G	M	P	Q	A	E	G	M	P	Q
Trial												
1	250	1084	440	276	228	135	0.60	1.84	0.97	0.94	1.00	0.68
2	822	68	952	501	241	202	1.97	0.12	2.09	1.71	1.06	1.01
3	400	409	371	286	64	117	0.96	0.70	0.82	0.97	0.28	0.58
4	347	617	338	379	246	202	0.83	1.05	0.74	1.29	1.08	1.01
5	504	430	578	308	434	196	1.21	0.73	1.27	1.05	1.91	0.98
6	448	467	459	420	230	218	1.08	0.79	1.01	1.43	1.01	1.09
7	517	467	380	346	239	173	1.24	0.79	0.84	1.18	1.05	0.87
8	542	402	792	564	80	248	1.30	0.68	1.74	1.92	0.35	1.24
9	256	170	177	515	115	260	0.61	0.29	0.39	1.75	0.51	1.30
10	298	161	275	557	145	345	0.72	0.27	0.61	1.90	0.64	1.73
Mean	438	428	476	415	202	210	1.05	0.73	1.05	1.41	0.89	1.05
Std	172	286	237	112	108	65	0.41	0.49	0.52	0.38	0.47	0.33
significant			x									

Table B.5: Initial tests taken on **Surface 3** (s:75 µm, h:0.3 mm) with three data points per pad design.

	Shear Stress (Pa)			**Shear Force (g)**		
Design	A	M	Q	A	M	Q
Trial						
1	181	223	107	0.43	0.76	0.53
2	182	187	43	0.44	0.63	0.22
3	149	218	41	0.36	0.74	0.21
Mean	171	209	64	0.41	0.71	0.32
Std	19	20	37	0.05	0.07	0.19
significant	x	x			x	

Table B.6: **Relative performance** of select pads types over varying surfaces.

	Performance				**Comparison Ratio**							
	Shear Stress (Pa)				**To Best of Self**				**To Ideal Case**			
Design	Flat	S1	S2	S3	Flat	S1	S2	S3	Flat	S1	S2	S3
Circle (Q)	9381	1338	210	64	1.00	0.14	0.02	0.01	1.00	0.14	0.02	0.01
Fractal (A)	2953	1374	438	171	1.00	0.47	0.15	0.06	0.31	0.15	0.05	0.02
Serpentine (M)	6049	1267	415	209	1.00	0.21	0.07	0.03	0.64	0.14	0.04	0.02

	Shear Force (g)				**To Best of Self**				**To Ideal Case**			
Design	Flat	S1	S2	S3	Flat	S1	S2	S3	Flat	S1	S2	S3
Circle (Q)	46.91	6.69	1.05	0.32	1	0.14	0.02	0.01	1.00	0.14	0.02	0.01
Fractal (A)	7.09	3.30	1.05	0.41	1	0.47	0.15	0.06	0.15	0.07	0.02	0.01
Serpentine (M)	20.57	4.31	1.41	0.71	1	0.21	0.07	0.03	0.44	0.09	0.03	0.02

Table B.7: **Spoke width** data taken on Surface 2 (s:75 µm, h:1 mm) with 15 data points per pad design. [1] Includes the same baseline circular pad performance data used for comparison with the serpentine results table, with additional data points added here.

	Shear Stress (Pa)					**Shear Force (g)**				
Design	H	I	J	K	Q	H	I	J	K	Q
Width (mm)	0.25	0.5	1	2	4.2	0.25	0.5	1	2	4.2
Cu Area (mm^2)	11	15	22	38	50	11	15	22	38	50
Type	Spoke	Spoke	Spoke	Spoke	Circle[1]	Spoke	Spoke	Spoke	Spoke	Circle[1]
Trial										
1	482	455	82	127	202	0.53	0.68	0.18	0.48	1.01
2	543	208	559	287	173	0.60	0.31	1.23	1.09	0.87
3	785	385	462	180	117	0.86	0.58	1.02	0.68	0.58
4	304	457	83	372	202	0.33	0.68	0.18	1.41	1.01
5	291	322	323	338	248	0.32	0.48	0.71	1.28	1.24
6	76	276	573	375	260	0.08	0.41	1.26	1.43	1.30
7	232	582	249	245	102	0.26	0.87	0.55	0.93	0.51
8	180	312	107	270	130	0.20	0.47	0.24	1.03	0.65
9	448	281	321	347	118	0.49	0.42	0.71	1.32	0.59
10	556	641	325	230	48	0.61	0.96	0.72	0.87	0.24
11	713	379	196	88	136	0.78	0.57	0.43	0.33	0.68
12	249	265	107	248	246	0.27	0.40	0.23	0.94	1.23
13	111	271	129	251	181	0.12	0.41	0.28	0.95	0.90
14	598	315	203	224	58	0.66	0.47	0.45	0.85	0.29
15	349	261	95	151	286	0.38	0.39	0.21	0.57	1.43
Mean	394	361	254	249	167	0.43	0.54	0.56	0.95	0.84
Std	216	125	169	87	74	0.24	0.19	0.37	0.33	0.37
significant	x	x				x				

Table B.8: **Serpentine width and length** data taken on Surface 2 (s:75 µm, h:1 mm) with eight data points per pad design.

	Shear Stress (Pa)					**Shear Force (g)**				
Design	L	M	N	O	Q	L	M	N	O	Q
Width (mm)	0.25	0.5	0.75	1	-	0.25	0.5	0.75	1	-
Length (mm)	11	8	5.2	5.2	4	11	8	5.2	5.2	4
Cu Area (mm^2)	29	34	33	44	50	29	34	33	44	50
Type	Spoke	Spoke	Spoke	Spoke	Circle	Spoke	Spoke	Spoke	Spoke	Circle
Trial										
1	485	594	447	367	202	1.41	2.02	1.47	1.62	1.01
2	610	482	366	263	173	1.77	1.64	1.21	1.16	0.87
3	586	503	364	373	117	1.70	1.71	1.20	1.64	0.58
4	315	436	353	246	202	0.91	1.48	1.16	1.08	1.01
5	493	650	215	395	248	1.43	2.21	0.71	1.74	1.24
6	850	353	224	98	260	2.47	1.20	0.74	0.43	1.30
7	534	401	355	289	102	1.55	1.36	1.17	1.27	0.51
8	359	526	525	291	130	1.04	1.79	1.73	1.28	0.65
Mean	529	493	356	290	179	1.53	1.68	1.18	1.28	0.90
Std	165	98	103	95	59	0.48	0.33	0.34	0.42	0.30
significant	x	x	x			x	x			

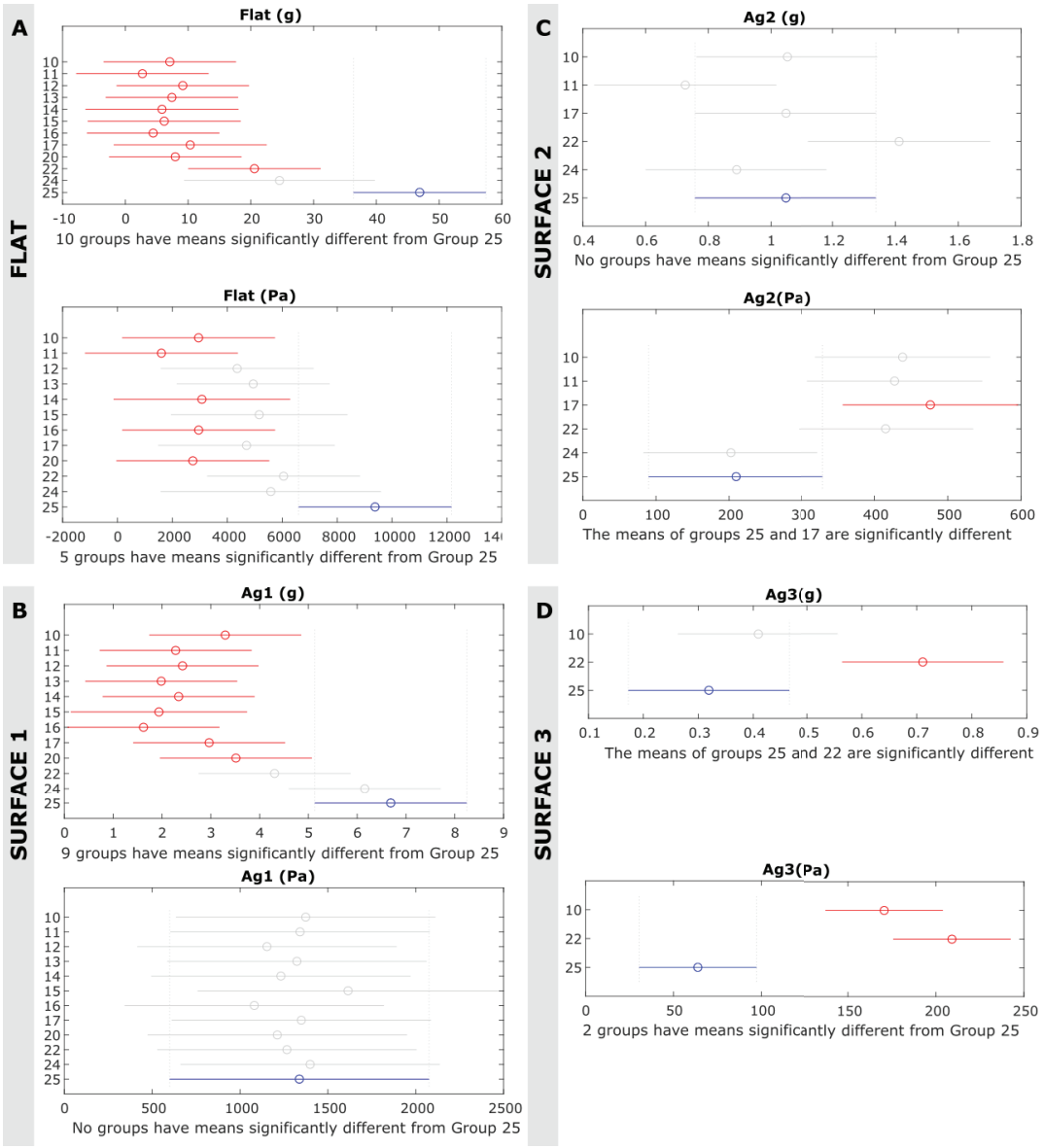


Figure B.3: **Statistical significance** was tested using *anova1* and *multcompare* functions in MATLAB to perform a one-way analysis of variance (ANOVA) test for each set of data. The horizontal axis shows the data (shear stress or force, accordingly) and variation, while the vertical axis shows the group tests that correspond to trials labelled in surface test data tables (assortment of fractals, spokes, serpentines, wedges, circles). Section marked A) Flat, B) Surface 1, C) Surface 2, and D) Surface 3 denote the surface used in testing for that data set.

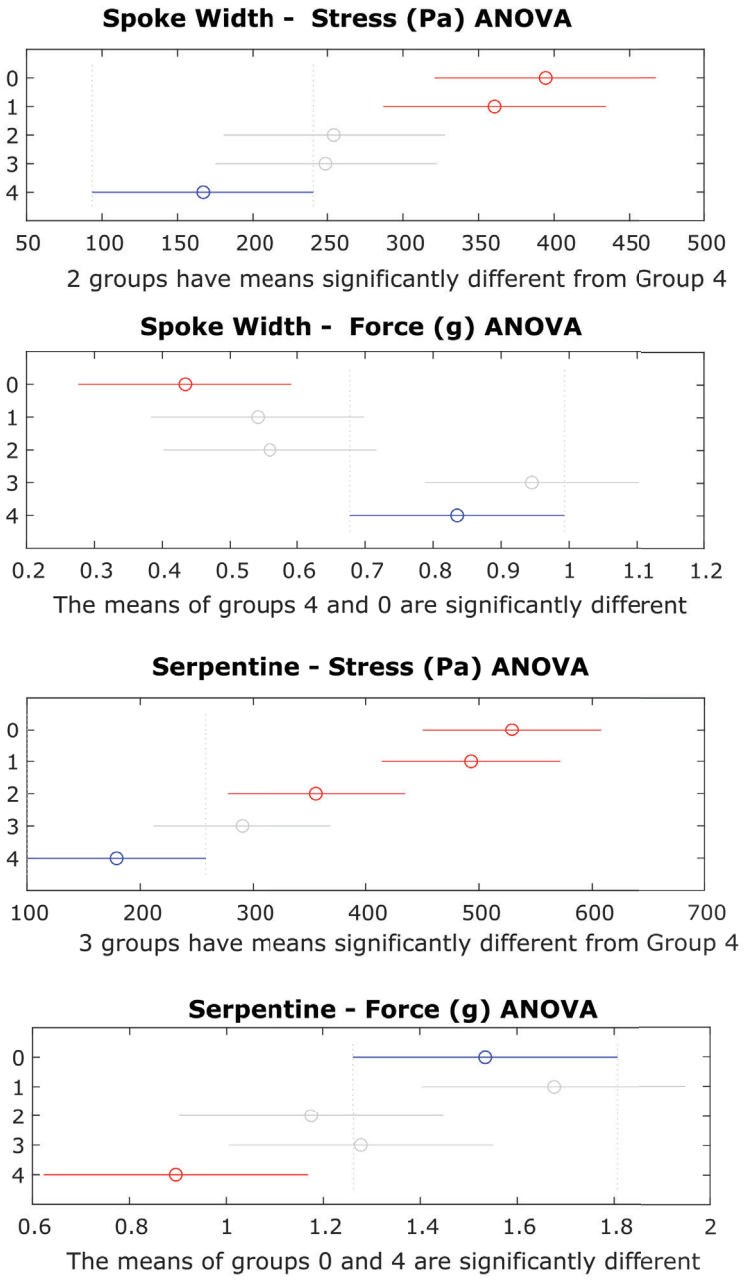


Figure B.4: **Statistical significance** was tested using *anova1* and *multcompare* in MATLAB to perform a one-way analysis of variance (ANOVA) test for each set of data. The horizontal axis shows the data (shear stress or force, accordingly) and variation, while the vertical axis shows the group tests in order of increasing width (spoke) or increasing lengths (serpentine).